

ENGINEERING METALLIC NANOGAP APERTURES
FOR ENHANCED OPTICAL TRANSMISSION

A DISSERTATION
SUBMITTED TO THE FACULTY OF
UNIVERSITY OF MINNESOTA
BY

DAEHAN YOO

IN PARTIAL FULFILLMENT OF THE REQUIREMENTS
FOR THE DEGREE OF
DOCTOR OF PHILOSOPHY

PROF. SANG-HYUN OH, ADVISOR

OCTOBER, 2016

© DAEHAN YOO 2016

ALL RIGHTS RESERVED

Acknowledgements

I would like to thank my advisor, Professor Sang-Hyun Oh, for his guidance in my research as well as strong support during my doctoral study. I am deeply grateful for his effort to organize the collaborations with great scientists. I would also like to thank all collaborators, Professor Jaime Peraire and Dr. Ngoc-Cuong Nguyen at Massachusetts Institute of Technology, Professor Luis Martin-Moreno at Instituto de Ciencia de Materiales de Aragón and Dr. Sol Carretero-Palacios at Institute of Materials Science of Sevilla, Professor Thomas W. Ebbesen at the University of Strasbourg. Their insight and valuable advices enable me to achieve research results presented in this dissertation. I would also like to thank the members of my dissertation committee, Professors Stephen Campbell, Mo Li, and Vivian Ferry. Their suggestions and comments improved my dissertation greatly.

I wish to thank Si-Hoon Lee for his encouraging words and instructions for nanofabrication. I deeply appreciate Avijit Barik's work on dielectrophoresis and Dan Mohr's collaboration on computational modeling. Other group members, Nate Wittenberg, Jincy Jose, Sudhir Cherukulappurath, Tim Johnson, Luke Jordan, Xiaoshu Chen, Shailabh Kumar, Hyeong-Ryeol Park, Yong-Sang Ryu, Seon Namgung, Daniel Klemme, Christopher Ertsgaard, and Milan Vala also deserve my gratitude. Furthermore, I thank my good friends I met here, Wonho Choi, Jongyeon Kim, Albert Jang, Sechul Park and many others.

Out of the lab, and perhaps most importantly, it was my family and friends that encouraged me. To all, a deep thank you. And to my parents, I know my achievement would never have been made without their sacrifice. I am grateful for them with my heart. At this end, I would like to thank my wife, Yeonka Kim, for being beside me all the times. We have walked along together on this journey of doctoral study, and will be on our way together.

Dedication

This dissertation is dedicated to my wife, Yeonka Kim for her love and devotion during my doctoral study and to my little one, Claire Hara Yoo, who gave me a meaning and joy of life.

Engineering metallic nanogap apertures for enhanced optical transmission by Daehan Yoo

Abstract

Physics and technology of metallic nanoapertures have been of great interest in nanophotonics. In particular, enhanced optical transmission mediated by surface plasmon waves in metallic nanoapertures has been widely studied and utilized in biochemical sensing, imaging, optical trapping, nonlinear optics, metamaterials, and optoelectronics. State-of-the-art nanotechnology enables researchers to explore optical physics in complex nanostructures. However, the high cost and tedium of conventional fabrication approaches such as photolithography, electron-beam lithography, or focused-ion-beam milling have limited the utilization of metallic nanoapertures for practical applications. This dissertation explores new approaches to enable high-throughput fabrication of sub-10-nm nanogaps and apertures in metal films. In particular, we focus on a new technique called atomic layer lithography, which turns atomic layer deposition into a lithographic patterning technique and can create ultra-small coaxial nanoapertures. The resulting nanostructures allowed us to observe extraordinary optical transmission in mid-infrared regime that originates from an intriguing physical phenomenon called the epsilon-near-zero (ENZ) condition. Subsequently, we turn this nanogap structure into a high-Q-factor plasmonic resonator, called a trench nanogap resonator, by combining a nanogap and sidewall mirrors. This structure is optimized for electrical trapping of biomolecules and concurrent optical detection, which is demonstrated experimentally via dielectrophoresis-enhanced plasmonic sensing. The fabrication technique and resulting structures demonstrated in this thesis work can facilitate practical engineering of metallic nanoapertures towards harnessing the potential of plasmonics.

Contents

Acknowledgements	i
Dedication	ii
Abstract	iii
List of Tables	vii
List of Figures	viii
List of Publications	x
1 Introduction	1
1.1 Engineering Optical Metallic Nanostructure.	1
1.2 State-of-the-art Nanotechnology.	2
1.3 Limits of Current Technology.	3
1.4 Scope of This Dissertation.	3
1.4.1 Outline of Chapters.	3
2 Theoretical Background	5
2.1 Optical Properties of Materials.	5
2.1.1 Maxwell's Equations.	5
2.1.2 Light: the Wave Equation.	6
2.1.3 Lorentz Model of Dielectric.	8
2.1.4 Drude Model of Metal.	9
2.2 Plasmonics.	11
2.2.1 Surface Plasmon Polaritons.	11
2.2.2 Excitation of Surface Plasmon Polaritons.	13
2.3 Gap Plasmon.	15
2.4 Extraordinary Optical Transmission (EOT).	17
2.4.1 EOT at Nanohole Aperture Array.	17
2.4.2 EOT at Coaxial Aperture.	20
2.5 Epsilon-Near-Zero (ENZ).	23
2.5.1 ENZ Materials.	24
2.5.2 Supercoupling Effect.	27

3	Extraordinary Optical Transmission through Ultra-small Coaxial Apertures	28
3.1	EOT via ENZ at Cutoff Frequency.	28
3.2	High-throughput Fabrication of Coaxial Nanogap Aperture Array.	29
3.3	Optical Measurement Setup.	34
3.3.1	Optical Measurements for Visible and Near-infrared.	34
3.3.2	FTIR Instrument and Measurement for Mid-infrared.	35
3.4	Transmission Spectra Measured from Visible to Mid-infrared.	36
3.5	Finite Element Method Modeling Results.	39
3.6	ENZ Property of Coaxial Nanogap Aperture.	41
3.7	Dispersion of Coaxial Nanogap Aperture.	42
3.8	Conclusion.	45
4	Optically-active Trench Nanogap Resonators	46
4.1	High Q Factor and Fano Resonance.	46
4.2	Plasmon Excitation and Resonances in a Trench Nanogap Resonator.	47
4.3	Optical Properties of a Trench Resonator.	48
4.3.1	Fano Resonance Induced by Nanogap.	48
4.3.2	Dispersion of Fano resonance with Trench Width.	51
4.3.3	Asymmetric geometrical effect.	53
4.3.4	Reflection Effect on Sidewall.	55
4.4	Fabrication of a Trench Nanogap Resonator.	56
4.5	Experimental Characterization of a Trench Nanogap Resonator.	57
4.6	Refractive Index Sensitivity.	59
4.7	Conclusion.	60
5	Electrically-active Trench Nanogap Resonators	61
5.1	Dielectrophoresis (DEP).	62
5.2	On-chip Biosensor: DEP Trapping in a Trench Nanogap Resonator.	66
5.3	Transmission Measurement of a Trench Nanogap Resonator in Water.	69
5.4	Experiment of DEP-enhanced Plasmonic Sensing.	70
5.5	Limit of Detection: Size and Concentration.	72
5.6	Conclusion.	73

6	Other Research Results: Template-stripped Tunable Plasmonic Devices on Stretchable and Rollable Substrates	74
6.1	Motivation of Flexible Optical and Electrical Devices.	75
6.2	Stretchable Plasmonic Nanohole Device.	76
6.2.1	Fabrication of Stretchable Gold Nanohole Arrays.	76
6.2.2	Characterization of Stretchable Gold Nanohole Arrays.	77
6.3	Stretchable Plasmonic Gold Pyramids.	79
6.3.1	Fabrication of Stretchable Gold Pyramids.	79
6.3.2	Characterization of Stretchable Gold Pyramids.	81
6.4	Roller Template Stripping.	82
6.5	Conclusion.	85
7	Conclusion and Future Directions	86
7.1	Dissertation Overview and Conclusions.	86
7.2	Future Directions.	88
7.2.1	Nanogap-enhanced Infrared Absorption.	88
7.2.2	VO ₂ -incorporated Coaxial Nanogap Aperture Array.	90
	Bibliography	92
	Appendix A	102
A.1	Coaxial Nanogap Aperture.	102
A.2	Trench Nanogap Resonator-Electrode.	103
A.3	Template-stripped Nanohole Array.	105
	Appendix B Common Acronyms	109

List of Tables

3.1	The EOT calculated from the measured transmission with different gap widths.	38
B1	A listing of the common acronyms used throughout the dissertation text.	109

List of Figures

2.1	Characteristics of surface plasmon polaritons.	11
2.2	Dispersion relation of surface plasmon polariton at a dielectric-metal interface.	14
2.3	Excitation of surface plasmon polaritons.	15
2.4	Two dispersion modes of gap plasmon in metal-insulator-metal (MIM) waveguide.	16
2.5	Dispersion relations of MIM waveguides with different gap sizes.	17
2.6	EOT through silver nanohole arrays.	19
2.7	The cutoff wavelengths of the first guided modes for different waveguides.	20
2.8	Cutoff wavelengths of the TE_{11} mode of both PEC and silver coaxial waveguides.	21
2.9	Longitudinal electric field intensity distribution along annular aperture array.	22
2.10	Epsilon-near-zero materials.	23
2.11	Real and imaginary permittivity of the ITO film.	24
2.12	Permittivity of metal-dielectric multilayered ENZ material.	25
2.13	Dispersion of the guided wave number in a rectangular plasmonic channel.	26
3.1	The progress in developing atomic layer lithography.	31
3.2	SEM images corresponding to process steps.	32
3.3	Atomic force microscope characterization.	33
3.4	Schematic of optical measurement setup for visible and near-IR.	34
3.5	Schematic of optical measurement setup for mid-IR.	35
3.6	Measured extraordinary transmission through the coaxial aperture array.	36
3.7	Simulated extraordinary transmission through the coaxial aperture array.	40
3.8	Experimental verification of the FP0 cut-off resonance mode.	41
3.9	The effect of diameter on the transmission resonances.	42
3.10	The effect of period on the transmission resonances.	44
3.11	The angular dependence on the transmission resonances.	44
4.1	Illustration of the Fano formula.	47
4.2	Schematic of optical interference in a trench nanogap structure.	47
4.3	Fano-resonance with high Q induced by nanogap.	48
4.4	Q factor and FWHM calculated from FDTD modeling as a function of gap size.	50
4.5	Dispersion of destructive mode with trench width.	51

4.6	Plasmon-induced transparency (PIT) via breaking geometric symmetry.	53
4.7	The geometrical effect of sidewall mirrors on the resonance.	55
4.8	Fabrication schematic of trench resonator.	56
4.9	Optical measurement setup for trench resonator.	57
4.10	Experimental measurement of trench nanogap resonator.	58
4.11	Bulk sensitivity of asymmetric trench resonator.	59
5.1	Schematic of the polarization of dielectric particle in a surrounding medium.	62
5.2	Schematic diagram of how different DEP forces occurs.	63
5.3	Plot of the normalized dielectrophoretic force against frequency.	65
5.4	On-chip biosensor for DEP-enhanced plasmonic biosensing.	66
5.5	FEM modeling of electric field in the 10 nm gap electrode of a trench resonator.	67
5.6	Transmission spectrum from asymmetric trench resonator biosensor in water.	69
5.7	Dielectrophoretic manipulation of 190 nm fluorescent polystyrene beads.	70
5.8	Experiments for limit of detection.	72
6.1	Schematic of the fabrication for stretchable gold nanohole arrays.	76
6.2	Optical characterization of stretchable gold nanohole arrays on a PDMS film.	77
6.3	Simulation of transmission from a nanohole array stretched along the x axis.	79
6.4	Fabrication of isolated gold pyramids template-stripped onto PDMS.	80
6.5	Tunable resonances of stretched metallic pyramids on PDMS.	82
6.6	Roller template stripping process.	84
7.1	Gap-enhanced IR absorption spectroscopy.	89
7.2	VO ₂ -incorporated coaxial nanogap apertures.	91

List of Publications

1. **Daehan Yoo**, N. C. Nguyen, L. Martin-Moreno, D. A. Mohr, S. Carretero-Palacios, J. Shaver, J. Peraire, T. W. Ebbesen, S. H. Oh. “High-Throughput Fabrication of Resonant Metamaterials with Ultrasmall Coaxial Apertures via Atomic Layer Lithography,” *Nano Lett* **2016**, 16, (3), 2040-2046.
2. **Daehan Yoo**, T. W. Johnson, S. Cherukulappurath, D. J. Norris, S. H. Oh. “Template-Stripped Tunable Plasmonic Devices on Stretchable and Rollable Substrates,” *ACS Nano* **2015**, 9, (11), 10647-10654.
3. Y. S. Ryu, **Daehan Yoo**, N. J. Wittenberg, L. R. Jordan, S. D. Lee, A. N. Parikh, S. H. Oh. “Lipid Membrane Deformation Accompanied by Disk-to-Ring Shape Transition of Cholesterol-Rich Domains,” *J. Am. Chem. Soc.* **2015**, 137, (27), 8692-8695.
4. M. S. Nezami, **Daehan Yoo**, G. Hajisalem, S. H. Oh, R. Gordon. “Gap Plasmon Enhanced Metasurface Third-Harmonic Generation in Transmission Geometry,” *ACS Photonics* **2016**, 3, (8), 1461-1467.
5. A. Barik, L. M. Otto, **Daehan Yoo**, J. Jose, T. W. Johnson, S. H. Oh. “Dielectrophoresis-Enhanced Plasmonic Sensing with Gold Nanohole Arrays,” *Nano Lett.* **2014**, 14, (4), 2006-2012.
6. J. A. Jackman, E. Linardy, **Daehan Yoo**, J. Seo, W. B. Ng, D. J. Klemme, N. J. Wittenberg, S. H. Oh, N. J. Cho. “Plasmonic Nanohole Sensor for Capturing Single Virus-Like Particles toward Virucidal Drug Evaluation,” *Small* **2016**, 12, (9), 1159-1166.
7. O. Limaj, D. Etezadi, N. J. Wittenberg, D. Rodrigo, **Daehan Yoo**, S. H. Oh, H. Altug. “Infrared Plasmonic Biosensor for Real-Time and Label-Free Monitoring of Lipid Membranes,” *Nano Lett.* **2016**, 16, (2), 1502-1508.
8. X. H. Xu, A. Denic, L. R. Jordan, N. J. Wittenberg, A. E. Warrington, B. Wootla, L. M. Papke, L. J. Zoecklein, **Daehan Yoo**, J. Shaver, S. H. Oh, L. R. Pease, M. Rodriguez. “A natural human IgM that binds to gangliosides is therapeutic in murine models of amyotrophic lateral sclerosis,” *Dis. Model. Mech.* **2015**, 8, (8), 831-842.

Chapter 1

Introduction

1.1 Engineering optical metallic nanostructure

In 1998, Thomas Ebbesen and his co-workers reported that light transmission can be dramatically enhanced through a metal film perforated with a periodic array of subwavelength holes, which is called extraordinary optical transmission (EOT).¹ Surface plasmon polaritons (SPP) formed by coupling light with free electrons on the metal surface were suggested as the primary mechanism in EOT. The discovery of the EOT effect has triggered a great deal of research to understand the underlying physics as well as to harness the effect for practical applications. Various plasmonic metallic nanostructures have been designed and demonstrated to achieve light field enhancement. Among these, periodic metallic nanohole arrays have been studied extensively,²⁻⁴ due in part to their potential utility for surface-based biosensing applications.⁵ A bull's eye structure with a single hole surrounded by circular gratings can enable directional out-coupling of light to further boost the EOT effect.^{6, 7} Sharp metallic tips have also been employed in near-field scanning optical microscopes (NSOM),⁸ enhancing nonlinear optical effects^{9, 10} with strong confinement of light at the tip.¹¹⁻¹³ In the fields of plasmonics and nanophotonics, sharper and smaller metallic nanostructures have been required to achieve stronger field confinement. Along these lines, metallic nanogaps are one of the key building blocks for plasmonic devices. If two metal surfaces approach each other with nanometer-scale spacing, extremely strong field confinement of light into a nanometric volume is made possible through a gap plasmon mode induced by the coupling of two SPPs inside a metal-insulator-metal (MIM) structure.¹⁴ Indeed, gap plasmons have been harnessed for nonlinear optics,¹⁵ light trapping,^{14, 16} surface-enhanced Raman spectroscopy (SERS),¹⁷ and surface-enhanced IR absorption (SEIRA).¹⁸ In addition to the shape of plasmonic nanostructures, the way light behaves with metallic nanostructures can be engineered through the arrangement of plasmonic nanoparticles. Split-ring-type metamaterials have demonstrated a negative refractive index, which does not exist in nature.^{19, 20} Metallic nanorods can act as optical antennas and efficiently couple light from visible to mid-IR frequencies,²¹ and have been used for applications in SEIRA.²² As introduced above, the behavior of light at metallic structures has been engineered morphologically as well as structurally by state-of-the-art nanotechnology, allowing us to explore various new phenomena.

1.2 State-of-the-art nanotechnology

The field of plasmonics has evolved along with advances in nanofabrication technology, because the subwavelength nature of plasmonic devices requires state-of-the-art nanotechnology to pattern nanometer-scale features. Focused-ion beam (FIB) milling has been widely used to carve various nanoscale patterns on metal surfaces.^{23, 24} However, such maskless-type lithography is less productive because it yields serial patterning rather than parallel patterning. Also, the contamination of Ga ions during ion milling may result in unwanted damping of SPP.²⁵ Electron-beam (e-beam) lithography is another powerful maskless-type technique.²⁶ A combination of this technique with various types of e-beam resist has been widely implemented in plasmonic and nanophotonics research despite being a low throughput method.²⁵ In the last decade, nanoimprint lithography has allowed researchers to produce metallic nanostructures with high throughput at a low cost.²⁷ Such lithographic tools have proven to be powerful tools capable of accomplishing a wide variety of high-quality Si nanostructures with the help of dry and wet etching techniques like reactive-ion etching (RIE), ion milling, and crystal-orientation-dependent etching.²⁵ However, because it is very difficult to pattern metals using the above mentioned techniques, they have been limited to Si substrate. More recently, template stripping, a novel technique of duplicating high-quality metallic nanostructures from Si templates patterned using various Si semiconductor fabrication techniques, was successfully demonstrated to improve the lifetime of SPPs by reducing metallic loss.²⁸ This versatile technique has paved the way for producing various high quality, low cost plasmonic metallic nanostructures with high throughput.

Additionally, in the microelectronics industry, the atomic layer deposition (ALD) technique has been developed for the application of high-k dielectrics such as TiO_2 , HfO_2 , Al_2O_3 , and ZrO_2 .²⁹ ALD is a thin-film deposition technique performed by cyclic processes of two precursor exposures.³⁰ The reaction of each precursor is self-saturated within atomic layer thickness, thus enabling the deposition rate to be controlled by the number of process cycles with atomic-scale resolution. ALD has recently been used in atomic layer lithography to pattern vertically-oriented metallic nanogaps via conformal coating on the sidewalls of metal patterns and following metal evaporation.^{31, 32} In this technique, the metallic nanogap size is controlled by the ALD-grown, thin-film thickness. Such sub-10-nm metallic nanogap loops, produced by using atomic layer lithography, have demonstrated extremely high field enhancement, squeezing THz waves into a few nanometric metallic gaps.³²

1.3 Limits of current technology

Atomic layer lithography has opened the door to reliable experiments with sub-10-nm metallic apertures. Combined with conventional photolithography, the versatile technique creates very long and uniform sub-10-nm coaxial gaps, leading to strong resonance at THz.^{32, 33} In order to maintain the sub-10-nm gap sizes required for extreme field enhancements and enable operation at visible and infrared (IR) frequencies, the diameter of the coaxial resonator must be reduced by ~100-fold. However, tape-peeling-planarization-based atomic layer lithography was restricted to either reducing the loop size or increasing pattern density due to a reduction in the contact area where should be attached. Furthermore, simple single nanogap structures have broader and weaker resonance despite strong coupling of light.

1.4 Scope of this dissertation

This dissertation starts by reviewing the limitations of current technologies discussed above. The thesis consists of three main parts, divided according to the type of plasmonic structure. The first part of the dissertation presents a new approach to overcome the miniaturization challenge to construct ultra-compact, high-aspect-ratio coaxial nanocavities with nanogaps. Using the resulting large-area coaxial nanogap apertures, novel phenomena such as the epsilon-near-zero (ENZ) effect at the cutoff frequency, supercoupling of light, and the slow light effect are explored numerically and then experimentally. In the second part, I introduce the integration of atomic layer lithography with the addition photolithography to create a novel trench resonator with a nanogap aperture, which can act as a high-quality plasmonic resonator. In addition, I investigate bright-mode and dark-mode plasmons in this resonator geometry. Then, I outline our efforts using a trench resonator with a nanogap aperture as a two-terminal device or electrodes to perform dielectrophoresis (DEP)-enhanced plasmonic biosensing. The third portion presents additional work performed during the dissertation research, including work with stretchable plasmonic devices and three-dimensional integration of metallic nanostructures. The last chapter offers future research directions to integrate active media with metallic nanogap structures.

1.4.1 Outline of chapters

This dissertation is organized into the following chapters, each outlining a significant portion of the original research performed throughout the dissertation.

- **Chapter 2** introduces the fundamental theory necessary for understanding the optical properties of metals and surface plasmons. It also summarizes the recent progress in EOT as well as ENZ metamaterials.
- **Chapter 3** describes enhanced optical transmission from coaxial nanoapertures via ENZ conditions at cutoff frequency. A novel approach to fabricating ultrasmall coaxial nanocavities is introduced and ENZ properties of coaxial nanocavities are demonstrated experimentally and numerically.
- **Chapter 4** presents an integration of atomic layer lithography with additional photolithography to create a novel trench resonator with a nanogap aperture. Fano resonances and a dark mode in the trench resonator structure are investigated numerically and experimentally.
- **Chapter 5** suggests a new platform for DEP-enhanced plasmonic biosensing. A trench resonator with a nanogap aperture can act as electrodes. SPR sensors detect active trapping or de-trapping of nanometer-scale particles or molecules via the DEP force generated from the nanogap.
- **Chapter 6** introduces other progress made during the duration of the dissertation research, such as work with stretchable plasmonic devices and three-dimensional integration of metallic nanostructures.
- **Chapter 7** summarizes all of the work presented throughout the dissertation and suggests future directions for nanogap-based plasmonic structures.

Chapter 2

Theoretical background

In this chapter, the fundamental understanding of light-matter interaction will be first described via Maxwell's equations and the Lorentz and Drude models. Next, the special case of light-metal interactions such as surface plasmons will be discussed. Finally, the chapter will outline the theoretical basis for understanding the extraordinary optical transmission effect via nanoaperture array and supercoupling through the ENZ effect.

2.1 The optical properties of materials

2.1.1 Maxwell's equations

Maxwell's equations are a set of partial differential equations that describe the propagation of electromagnetic waves. These fundamental equations describe how electric and magnetic fields evolve over time, interact with each other, and are influenced by objects. In a medium with free charge and current, Maxwell's equations take the following forms:

$$\nabla \cdot \mathbf{D} = \rho_f \quad (2.1)$$

$$\nabla \cdot \mathbf{B} = 0 \quad (2.2)$$

$$\nabla \times \mathbf{E} = -\frac{\partial \mathbf{B}}{\partial t} \quad (2.3)$$

$$\nabla \times \mathbf{H} = \mathbf{J}_f + \frac{\partial \mathbf{D}}{\partial t} \quad (2.4)$$

where \mathbf{E} (Volts per Meter) and \mathbf{H} (Amperes per Meter) are the electric and the magnetic field intensities, respectively. In materials, the two Auxiliary fields, \mathbf{D} (Coulombs per square Meter) and \mathbf{B} (Teslas), are the electric flux density and the magnetic flux density, respectively, and are defined as

$$\mathbf{D} = \epsilon \mathbf{E} \quad (2.5)$$

$$\mathbf{B} = \mu \mathbf{H} \quad (2.6)$$

$$\epsilon = \epsilon_r \epsilon_0 \quad (2.7)$$

$$\mu = \mu_r \mu_0 \quad (2.8)$$

where, ϵ_0 and μ_0 are the electric permittivity and the magnetic permeability of free space. ϵ_r and μ_r are the relative permittivity and permeability of materials. Since non-magnetic materials are only considered in this dissertation, we will set $\mu_r = 1$.

2.1.2 Light: the wave equation

Maxwell's equations are coupled, first-order, partial differential equations that can be decoupled by taking the curl (2.3), and generating the following wave equation:

$$\nabla^2 \mathbf{E} - \epsilon_0 \mu_0 \frac{\partial^2 \mathbf{E}}{\partial t^2} = \mu_0 \frac{\partial \mathbf{J}_f}{\partial t} + \mu_0 \frac{\partial^2 \mathbf{P}}{\partial t^2} - \frac{1}{\epsilon_0} \nabla(\nabla \cdot \mathbf{P}) \quad (2.9)$$

In this inhomogeneous wave equation, the source terms on the right-hand side (RHS) describe the origin of emitting light. The first term on the RHS depicts the currents of free charges, which are important for determining the reflection of light from a metallic surface or for determining the propagation of light in a plasma. The second term on the RHS means dipole oscillations, which behave similarly to currents. The final term on the RHS can be ignored in isotropic media because it is polarization. For an electromagnetic wave propagating in a vacuum, all of the terms on the RHS are zero, in which the wave equation can reduce to

$$\nabla^2 \mathbf{E} = \epsilon_0 \mu_0 \frac{\partial^2 \mathbf{E}}{\partial t^2} \quad (2.10)$$

$$\nabla^2 \mathbf{B} = \epsilon_0 \mu_0 \frac{\partial^2 \mathbf{B}}{\partial t^2} \quad (2.11)$$

Magnetic field \mathbf{B} is derived in equation 2.11 in the same manner as electric field \mathbf{E} . In the simple homogeneous wave equation, plan wave solutions for electromagnetic waves are written simply as the complex sinusoidal wave form

$$\mathbf{E}(\mathbf{r}, t) = \mathbf{E}_0 e^{i(\mathbf{k} \cdot \mathbf{r} - \omega t)} \quad (2.12)$$

$$\mathbf{B}(\mathbf{r}, t) = \mathbf{B}_0 e^{i(\mathbf{k} \cdot \mathbf{r} - \omega t)} \quad (2.13)$$

The resultant solution depicts waves with an angular frequency ω and a wavevector \mathbf{k} propagating at speed $c = 1/\sqrt{\epsilon_0 \mu_0}$, the speed of light in vacuum. Here, the wave vector \mathbf{k} is defined as

$$\mathbf{k} = k\hat{\mathbf{u}} = \frac{2\pi}{\lambda_{\text{vac}}}\hat{\mathbf{u}} \quad (2.14)$$

The frequency (ω) of oscillation is related to the wavelength via

$$\omega = \frac{2\pi c}{\lambda_{\text{vac}}} \quad (2.15)$$

The wave equation requires them to be related through the dispersion relation, leading to

$$k = \frac{\omega}{c} \quad (2.16)$$

It is important to note that \mathbf{E}_0 , \mathbf{B}_0 and ω are not independently chosen in equations 2.12 and 2.13. In order to satisfy Faraday's law (2.4), they must be identical. Therefore, in a vacuum, the electric and magnetic fields travel in phase and Faraday's law requires

$$\mathbf{B}_0 = \frac{\mathbf{k} \times \mathbf{E}_0}{\omega} \quad (2.17)$$

The above cross product means that \mathbf{B}_0 is perpendicular to both \mathbf{E}_0 and \mathbf{k} . Meanwhile, Gauss law $\nabla \cdot \mathbf{E} = 0$ requires \mathbf{k} to be perpendicular to \mathbf{E}_0 , which shows how electromagnetic waves propagate. That is, electromagnetic waves are transverse: the electric and magnetic fields are perpendicular to the direction of propagation.

In a linear isotropic and homogeneous dielectric medium (i.e. $\mathbf{J}_{\text{free}} = 0$), the second term in the RHS of equation 2.9 only plays a role as a source and equation 2.9 is reduced to

$$\nabla^2 \mathbf{E} - \epsilon_0 \mu_0 \frac{\partial^2 \mathbf{E}}{\partial t^2} = \mu_0 \frac{\partial^2 \mathbf{P}}{\partial t^2} \quad (2.18)$$

In a linear medium under an applied electric field, the polarization amplitude (\mathbf{P}) is proportional to the strength of the applied electric field. Proportionality factor χ is called the susceptibility, which depends on the frequency of the field as

$$\mathbf{P}_0 = \chi(\omega)\epsilon_0 \mathbf{E}_0 \quad (2.19)$$

By substituting $\mathbf{P}_0 = \chi(\omega)\epsilon_0\mathbf{E}_0$, $\mathbf{E} = \mathbf{E}_0e^{i(\mathbf{k}\cdot\mathbf{r}-\omega t)}$, and $\mathbf{P} = \mathbf{P}_0e^{i(\mathbf{k}\cdot\mathbf{r}-\omega t)}$ into equation 2.18 and canceling the field term, we obtain the dispersion relation in dielectric:

$$k = \frac{\omega}{c}\sqrt{1 + \chi(\omega)} \quad (2.20)$$

Therefore, in general, a complex index of refraction is defined by

$$\mathcal{N}(\omega) \equiv n(\omega) + i\kappa(\omega) = \sqrt{1 + \chi(\omega)} \quad (2.21)$$

where n and κ are the real and imaginary parts of the index respectively. The index of refraction (\mathcal{N}) describes the response of electrons in the material to the passing electric field wave. n determines the phase velocity (λ_v) and κ affects the absorption in medium.

2.1.3 Lorentz model of dielectric

In a medium, electrons excited by the electric field of light experience fluctuation with distance (x_e) whose the electron charge depends on the local strength of the applied electric field. Such perturbation results in polarization, which can be expressed as $\mathbf{P} = Nq\mathbf{x}_e$. The behavior of electrons in a medium in relation to the electric field can be modeled and computed using Newton's equation of motion as follows:

$$m_e \frac{d^2\mathbf{x}_e}{dt^2} + m_e\gamma \frac{d\mathbf{x}_e}{dt} + m_e\omega_0^2\mathbf{x}_e = q\mathbf{E}_0e^{i(\mathbf{k}\cdot\mathbf{r}-i\omega t)} \quad (2.22)$$

This harmonic oscillator equation includes three force terms. The second term on the LHS is the viscous drag force which is opposite to the electron motion and explains the absorption of energy due to collisions with electrons. The third term on the LHS is the restoring force which arises from the electrons bound to the nucleus. The RHS is the electric field that electrons experience. The inhomogeneous solution to equation 2.22 becomes:

$$\mathbf{x}_e(t) = \left[\frac{q}{\omega_0^2 - \omega^2 - i\omega\gamma} \right] \mathbf{E}_0 e^{i(\mathbf{k}\cdot\mathbf{r} - i\omega t)} \quad (2.23)$$

The electrons oscillate with the same frequency ω as the driving electric field. The imaginary part in the denominator implies that the electrons can oscillate with phases different from the electric field oscillations. The damping term γ causes the two to be out of phase. This shape is the complex Lorentzian. Therefore, it is possible to write the polarization in terms of the electric field such as

$$\mathbf{P} = \epsilon_0 \left[\frac{\omega_p^2}{\omega_0^2 - \omega^2 - i\omega\gamma} \right] \mathbf{E}_0 e^{(\mathbf{k}\cdot\mathbf{r} - i\omega t)} \quad (2.24)$$

where the plasma frequency ω_p is defined as $\omega_p \equiv \sqrt{\frac{Nq^2}{\epsilon_0 m_e}}$.

A comparison of 2.19 and 2.24 reveals the susceptibility:

$$\chi(\omega) = \frac{\omega_p^2}{\omega_0^2 - \omega^2 - i\omega\gamma} \quad (2.25)$$

The index of refraction is then expressed as the following:

$$\epsilon(\omega) = [n(\omega) + i\kappa(\omega)]^2 = 1 + \chi(\omega) = 1 + \frac{\omega_p^2}{\omega_0^2 - \omega^2 - i\omega\gamma} \quad (2.26)$$

2.1.4 Drude model of metals

In a metal, conduction electrons are subject to a damping force due to collisions that remove energy and give rise to absorption of light while the outer electrons of atoms are free to move without being tethered to any particular atom. Movement of free electrons without the restoring force mimics the behavior of a free current \mathbf{J}_{free} . The dielectric function of metal can be derived from the context \mathbf{J}_{free} . In a conduction medium, equation 2.9 loses a polarization term and the wave equation is

$$\nabla^2 \mathbf{E} - \epsilon_0 \mu_0 \frac{\partial^2 \mathbf{E}}{\partial t^2} = \mu_0 \frac{\partial \mathbf{J}_f}{\partial t} \quad (2.27)$$

The assumption that the current arises from individual electrons traveling with velocity \mathbf{v}_e leads to

$$\mathbf{J}_f = Nq\mathbf{v}_e \quad (2.28)$$

The electrons satisfy Newton's equation of motion without a restoring force:

$$m_e \frac{d^2 \mathbf{x}_e}{dt^2} + m_e \gamma \frac{d\mathbf{x}_e}{dt} = q\mathbf{E}_0 e^{(\mathbf{k}\cdot\mathbf{r} - i\omega t)} \quad (2.29)$$

The solution of equation 2.29 is

$$\mathbf{v}_e = \frac{d\mathbf{x}_e}{dt} = \left(\frac{q}{m_e}\right) \frac{1}{\gamma - i\omega} \mathbf{E}_0 e^{(\mathbf{k}\cdot\mathbf{r} - i\omega t)} \quad (2.30)$$

The current density in terms of the electric field is then

$$\mathbf{J}_f = e \left(\frac{Nq^2}{m_e}\right) \frac{1}{\gamma - i\omega} \mathbf{E}_0 e^{(\mathbf{k}\cdot\mathbf{r} - i\omega t)} \quad (2.31)$$

By substituting this and the electric field into the wave equation 2.27 and canceling the electric field term, the dispersion relation in metal is

$$k^2 = \frac{\omega^2}{c^2} \left(1 - \frac{\omega_p^2}{\omega^2 + i\omega\gamma}\right) \quad (2.32)$$

Therefore, the dielectric function of metal is expressed as

$$\varepsilon(\omega) = \varepsilon_1 + i\varepsilon_2 = 1 + \chi(\omega) = 1 - \frac{\omega_p^2}{\omega^2 + i\omega\gamma} \quad (2.33)$$

This is the Drude model to describe the dielectric function of metal.

In the low frequency ($\omega \ll \gamma$), the current density (equation 2.31) reduces to Ohm's law $\mathbf{J} = \sigma\mathbf{E}$, where $\sigma = \frac{Nq^2}{m_e\gamma}$ is the DC conductivity. In the high frequency limit ($\omega \gg \gamma$), the behavior changes over to that of a free plasma, where collisions, which are responsible for resistance, become very small. The dielectric function of metal can be simplified to $\varepsilon(\omega) = 1 - \frac{\omega_p^2}{\omega^2}$, which is called a non-lossy Drude model. The optical property has a transition at plasma frequency (ω_p). For $\omega > \omega_p$, the materials behave as dielectric media. For $\omega < \omega_p$, however, the materials become metallic and have the real and imaginary parts of dielectric function as follows:

$$\varepsilon_1(\omega) = 1 - \frac{\omega_p^2\tau^2}{1 + \omega^2\tau^2} \quad (2.34)$$

$$\varepsilon_2(\omega) = \frac{\omega_p^2\tau}{\omega(1 + \omega^2\tau^2)} \quad (2.35)$$

where $\tau = 1/\gamma$, which is defined as the average time between the collisions of free electrons.

2.2 Plasmonics

Optical properties of metal can be described by the response of conduction electrons to the electromagnetic field. In the specific frequency regime ($\omega < \omega_p$), the free electron gas in a metal behaves as plasma, a gas composed of charged particles that respond collectively to electromagnetic fields. Therefore, the study of optical phenomena related to the electromagnetic response of metals has been termed plasmonics. At optical frequencies, metals such as gold and silver have an imaginary index of refraction, which gives rise to non-radiative modes unlike light in a dielectric. The resulting highly confined waves at the subwavelength scale enable the study of the manipulation of light localization and propagation on the nanometer scale.

2.2.1 Surface Plasmon Polaritons

Surface plasmon polaritons (SPPs) are electromagnetic waves coupled to surface charge density oscillation and propagating at the interface between a dielectric and a metal, evanescently confined in the perpendicular direction.^{35, 36} Figure 2.1 shows the characteristics of SPPs, which we will discuss in this section.

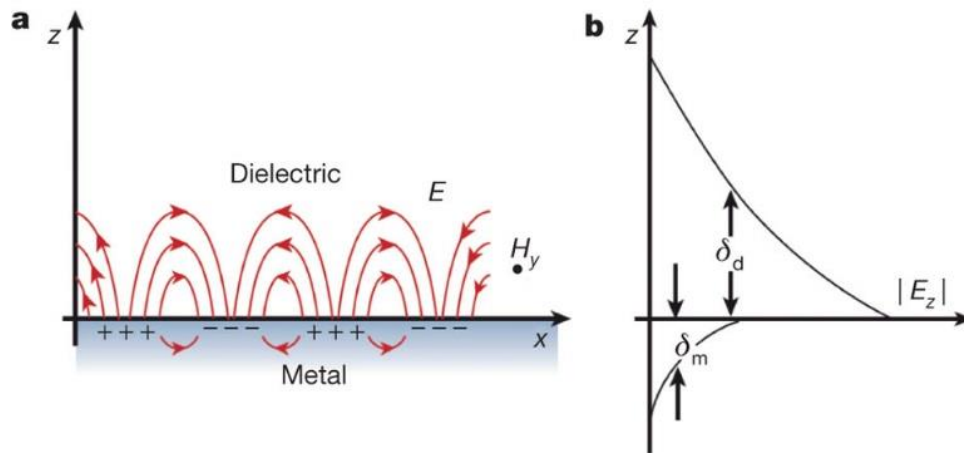


Figure 2.1 Characteristics of surface plasmon polaritons. (a) SPPs as a collective excitation at a metal–dielectric interface. The electromagnetic field (electric field, E , plotted in the z – x plane; magnetic field, H_y , sketched in the y direction) is drastically confined at the interface. (b) The perpendicular field E_z decays exponentially with a characteristic length of δ_d (of the order of the optical wavelength) in the dielectric and a characteristic length of δ_m (the skin depth) in the metal. Reprinted with permission from Barnes *et al.*³⁶ Copyright 2003 Macmillan Publishers

In a classical picture, SPPs are a particular solution of Maxwell's equations that appear for certain boundary conditions. Inserting $\mathbf{E}(\mathbf{r}, \mathbf{t}) = \mathbf{E}(\mathbf{r})e^{-i\omega t}$ into the wave equation with a condition of no free charge and current yields

$$\nabla^2 \mathbf{E} + k_0^2 \epsilon \mathbf{E} = 0 \quad (2.36)$$

Next, by considering a p-polarized plan wave form (TM wave) and boundary conditions such as conservation of the wavevector parallel to the surface, and continuity of the parallel component of \mathbf{E} and the perpendicular component of \mathbf{D} between the dielectric and metal, we obtain three relation equations as follows:

$$k_x^2 + k_{d,z}^2 = \epsilon_d k^2 \quad (2.37)$$

$$k_x^2 + k_{m,z}^2 = \epsilon_m k^2 \quad (2.38)$$

$$\epsilon_d k_{m,z} - \epsilon_m k_{d,z} = 0 \quad (2.39)$$

The combination of these three equations yields dispersion relations of the wavevector k_x along the propagating direction and the normal component of the wavevector k_y with the angular frequency ω , respectively:

$$k_x^2 = \frac{\epsilon_d \epsilon_m}{\epsilon_d + \epsilon_m} \frac{\omega^2}{c^2} \quad (2.40)$$

$$k_{j,z}^2 = \frac{\epsilon_j^2}{\epsilon_d + \epsilon_m} \frac{\omega^2}{c^2} \quad (j = d, m) \quad (2.41)$$

We define SPPs as surface waves propagating along the x direction, exponentially decaying to the z direction. To meet the characteristics of a propagating evanescent field, k_x should be real and k_y has to be purely imaginary. From this, the conditions for a surface mode to exist are as follows:

$$\epsilon_d(\omega) \cdot \epsilon_m(\omega) < 0 \quad (2.42)$$

$$\epsilon_d(\omega) + \epsilon_m(\omega) < 0 \quad (2.43)$$

which results in $\epsilon_m = \epsilon'_m + i\epsilon''_m$, $\epsilon'_m < 0$, $|\epsilon'_m| > \epsilon''_m$, $|\epsilon'_m| > \epsilon_d$.

In particular, we can observe such conditions in novel metals such as gold and silver at optical frequencies, which is why they are popular and useful in plasmonics. The propagation constant

($k_{\text{SPP}} = k'_{\text{SPP}} + ik''_{\text{SPP}}$) of SPPs includes much information about their optical properties. First is the surface plasmon wavelength. The SPP wavelength can be determined by the real component k'_{SPP} , while the imaginary part k''_{SPP} describes the damping (ohmic losses) of the SPP as it propagates along the interface.

$$k'_{\text{SPP}} = \left(\frac{\epsilon_d \epsilon'_m}{\epsilon_d + \epsilon'_m} \right)^{1/2} \frac{\omega}{c} \quad (2.44)$$

$$k''_{\text{SPP}} = \left(\frac{\epsilon_d \epsilon'_m}{\epsilon_d + \epsilon'_m} \right)^{3/2} \frac{\epsilon''_m}{2\epsilon'^2_m} \frac{\omega}{c} \quad (2.45)$$

Thus, the SPP wavelength is obtained from k'_{SPP} as the following and the plasmon wavelength is always shorter than the wavelength in the dielectric medium:

$$\lambda_{\text{SPP}} = \frac{2\pi}{k'_x} = \left(\frac{\epsilon_d + \epsilon'_m}{\epsilon_d \epsilon'_m} \right)^{1/2} \lambda \quad (2.46)$$

Next, we can calculate the surface plasmon evanescent field decay length using the normal component of wavevector (k_z) shown in Figure 2.1b. Given equation 2.12, the distance at which the field falls to $1/e$ becomes

$$\delta_d = \left(\frac{\epsilon_d + \epsilon'_m}{\epsilon_d^2} \right)^{1/2} \frac{\omega}{c} \quad (2.47)$$

$$\delta_m = \left(\frac{\epsilon_d + \epsilon'_m}{\epsilon'^2_m} \right)^{1/2} \frac{\omega}{c} \quad (2.48)$$

2.2.2 Excitation of surface plasmon polaritons

In order to excite SPPs, we have to fulfill the conservation of both energy and momentum. Given the dispersion relation of SPPs (2.44), the wavevector k_{SPP} is always larger than that of light in free space. Therefore, light in free space cannot excite SPPs directly due to the mismatch of momentum. Figure 2.2 shows the dispersion curves of SPPs and free-space light.

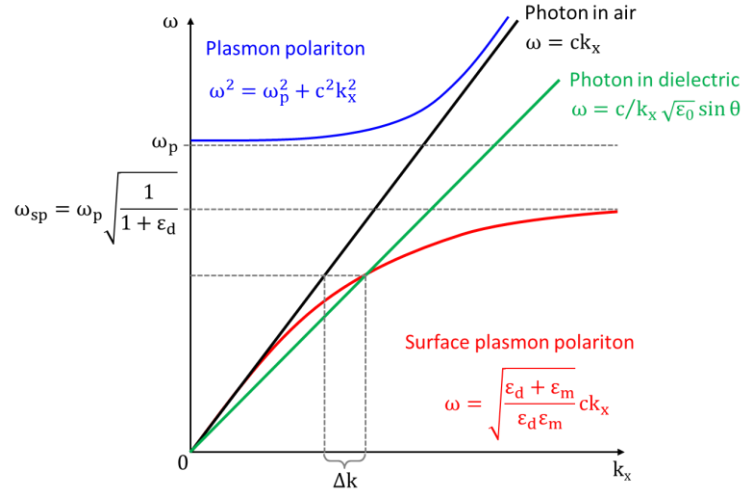


Figure 2.2 Dispersion relation of surface plasmon polaritons at a dielectric-metal interface.

There are many techniques to match the momentum between SPPs and light in free space. Here, I will introduce the two methods shown in Figure 2.3. The Kretschmann configuration³⁷ is well known as the simple way to launch SPPs. In this setup, a metallic, thin-film-coated prism with high index of refraction is used to generate an evanescent field to the metal side through the total internal reflection condition. The resulting evanescent field with large wavevector due to high index can excite the SPPs at the interface between air and a metal. A grating coupler is an alternative way to launch SPPs.³⁵ Grating with a period p_0 gives a reciprocal lattice vector ($\mathbf{G} = 2\pi/p_0$) to a wavevector of light in free space, yielding the increase of the wavevector required to match the momentum:

$$\mathbf{k}_{\text{spp}} = \mathbf{k}_0 + m\mathbf{G} \quad (2.49)$$

where m is integers and \mathbf{G} is the reciprocal lattice vector. This approach can give us a degree of freedom to study the behavior of light at nanometer scale by engineering the geometry of grating with advanced nanotechnology. This is crucial to this thesis in which a variety of nanoplasmonic structures are introduced and their characteristics explored.

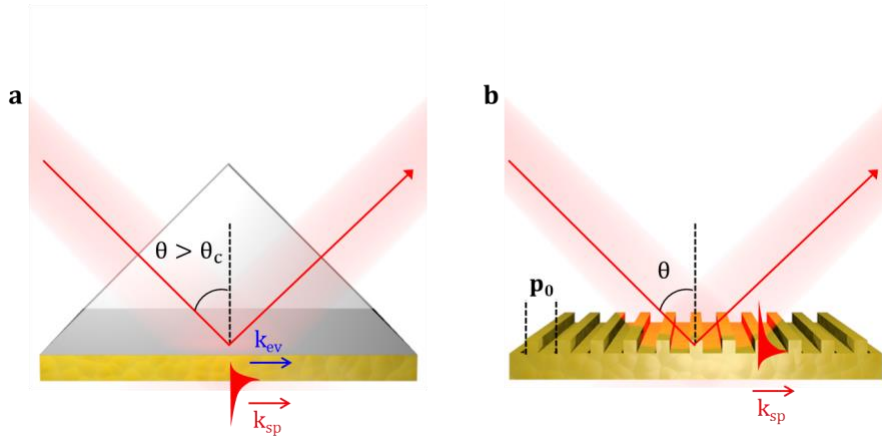


Figure 2.3 Excitation of surface plasmon polaritons. (a) Schematic representation of SPP excitation (Kretschmann configuration) in which the plasmon mode propagates into a metal film adjacent to a prism. The incident angle should be accurately chosen so as to phase-match the momentums of the illuminated light and the SPP. (b) Excitation of an SPP can be coupled with the light diffraction on a grating.

2.3 Gap plasmon

SPPs propagating along two opposite interfaces of a metal-insulator-metal (MIM) structure can couple with each other and form a mode known as a gap plasmon, which can lead to strong field enhancement as the distance between the two interfaces decreases.³⁸ As depicted in Figure 2.4, when two SPPs get closer than the decay length (around 100 nm), they start to couple with each other, diverging into two different modes such as symmetric and anti-symmetric modes. Such singular dispersive properties are analyzed with the dispersion relation in the MIM structure. The eigenmode of the planar MIM structure can be solved using the wave equation under the boundary condition of H_y and E_x field continuity.³⁹ The dispersion relation in the MIM structure is defined as:

$$e^{-2k_d a} = \pm \frac{k_d/d + k_m/\epsilon_m}{k_d/\epsilon_d - k_m/\epsilon_m} \quad (2.50)$$

This branches off into two different modes like symmetric and anti-symmetric modes according to the sign as follows:

$$\frac{k_m \epsilon_d}{k_d \epsilon_m} = -\tanh(k_d a) : \text{symmetric mode} \quad (2.51)$$

$$\frac{k_d \epsilon_m}{k_m \epsilon_d} = -\tanh(k_d a) : \text{anti-symmetric mode} \quad (2.52)$$

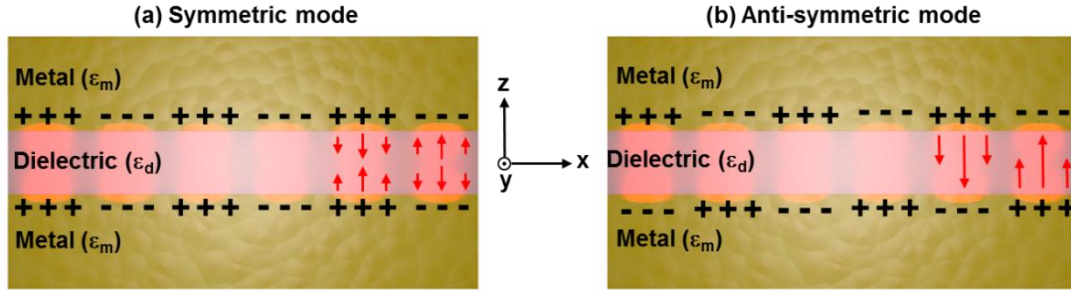


Figure 2.4 Two dispersion modes of gap plasmons in a metal-insulator-metal (MIM) waveguide. As the gap distance decreases, SPPs at the two interfaces couple with each other, generating gap plasmons with strong field enhancement. The type of dispersion mode depends on how the electric field is distributed inside the MIM waveguide such as (a) and (b).

The deviation in the dispersion of SPPs in an MIM structure from that in a single metallic interface is shown in Figure 2.5. If the distance between the two interfaces is large enough, the coupling between SPP waves is weak and the dispersion curve is nearly identical to one of the SPPs at the single interface. As the distance becomes comparable to the perpendicular SPP decay length, however, two SPPs are coupled together and split into two modes. The symmetric mode can oscillate at a high frequency because the two SPPs are in-phase while two SPPs coupled out-of-phase (anti-symmetric mode) can oscillate at a low frequency. Therefore, the symmetric mode with a high frequency goes close to the light line. On the other hand, the anti-symmetric mode with a low frequency becomes flat and increases wavevector k as the distance decreases. That is, strong field enhancement with a high effective index can be achieved in the anti-symmetric mode.⁴⁰ Thus, this mode has attracted attention in terms of light-matter interactions such as absorption enhanced spectroscopy⁴¹ and nonlinear optics.¹⁷ But, the absence of reproducible fabrication techniques to make very small MIM gap structures has limited its applications. In this thesis, various methods to fabricate MIM nanogaps will be introduced.

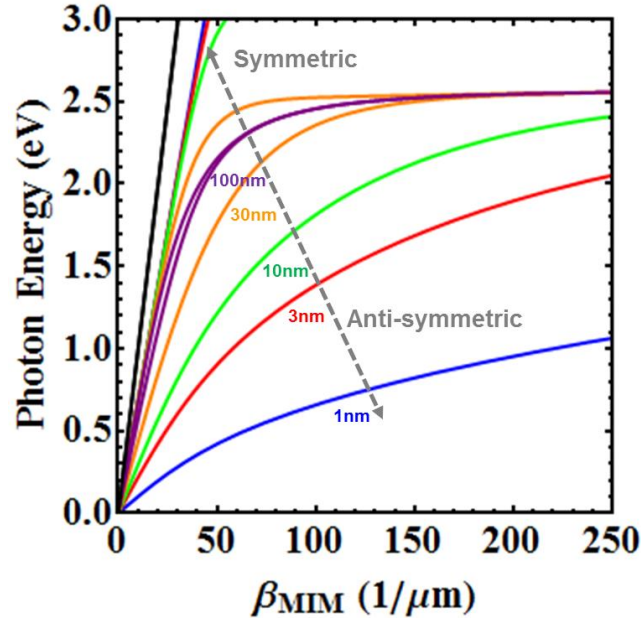


Figure 2.5 Dispersion relations of MIM waveguides with different gap sizes like 100nm (purple), 30nm (orange), 10nm (green), 3nm (red), and 1nm (blue). Black line shows dispersion of light in free space.

2.4 Extraordinary optical transmission (EOT)

2.4.1 EOT through a nanohole array

Up to this point, we have concentrated on the discussion of surface plasmon polariton excitation and propagation along the planar surface. Now, I turn our attention to the perpendicular direction and take a look at the transmission of light through a metallic aperture. When light is passing through a single metallic aperture, diffraction arises due to the nature of light. For apertures larger than the wavelength of impinging light ($r \gg \lambda_0$), the Huygens-Fresnel principle takes the transmission coefficient into account. For subwavelength apertures ($r \ll \lambda_0$), the diffraction of light through an aperture can be understood by Bethe's aperture theory.⁴² The transmission coefficient for an incident plane wave is then given by

$$T = \frac{64}{27\pi^2} (kr)^4 \propto \left(\frac{r}{\lambda_0}\right)^4 \quad (2.53)$$

It is shown that transmission intensity via subwavelength aperture decreases at the fourth power of the aperture size (r). That is, this model is limited to apertures which only allow the decaying mode because Bethe's description of transmission through a subwavelength aperture relies on two major assumptions such as infinitely thin, but perfectly opaque, metallic apertures due to infinite conductivity.

In 1998, Ebbesen and his co-workers reported that light transmission can be dramatically enhanced through a periodically-perforated metallic thin film with finite conductivity, which they named extraordinary optical transmission (EOT).¹ This observation was surprising because Bethe's theory predicts very small optical transmission when the aperture size, r , is much smaller than the free-space wavelength ($r \ll \lambda_0$). Since this discovery, EOT has triggered a great deal of research exploring the underlining physics as well as practical applications. In the initial understanding of EOT, an incident light can be converted into SPPs by periodic nanohole grating, leading to a strongly confined light field. SPPs, propagating along the top surface of the metallic nanohole array, then tunnel through the nanoholes, followed by out-coupling of light into the far field on the opposite side. The resulting transmission spectrum shows well-defined resonance at the wavelength where the excitation of SPPs takes place. At this wavelength, transmission normalized by aperture area exceeds unity ($T > 1$). To confirm the assumption that SPPs play a critical role in enhancing light intensity, the dispersion relation of grating-coupled SPPs with different incident angles was investigated, which derived the phase matching condition²

$$\beta = k_x \pm nG_x \pm mG_y = k_0 \sin \theta \pm (n + m) \frac{2\pi}{a_0} \quad (2.54)$$

where β is the SPP propagating constant, $G_{x,y}$ is a reciprocal lattice given by $2\pi/a_0$, and n and m are integers to account for the grating diffraction order. By combining equations 2.43 and 2.54, the wavelengths at which transmission maxima occur were approximated as follows:²

$$\lambda_{\text{spp}}(n, m) = \frac{a_0}{\sqrt{n^2 + m^2}} \sqrt{\frac{\epsilon_m \epsilon_d}{\epsilon_m + \epsilon_d}} \quad (2.55)$$

Figure 2.6 shows a spectrum of multiple resonances via a silver metallic nanohole array with normal incident light. Each resonance mode can be identified using equation 2.55. After this first approximation, others interested in EOT effects have demonstrated that geometric factors such as

the periodicity of hole array,^{1, 4} hole size and shape,^{43, 44, 45} and the thickness of the metal film⁴ can play a critical role in EOT effects. In particular, some studies claim that hole cavity resonance can be mainly attributed to EOT rather than SPPs.^{46, 47} While many experiments and analytic modeling have supported the role of SPPs in the EOT effect, there have been trials to understand the EOT effect as purely geometric,⁴⁸ without the possibility of SPP excitation. EOT has also been interpreted as the result of frequency selective surface (FSS) components in the spectral region from near-infrared to microwave frequencies, which is associated with the Rayleigh-Wood anomaly.^{34, 49, 50} This states that a transmission minimum occurs at the wavelength where $\lambda_{\min} = na_0$, when incident light is diffracted parallel to a periodically-corrugated surface with periodicity of a_0 . In spite of such controversy, it is generally accepted that the constructive interference between non-resonant directly-transmitted light and resonant grating-coupled SPPs⁵¹ results in the transmission maximum and that they interfere destructively at the transmission minimum.^{52, 53} Furthermore, it has been reported that waveguide behavior can enhance the transmission of light without a grating-coupling mechanism such as a circular hole with a diameter above cutoff, one-dimensional slit without cutoff, or annular-shaped aperture.⁵⁴ Therefore, the term EOT is now considered broadly as exceptionally enhanced transmission light regardless of the grating-coupling mechanism.

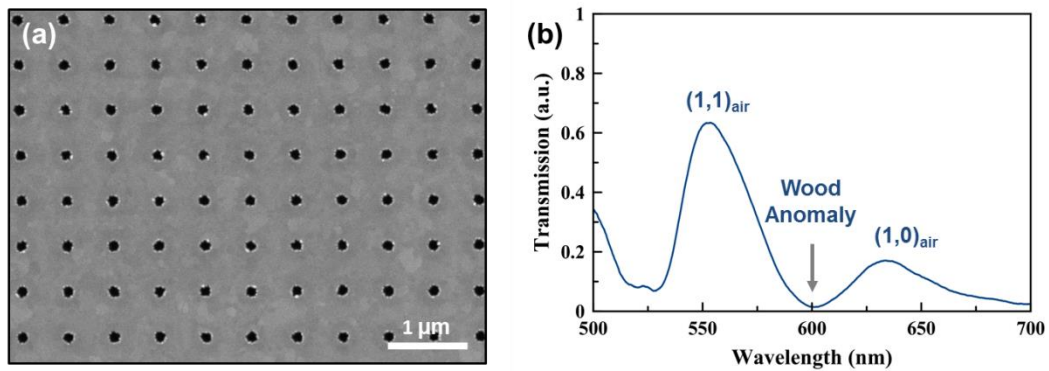


Figure 2.6 EOT through silver nanohole arrays. (a) Silver nanohole array with 600nm period and 120nm diameter. (b) Transmission spectrum measured from silver nanohole array with 600nm period and 120nm diameter.

2.4.2 EOT through coaxial apertures

For EOT mediated by a periodic subwavelength hole array, the peak transmission wavelength is determined by the array periodicity. Thus, a micrometer-scale periodic aperture array is necessary for enhancing transmission in near- or mid-infrared regimes. On the other hand, the guided mode has been used to improve EOT via a single aperture rather than periodic structure. Among various waveguide geometries, coaxial holes^{54, 55} have been of particular interest due to their resemblance to coaxial cables, which can sustain a transverse electromagnetic (TEM) waveguide mode with no cutoff.⁵⁶ Even though a TEM mode can be excited under specific conditions,⁵⁶ it has also been shown that subwavelength coaxial apertures with optimized parameters can transmit more light than circular apertures with the same open area.

These intriguing behaviors of coaxial apertures can be understood by comparing cutoff wavelengths with different types of waveguide structures. Figure 2.7 compares the cutoff wavelengths of the first guided modes for three different kinds of waveguides made in perfectly electric conductor (PEC).

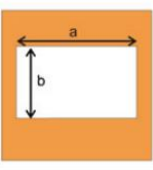


Structures			
First modes	$\lambda_{TM_{11}}^c = \frac{2ab}{\sqrt{a^2 + b^2}}$ $\lambda_{TE_{10}}^c = 2a$	$\lambda_{TE_{11}}^c = \frac{2\pi R}{1.841}$ $\lambda_{TM_{01}}^c = \frac{2\pi R}{2.405}$	$\lambda_{TE_{m1}}^c = \frac{(R_o + R_i)\pi}{m}$ $\lambda_{TE_{mn}}^c = \frac{2(R_o - R_i)}{n - 1}$ $\lambda_{TM_{mn}}^c = \frac{2(R_o - R_i)}{n}$
Examples	$a = b = 250nm$ $\lambda_{TE_{10}}^c = 500nm$	$R = 125nm$ $\lambda_{TE_{11}}^c = 426.6nm$	$R_o = 125nm,$ $R_i = 75nm$ $\lambda_{TE_{11}}^c = 628.3nm$

Figure 2.7 The cutoff wavelengths of the first guided modes for three different kinds of waveguides made in a perfectly electric conductor (PEC). Reprinted with permission from Baida *et al.*⁵⁷ Copyright 2006 American Physical Society.

Three different types of waveguides with the same outer dimension show different cutoff wavelengths depending on the geometrical shape of the waveguide. Among them, the coaxial waveguide supports the largest cutoff wavelength at TE₁₁ waveguide mode. In TE₁₁ mode, the

maximum of the cutoff wavelength can reach $2\pi R_o$, when the inner radius approaches very close to the outer radius, resulting in a very narrow coaxial gap aperture. As a result, the cutoff wavelength in TE_{11} mode is proportional to the sum of the inner and outer radii of a coaxial metallic waveguide with infinity conductivity. However, a real metallic coaxial waveguide with finite conductivity can show different behavior from a PEC one, as shown in Figure 2.8. Cutoff wavelengths from real metal (silver) and PEC coaxial waveguides are compared in Figure 2.8 as the outer radius approaches the fixed inner radius (50nm) of a coaxial waveguide.

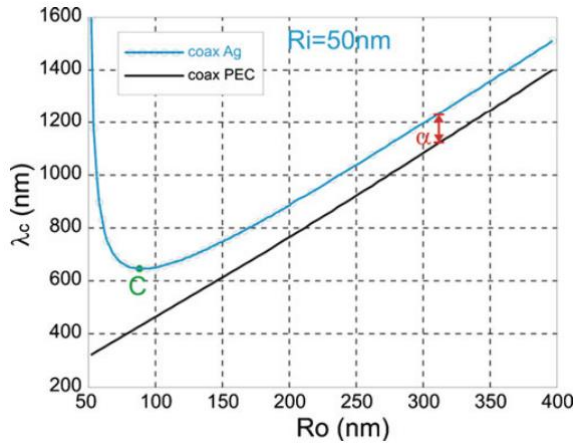


Figure 2.8 Cutoff wavelengths of the TE_{11} mode of both PEC and silver coaxial waveguides. α denotes the red shift introduced by the metal nature in the case of a relatively large dielectric gap. Reprinted with permission from Baida *et al.*⁵⁷ Copyright 2006 American Physical Society.

A coaxial waveguide made with real metal has a larger cutoff wavelength than a PEC waveguide because real metal has a skin depth, which increases the effective aperture size a little bit. Then, as the outer radius decreases from 400nm to 50nm, the two cutoff wavelengths tend to decrease together due to the reduction in the sum of the two radii. However, at an outer radius of 80nm, the two cutoff wavelengths start to diverge from each other. While the cutoff wavelength in the PEC waveguide continues to decrease with the outer radius, the cutoff wavelength in the silver waveguide goes up to a longer wavelength. Such peculiar behavior in a real metal waveguide can be explained by the presence of surface plasmons in real metal because a PEC cannot support surface plasmons. The role of the plasmonic guided mode (TE_{11}) in a real metal coaxial waveguide has been demonstrated in many papers.^{57, 58} Haftel suggested cylindrical surface plasmons as a key concept to enhance optical transmission with increased transmission wavelength. Here, a cylindrical surface plasmon is considered a gap plasmon as discussed above. The inner and outer

interfaces of a coaxial waveguide support SPPs on two interfaces. When the gap distance between the two interfaces is sufficiently small compared to the decay length of the evanescent field, very strong field enhancement inside the gap can arise from the coupling of two opposite SPPs. Strong field enhancement enables the cutoff wavelength of TE_{11} to redshift.

While an isolated circular hole in a metal film only shows a broad transmission peak,⁴⁶ a coaxial aperture can exhibit a series of resonance peaks due to cutoff resonances along its perimeter as well as Fabry-Perot (FP) resonances of waveguide modes across the film as shown in Figure 2.9. At the cutoff wavelength, light waves cannot propagate through the waveguide. The resulting zero-propagation constant causes the effective index of the guided mode to vanish at the cutoff wavelength. Therefore, the cutoff resonance or FP0 is independent of the waveguide length, since this is not a propagation mode unlike FP resonances traveling and built up along the waveguide cavity. Furthermore, the vanishing effective index ($n_{\text{eff}} \ll 1$) makes the wavelength of light inside the waveguide longer than in the air. Thus, the electric field distribution becomes uniform along the waveguide due to no phase shift between the two end faces of the waveguide as illustrated in Figure 2.9. As a result, at a cutoff wavelength, the reduced group velocity inside the coaxial waveguide generates a “slow light” mode, which can significantly enhance the field intensity inside the aperture. Without relying on periodic effects, this intrinsic mode of a single coaxial nano-aperture can show EOT that can be tuned over a broad spectral range and accompanied by strong local fields.^{54, 55, 57}

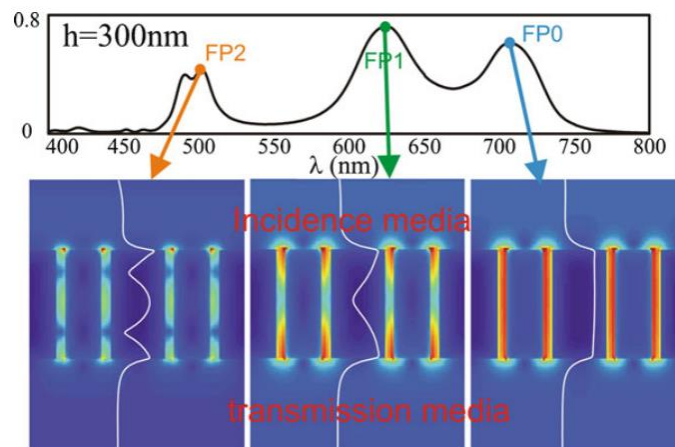


Figure 2.9 Electric field intensity distribution along a longitudinal plane corresponding to the three transmissions peaks of one annular aperture array structure with $h=300\text{nm}$. Note that these three light distributions are separately normalized. Reprinted with permission from Biada *et al.*⁵⁹ Copyright 2012 Springer.

2.5 Epsilon-near-zero (ENZ) phenomenon

Light in matter is affected by the medium in which the light propagates. While the refractive index determines the wavelength of light propagating inside the medium, the absorption of light inside the matter is described by an imaginary part of it. Therefore, the refractive index plays a key role in determining the scattering response of the light to the matter. Recently, metamaterials which can tune a material's permittivity and permeability have attracted tremendous interest in nanophotonics because metamaterials can exhibit singular optical properties which do not exist in nature. A negative refractive index^{19, 20} is one of the most widely studied examples of unusual optical properties in metamaterials. In this thesis, I investigate another interesting metamaterial behavior known as the epsilon-near-zero (ENZ) effect. ENZ material manifests itself as medium having ϵ approaching zero.⁶⁰ In general, dielectrics such as glass have higher permittivity than air, which allows light to be compressed in the medium as shown in Figure 2.10a. That is, the wavelength becomes shorter when light is impinging on the medium. A medium with a negative permittivity behaves as a metallic, reflecting incident light back so there is no propagating of light into the medium. The area of interest is a permittivity lower than 1, but positive. In this zone ($\epsilon \rightarrow 0$), light impinging on the medium can be stretched with lower permittivity as depicted in Figure 2.10a. Increasing the wavelength allows the phase velocity of the wave to increase, which might provide a relatively small phase variation over a physically long distance in these media.⁶¹

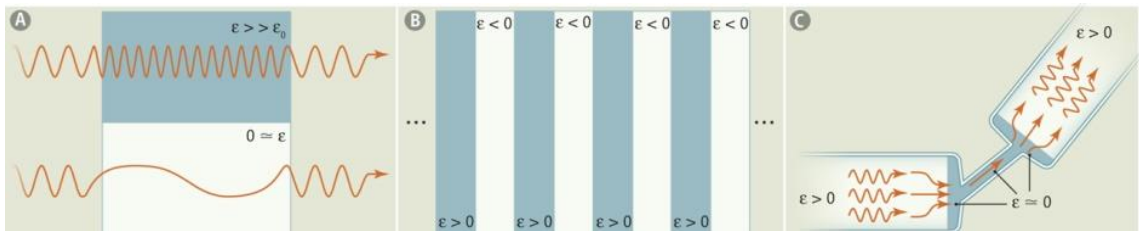


Figure 2.10 (a) The wavelength can be “stretched” within materials with low permittivity, whereas for high permittivity it is compressed. (b) A judicious mixture of a permittivity-positive and a permittivity-negative constituent structure may provide an effectively ENZ metamaterial. (c) The supercoupling phenomenon in ENZ-filled ultranarrow channels between two similar, but arbitrarily oriented, waveguides, in which an efficient tunneling occurs regardless of the length, shape, bending, and twisting of the ultranarrow channel. Reprinted with permission from Engheta⁶² Copyright 2013 American Association for the Advancement of Science.

2.5.1 ENZ materials

Metamaterials with anomalous optical properties are hardly observable although they may exist in nature. All materials have a dispersive optical response depending on the frequencies. When the operating frequency is near the plasma frequency of materials (ω_p), materials may experience an abrupt change in optical properties because the sign of permittivity can alter at this boundary.⁶³ For transparent conducting oxides [e.g., indium-tin-oxide (ITO)], the real part of the permittivity is larger than one at a high frequency (visible regime) and tends to decrease as the frequency goes down. In near-infrared, it turns into negative permittivity as displayed in Figure 2.11.⁶³ Therefore, at given frequency near the plasma frequency (ω_p) of ITO, ITO has the ENZ effect. Interestingly, electron density in a semiconductor such as ITO can be tuned via field effect, which in turn, enables the frequency at which the ENZ effect occurs to be modulated. This mechanism is very useful in manipulating light at the telecommunication wavelength of $1.55\mu\text{m}$.⁶⁴ Thus, many researchers have investigated electro-optical modulation of a silicon waveguide via the ENZ phenomenon.⁶⁴⁻⁶⁶

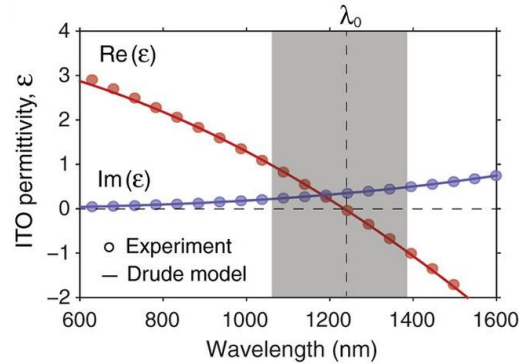


Figure 2.11 Linear relative permittivity of the ITO film measured via spectroscopic ellipsometry (symbols) and estimated by the Drude model (lines). The condition $\text{Re}(\epsilon) = 0$ occurs at $\lambda = 1240$ nm. Reprinted with permission from Alam *et al.*⁶⁷ Copyright 2016 American Association for the Advancement of Science.

Alternatively, metamaterials can be designed to achieve effective permittivity near zero by mixing constituent materials with positive permittivity (oxide) and negative permittivity (metal) structures as shown in Figure 2.10b.^{68, 69} Metamaterial designs composed of alternating layers of Ag and SiN with subwavelength layer thickness enable effective permittivity to be modulated via geometrically averaged permittivity, like $\epsilon_{\text{avg}} = \rho\epsilon_m + (1 - \rho)\epsilon_d$, where ρ is the metal filling fraction. As shown in Figure 2.12, Ag metal has negative permittivity in the visible regime while the SiN

dielectric has positive permittivity at all visible frequencies. Therefore, by controlling the filling fraction of the metal film, the average effective permittivity of this metamaterial can be tunable, leading to ENZ materials in the visible frequencies.⁶⁸ This ENZ metamaterial composed of alternating metallic and dielectric layers demonstrated unique optical properties such as strong light transmission with no phase variation.

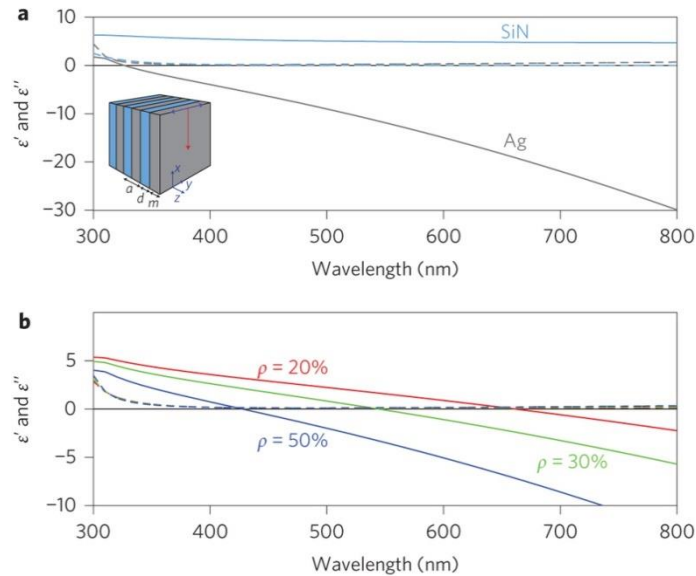


Figure 2.12 Permittivity of a metal-dielectric multilayered ENZ material. (a) Measured real (ϵ' , solid line) and imaginary (ϵ'' , dashed line) permittivity of Ag (grey) and Si₃N₄ (blue). Inset: schematic of the multilayered metamaterial structure composed of Ag and SiN layers (a , d , and m are unit cell dimension and dielectric and metal layer thicknesses, respectively). Light is incident along the x -direction and polarized along the y -direction. The dashed lines for Ag and SiN coincide. (b) Effective permittivity of an Ag/SiN multilayered metamaterial with metal filling fraction $\rho=20\%$ (red), 30% (green) and 50% (blue), calculated using an effective medium approximation. The real (ϵ' , solid line) and imaginary (ϵ'' , dashed lines) parts of the permittivity are shown. The dashed lines for the three filling fractions coincide. Reprinted with permission from Maas *et al.*⁶⁸ Copyright 2013 Macmillan Publishers.

Another way to imitate propagation in an ENZ medium is to exploit the structural dispersion of metal-clad waveguides near their cut-off frequencies.⁷⁰ When operated near its cut-off frequency, such a waveguide can support a non-propagating mode with wavevector k approaching zero, resulting in a large phase velocity inside the waveguide, which is in many ways analogous to ENZ materials without any effort to employ complicated structures for realizing the ENZ material.

Studying modal dispersion of waveguides gives us the insight to understand optical behaviors at cut-off frequencies. Figure 2.13 shows the dispersion of a guided wavevector in a rectangular plasmonic channel. The cut-off mode is not seen in a planar MIM waveguide, whereas a rectangular-shaped waveguide shows that the propagation constant (β) drops off abruptly near the cut-off frequency (350 THz) and no longer allows the propagation of light whose frequency is over the cut-off frequency. k approaching zero at the cut-off frequency leads to a huge wavelength with very fast phase velocity inside the waveguide.⁷⁰ At this cut-off frequency, the waveguide behaves as if it is filled with an ENZ medium, showing no phase delay between entrance and exit sides and high transmission owing to low reflection in spite of the large geometrical mismatch. The advantage of this approach to realizing ENZ materials is the tunability of the frequency at which ENZ conditions can operate by engineering the size and shape of the waveguide or aperture.

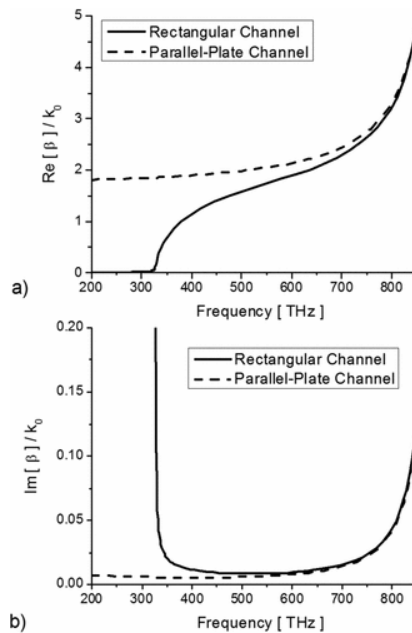


Figure 2.13 Dispersion of the guided wave number (real and imaginary parts) in a rectangular plasmonic channel with $a_{\text{ch}}=20\text{nm}$ and $b=200\text{nm}$ (black), compared with the dispersion in a parallel-plate, metal-insulator-metal waveguide with $a_{\text{ch}}=20\text{nm}$ (red). Reprinted with permission from Alu *et al.*⁷⁰, Copyright 2008 American Physical Society.

2.5.2 Supercoupling effect

When two waveguides are connected by an ENZ-filled tunnel, an exceptional optical property called supercoupling⁷⁰ occurs regardless of the connecting channel's length, shape, or bending as illustrated in Figure 2.10c. In an ENZ-filled channel, the wavelength of light becomes infinitely long due to the near-zero permittivity. The resulting reduced group velocity allows for the trapping of light in the narrow channel. Therefore, more optical energy can pile up inside the narrow waveguide, leading to enhanced tunneling. In addition, the enhanced intensity is uniform along the waveguide without phase delay because of infinitely long wavelength of light. Such enhanced optical transmission via the ENZ condition seems to be similar to the coaxial aperture discussed in 2.4.2. They may be different approaches to or interpretations of the same phenomenon. In Chapter X of this thesis, this guided ENZ mode at the cut-off frequency will be demonstrated, experimentally and numerically showing the unusual tunneling effects mentioned above.

Chapter 3

Extraordinary optical transmission through ultra-small coaxial apertures

As described in chapter 2.5, epsilon-near-zero (ENZ) metamaterials can enable novel physical investigations (*e.g.*, supercoupling and squeezing of mid-infrared light, slow light phenomena) and practical applications such as nonlinear optics, optical trapping, and graphene plasmonics. Among three types of ENZ metamaterials mentioned above, ITO-based ENZ materials and multi-layered ENZ materials consisting of alternating Ag and SiN thin layer have been demonstrated experimentally. However, the last structure such as extremely narrow metallic waveguide with the cutoff frequency has been very challenging to manufacture with reproducibility and high throughput. In this chapter, a practical platform to realize wafer-scale ENZ metamaterials is demonstrated by combination of atomic layer lithography and glancing-angle ion polishing to create wafer-scale metamaterials composed of dense arrays of ultrasmall coaxial nanocavities in gold films.⁷¹ Using this platform, we explored extraordinary optical transmission in MIR via supercoupling at ENZ condition, both numerically and experimentally. The results of fabrication method and optical measurement of coaxial nanogap aperture introduced in this chapter are mainly derived from the following publication:

Daehan Yoo, Ngoc-Cuong Nguyen, Luis Martin-Moreno, Daniel A. Mohr, Sol Carretero-Palacios, Jonah Shaver, Jaime Peraire, Thomas W. Ebbesen, Sang-Hyun Oh, “High-throughput fabrication of resonant metamaterials with ultra-small coaxial apertures via atomic layer lithography”, *Nano Lett.*, 2016, 16, pp 2040–2046

3.1 EOT via ENZ at the cutoff frequency

Engineered metallic apertures and resonant cavities that confine light into nanometric volumes are powerful tools for plasmonics, biochemical sensing, imaging, optical trapping, nonlinear optics, and nanophotonics.^{1, 3, 72-74} Coaxial nanoapertures^{54, 57, 75-78} have been of particular interest in this area due in part to their unique properties arising from the 0th-order Fabry-Pérot (FP0) mode, which occurs spectrally close to the cutoff frequency of the TE₁₁ waveguide mode. At this cutoff

resonance, the propagation constant approaches zero, resulting in a model ENZ material.^{68, 70} As the phase velocity diverges and the group velocity is greatly diminished, extreme, uniform field enhancement is enabled by a “slow-light” effect caused by the trapping of light inside the aperture as well as other intriguing effects such as supercoupling and squeezing of light into ultra-narrow waveguides, and transmission that is nearly independent of the channel length.⁷⁹ Since a normally incident plane wave is efficiently coupled to this resonant mode, EOT¹ can readily be observed. In this coaxial metal-insulator-metal (MIM) geometry, the cutoff wavelength is governed by the gap size and diameter of the annular aperture.⁷⁸ The highly tunable cutoff resonance available in this geometry can couple and store a significant amount of optical energy into ultra-compact ring-shaped nanocavities. These structures exhibit higher order resonances at frequencies as high as the optical and FP0 resonances in the near-infrared (NIR). Using a dense array of these nanocavities, EOT mediated by cutoff resonances can be measured through sub-10-nm gaps, revealing ENZ-like properties – efficient coupling and channel-length-independent resonance – arising from the FP0 mode. These properties can be harnessed for nonlinear optics,^{80, 81} metamaterials,^{82, 83} light trapping,^{84, 85} coaxial nanolasers,⁸⁶ particle trapping,⁸⁷ and spontaneous emission enhancement.⁸⁸

3.2 High-throughput fabrication of coaxial nanogap aperture array

In spite of many advantages discussed above, the reproducible, high-throughput fabrication of compact coaxial structures – in particular with single-digit-nanometer gaps – has been very challenging. Typically coaxial-shaped apertures have been fabricated using focused-ion beam (FIB) milling over a small area, but the gap width is not constant throughout the film due to redeposition of metals, and it is difficult to achieve resolution below 50 nm using gallium-based FIB^{77, 89}. Optical interference lithography has been used to produce coaxial apertures over a large area, but the gap size was larger than 60 nm.^{90, 91} Recent work employing helium-FIB lithography created isolated 8-nm-wide single coaxial apertures and studied resonances only in the visible regime, but cut-off resonance mode was not observed.⁸⁹ In this chapter, a new approach to make a large array of ultra-small coaxial apertures will be demonstrated. Experiments combine atomic layer lithography, which turns atomic layer deposition (ALD)^{25, 92} into an Angstrom-resolution gap-forming method,³² with a wafer-scale glancing-angle ion polishing technique. The combination of these two powerful methods can create ultrasmall coaxial nanocavities at extreme densities over an entire wafer, opening up the door to devices with sub-10-nm gaps and FP0 resonances in the NIR and potentially even in the visible.

Before introducing a new fabrication scheme employed for this work, I will briefly summarize how ALD-based nanogap fabrication schemes have evolved, as illustrated in Figure 3.1. The idea of using ALD for lithographic patterning was first demonstrated by H. Im et al. to make vertically oriented nanogaps with 5 nm gap patterning resolution (Figure 3.1a). However, resulting nanogap structures had an opening area at the center of the nanogap loop, which made it difficult to observe the resonance arising from the nanogap loop due to strong background signal, even though the vertically-oriented nanogap loops achieved the strong enhancement of Raman signal through the nanogap loops. To remove such hollow structures and study optical transmission and resonant effects, tape-peeling-based planarization technique was developed by Chen et al., as shown in Figure 3.1b. In this approach, the metal layer on top of alumina ALD layer was removed using Scotch Tape simply owing to poor adhesion between gold and alumina, thereby leaving alumina nanogap loop only to be inserted to metal without any hollow structures. This technique^{32, 33} addressed the challenge of mass-producing long and uniform annular gaps down to 1 nm in width, but was limited by photolithography and our tape-peeling method in resonator diameter and array periodicity, leading to THz regime FP0-mediated enhanced transmission. In order to maintain the 1-2 nm gap sizes required for extreme field enhancements and enable operation at visible and infrared (IR) frequencies, the diameter of the coaxial resonator must be reduced by ~100 fold. Thus, a new approach should be introduced to overcome this miniaturization challenge for atomic layer lithography and construct ultra-compact, high-aspect-ratio coaxial nanocavities with gaps as small as 2 nm and diameters as small as 100 nm, as shown in Figure 3.1c.

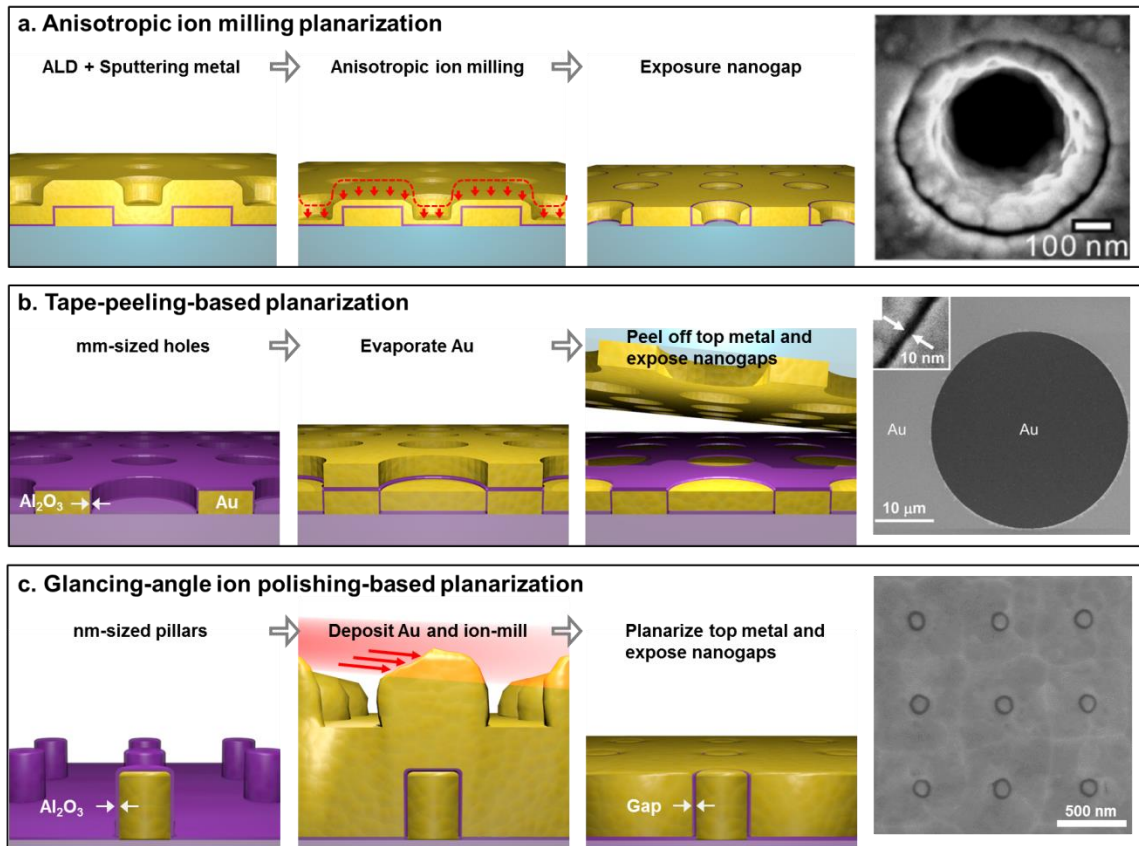


Figure 3.1 Variations of atomic layer lithography technique. (a) Process flow of making vertically oriented nanogap structure by anisotropic ion milling. Minimum gap size of 5 nm was demonstrated, but the resulting hollow structures prevented optical transmission measurements. (b) To solve this problem, Chen et al. used adhesive tape-based planarization to form nanogaps in otherwise opaque metal films. (c) Schematic flow of our new fabrication process used for the coaxial nanocavity array using glancing-angle ion polishing. Figure is adapted from Yoo *et al.*⁷¹

As shown in Figure 3.1, atomic layer lithography, which we define as a fabrication scheme to control critical gap dimensions using ALD, can be implemented via different approaches to planarize and expose vertical nanogap structures. Previous work³³ demonstrated the unique possibility of fabricating arrays containing very long nanogap loops (perimeter of up to ~ 1 cm) as illustrated in Figure 3.1b. To push FP0 resonances to NIR and visible, the diameter of each coaxial gap should be in the deep-sub-micron regime. The critical challenge in making high-aspect-ratio coaxial nano-waveguides via tape-peeling-based nanogap fabrication is filling the sub-micron core region with metals. To solve this problem, the process sequence is inverted by first forming high-

aspect-ratio metal pillars, i.e. the core region, followed by ALD coating to define the gap size and then a conformal metal cladding deposition. After this step, the entrance of coaxial nanocavities is exposed by glancing-angle ion polishing to shave off residual metals on the surface (Figure 3.1c). Tape-peeling-based planarization is suitable for manufacturing large nanogap loops (from tens of micrometers to a few centimeters in perimeter), whereas glancing-angle ion polishing is optimized for the fabrication of large-area sub-micron coaxial nano-aperture arrays.

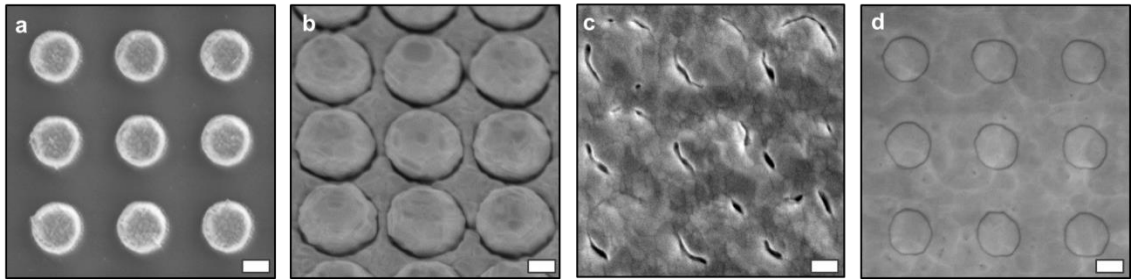


Figure 3.2 Series of SEM images corresponding to process steps. (a) First, the Au pillar arrays are patterned on a sapphire wafer using e-beam lithography, metal evaporation, and lift-off. An ALD Al_2O_3 film is then conformally coated on the patterned Au pillar array. The array periodicity is 500 nm, and the pillar diameter is 250 nm. (b) Second Au film is conformally deposited atop of the Au pillar array. (c) Decorated second Au film is then selectively etched away through glancing-angle ion polishing. (d) Patterned Au surface is planarized by glancing-angle ion polishing, which exposes vertically oriented Al_2O_3 gaps. Scale bars: (a), (b), (c), (d) 150 nm. Figure is adapted from Yoo *et al.*⁷¹

Our new fabrication method is illustrated in Figure 3.1c with corresponding scanning electron micrographs (SEMs in Figures 3.2a-d). In this exemplary structure, first, a square array of 200 nm-tall gold pillars (diameter: 250 nm; period: 500 nm; array size: 200 μm by 200 μm) is patterned on a sapphire substrate using electron-beam lithography. For large-area fabrication after optimal parameters are chosen, nanoimprint or photolithography can be used. Next, the critical dimension (gap width) is defined via an ALD-grown alumina (Al_2O_3) film, which conformally covers the exposed gold surfaces (Figure 3.2a). A second layer of gold (400 nm) is then deposited to form the metal-insulator-metal (MIM) structures (Figure 3.2b). Finally, the top surface is planarized via glancing-angle ion milling (10° from surface) to expose the Al_2O_3 -filled coaxial apertures. During this process, the bumps in the second gold layer are shaved off by Ar ion bombardment whereas flat regions are shadowed and protected (Figure 3.2c). As the planarization

process continues, this shadowing effect gradually dissipates, and the entire film is polished uniformly. A top view SEM (Figure 3.2d) shows an array of coaxial apertures with a 250-nm diameter and 10-nm Al_2O_3 gap formed through the entire thickness of a 150-nm gold film. The sample before the planarization by glancing-angle ion milling shows the height difference of 200 nm (Figure 3.3), which corresponds to the core metal thickness. After ion milling, the height difference was reduced to below 20 nm, as confirmed by atomic force microscopy (AFM) (Figure 3.3). In this process, the flatness after polishing is controlled by the incidence angle of the ion beam. Using an ion beam with a glancing angle lower than 10° can further reduce the height difference. Since ductile metals such as gold are not amenable to standard polishing methods, this new technique could also find applications in eliminating topographic variations in other metallic nanostructures.

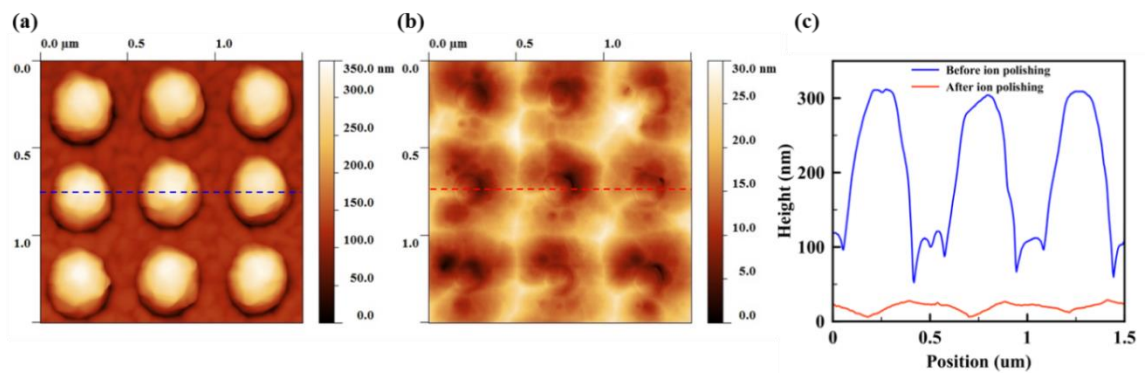


Figure 3.3 Atomic force microscope (AFM) characterization. (a) AFM 2-D image from a coaxial aperture array with 7 nm gap width, 150 nm diameter, and 500 nm period before glancing-angle ion milling. (b) The same sample after glancing-angle ion milling. (c) The comparison of 1-D height profiles over a dashed line in AFM images before and after glancing-angle ion milling. All AFM images were obtained with a Veeco Nanoscope V multimode system. The samples were scanned using tapping mode, typically over a $2 \times 2 \mu\text{m}$ area at a scan rate of 1 Hz. Nanoscope software was utilized to analyze the images and extract topographical information. Figure is adapted from Yoo *et al.*⁷¹

3.3 Optical measurement setup

3.3.1 Visible and NIR spectroscopic measurements

For transmission measurements in the visible and NIR wavelengths, coaxial apertures were illuminated with a broadband fiber-coupled, laser driven light source (Energetiq, EQ-99FC) through a condenser on an inverted microscope (Nikon, Ti-S), and the transmitted light was collected with an objective and imaged onto the entrance slit of a 300 mm focal length imaging spectrometer (Acton SP2300i) equipped with a CCD camera (Princeton, Pixis 400) for the visible and a thermoelectrically cooled, 256-element InGaAs diode array (BaySpec Nunavut) for the NIR. Spectra were background subtracted and normalized using the spectrum for direct transmission through the sapphire substrate.

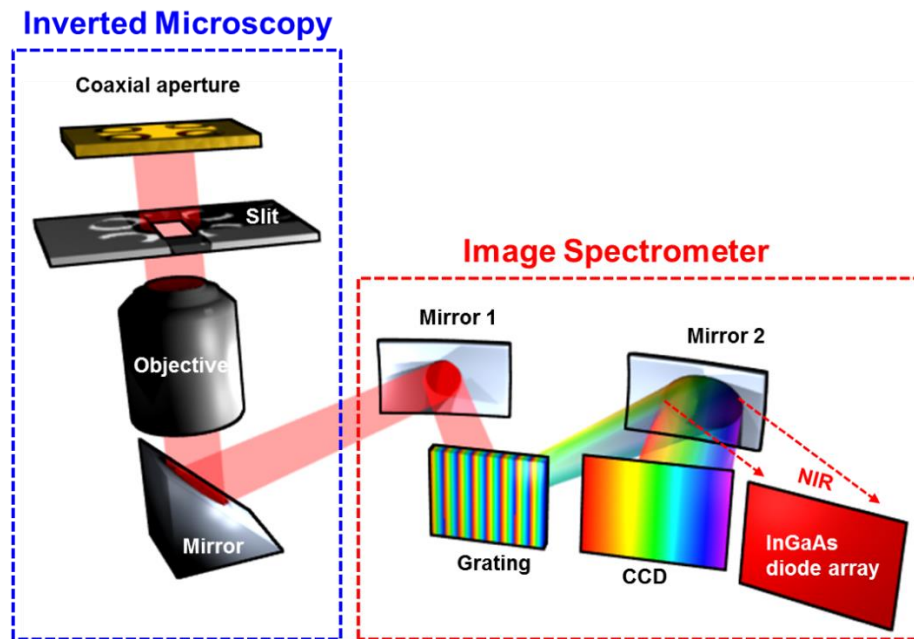


Figure 3.4 Schematic of optical measurement setup for visible and near-IR.

3.3.2 FTIR instrument and measurement for mid-IR

The transmission spectra of coaxial apertures were measured in the MIR using Fourier transform infrared spectroscopy (Thermo Scientific, Nicolet Magna IR 750) with a transmission mode microscope. All of the data from coaxial aperture arrays were taken using the microscope with an unpolarized IR light source, a liquid-N₂-cooled MCT-A (Mercury ZincTelluride Alloy) detector, and an aperture size of 100 μm by 100 μm . The signals that were averaged for 256 times with a resolution of 4 cm^{-1} were normalized to the background signal taken from a bare sapphire wafer. The sapphire wafer was transparent up to 6.5 μm with measured transmittance of 80%.

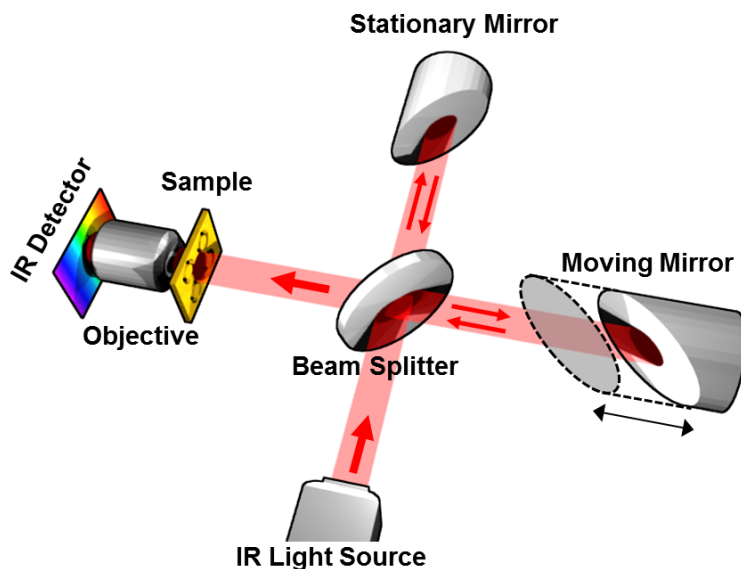


Figure 3.5 Schematic of optical measurement setup for mid-IR.

3.4 Transmission spectra measured from visible to IR

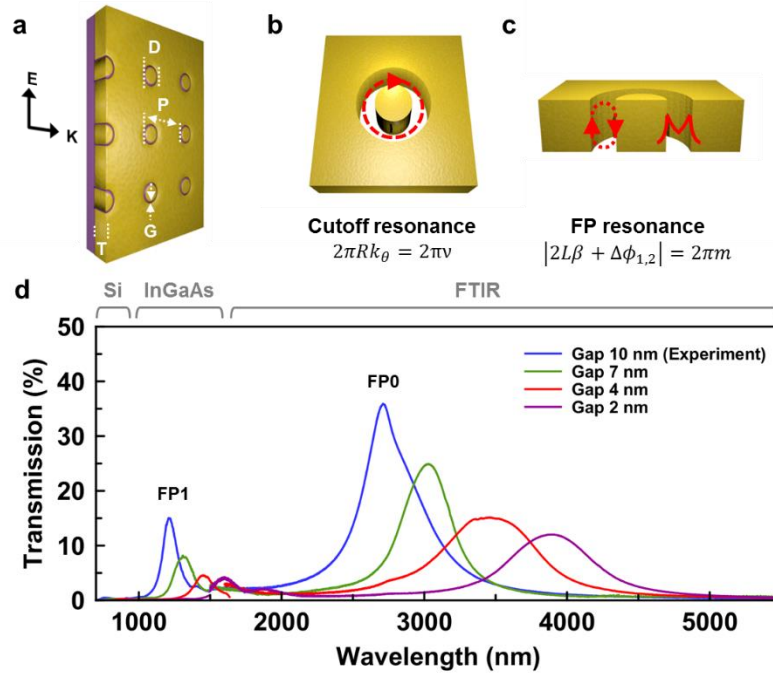


Figure 3.6 Measured extraordinary transmission through the coaxial aperture array. (a) Schematic of a coaxial aperture array. Illumination is through a sapphire substrate with unpolarized light, and transmission spectrum is measured using three different spectroscopic systems covering over 3 full octaves from 400 nm to 5000 nm in wavelength. (b-c) Schematics of coaxial waveguides with the cutoff resonance and the FP resonance. (d) Measured spectra of light transmitted from the coaxial aperture array with a 250 nm diameter and four different gap widths (2, 4, 7, 10 nm). Figure is adapted from Yoo *et al.*⁷¹

The geometry of the coaxial nanocavity array is determined by the metal film thickness (T), inner diameter of the annular gap (D), gap width (G), and array periodicity (P), as illustrated in Figure 3.6a. The cutoff wavelength of a coaxial aperture made with a perfect electrical conductor is given by $c = n(R_o + R_i)$, where n is the refractive index of the insulator and R_o and R_i are the radius of the outer and inner surfaces of the gap, respectively.⁵⁷ For coaxial apertures made with a real metal, however, the cutoff wavelength can differ dramatically from this PEC approximation, especially as the gap size is reduced.⁵⁷ To prove our coaxial waveguides exhibit singular optical behavior, we experimentally measured the optical transmission spectra through coaxial aperture arrays with a 250 nm inner diameter and four different gap widths (2, 4, 7, 10 nm). Spectra were collected using

a Si CCD, InGaAs photodiode array, and FTIR spectrometer, respectively in the visible, NIR, and mid-infrared (MIR) regions (Figure 3.6d). Multiple peaks for a given gap size are observed throughout the entire spectrum. The most notable feature of the measured spectra is the presence of intense MIR EOT peaks. For a 10 nm gap size and inner diameter of 250 nm, the strongest resonance peak occurs at the free-space wavelength of 2800 nm with an aperture-normalized transmission of 1170%. Table 3.1 shows the aperture-normalized and absolute transmission from different gap sizes. Interestingly, as the gap size shrinks, the resonance wavelength of the EOT increases dramatically (Figures 3.6d).

When first described, EOT initially referred to transmission greater than unity through periodic metallic apertures in cutoff, i.e. the field inside the aperture is evanescent. In that case, the incoming electromagnetic field couples to surface plasmons of the corrugated surface of a metal film, trapping energy in the system for an extended time leading to increased tunneling through the apertures. This definition has since been expanded to include optical resonances that lead to enhanced transmission in general, irrespective of whether the individual apertures are in cutoff, and a non-exhaustive list now includes cut-off resonances, Brewster-like resonances, and absorption-induced transparency.⁹³ In our coaxial aperture array, the periodicity of 500 nm was chosen to confine surface resonance effects to the NIR (900 nm), thereby ensuring the observed MIR peaks are not due to surface resonances or a periodic effect. Instead, enhanced transmission in our coaxial waveguides is induced by Fabry-Pérot (FP) type resonances that propagate along the length of the aperture. Notably, there is a special 0th-order FP case, which occurs spectrally close to the cutoff frequency of the TE₁₁ waveguide mode, where EOT can arise as well.

The multiple peaks for a given gap size in our devices emerge from these series of FP modes, including the 0th-order cutoff resonance, and span over a full octave in frequency. The lowest-frequency peak we observe in the MIR should correspond to the 0th-order cutoff resonance, and the next resonance peak in the NIR corresponds to a first-order FP mode. In the first-order FP mode, light traveling in the Al₂O₃-filled coaxial MIM waveguide is partially reflected at the upper and lower surfaces of the metal film, forming a resonator whose cavity length (L) is equal to the film thickness, provided that the following condition is satisfied:

$$|2L\beta + \Delta\phi_1 + \Delta\phi_2| = 2\pi m \quad (3.1)$$

Where β is the propagation constant in the MIM coaxial waveguide, $m \geq 0$ is the integer representing the mode number ($m=1$ in this case), and $\Delta\phi_{1,2}$ are the phase shifts due to reflection.⁷⁷ As alluded

to earlier, $m=0$ is a valid solution to the FP condition as well, so long as $X \rightarrow 0$, which explains why the cutoff resonance can be described using FP nomenclature.

Table 1. The EOT calculated from the measured transmission with different gap widths.

Gap width (nm)	Measured transmission (%)	Open area fraction (%)	Area-normalized transmission (%)
10	36	3.06	1,170
7	25	2.28	1,090
4	15	1.35	1,120
2	12	0.69	1,740

3.5 FEM modeling results

The physical origin of the observed peaks is further analyzed by comparing the measured data to computer simulations. Because of the large-scale mismatch in the wavelength (up to 6 μm) and gap size (<10 nm), we chose an advanced finite-element method based on a Hybridizable Discontinuous Galerkin (HDG) scheme, which is optimized to handle such multi-scale problems.³³ The HDG scheme was developed by our collaborator, Jaime Peraire and N.C. Nguyen, and they performed simulations for this publication, which I summarize in this section. In this work, the HDG method is used to solve the time-harmonic Maxwell's equations on an anisotropic unstructured mesh of 21384 quartic hexagonal elements. The accuracy of these results is verified by performing a grid convergence study in which we carry out the simulations on three consecutively refined meshes and observe that the difference in the maximum EOT between the medium mesh and the fine mesh is less than 0.25% for all cases. The calculated EOT spectra (Figure 3.7a) agree well with the measured spectra for a 10-nm-gap coaxial aperture array. For gap sizes below 4 nm, the mismatch increases likely due to fabrication imperfection such as roughness of the interior metal surfaces. In the size regime presented, even sub-nm changes in the gap width can have large effects on the position of resonant peaks. Additionally, the realistic bulk dielectric constant values for an ALD-grown Al_2O_3 thin film used in simulation can diverge from experimental values for narrower gaps (below 4 nm). The calculated electric field maps for two observed peaks are plotted in Figure 3.7d. For illumination at normal incidence using linearly polarized light, the fundamental TEM mode of a coaxial waveguide cannot be excited due to the mismatch in mode symmetry, but higher-order modes with non-zero angular momentum can. The field profiles of the cross-section atop the coaxial aperture show that the transmission resonances arise from TE_{11} modes (the lowest order mode with non-zero angular momentum). At the ENZ condition, the phase velocity is so large that the phase shift between the entrance and exit sides of the coaxial waveguide becomes very small, leading to uniform electric fields inside the nanogap as shown in the vertically cross-cut field map corresponding to the MIR resonance. The simulation results also indicate that this is indeed a cut-off resonance (FP0 mode). The resulting slow light effect can enable extremely strong field intensity enhancements (over 6,000 observed in simulation) inside the ultrasmall coaxial nanocavities as the gap size narrows to only 2 nm (Figure 3.7c).

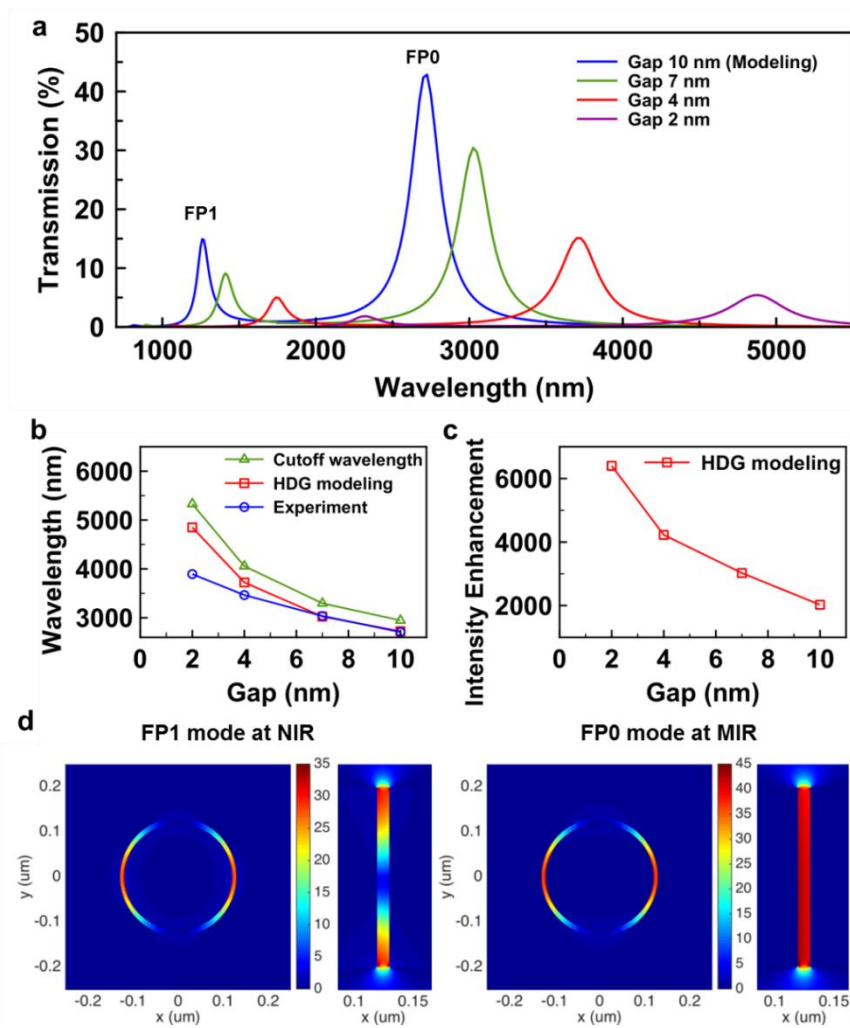


Figure 3.7 Simulated extraordinary transmission through the coaxial aperture array. (a) Simulated spectra of light transmitted from the coaxial aperture array with a 250 nm diameter and four different gap widths (2, 4, 7, 10 nm). (b) Variation of transmission peak wavelength of the FP0 ($m=0$) resonance as a function of gap width in the coaxial aperture array. (c) Intensity enhancement for the FP0 resonance as a function of gap width. (d) Calculated electric field distributions of 250 nm diameter coaxial aperture with a 10 nm gap at the resonance wavelengths of 1200 and 2700 nm. Figure is adapted from Yoo *et al.*⁷¹

3.6 ENZ property of coaxial nanogap aperture

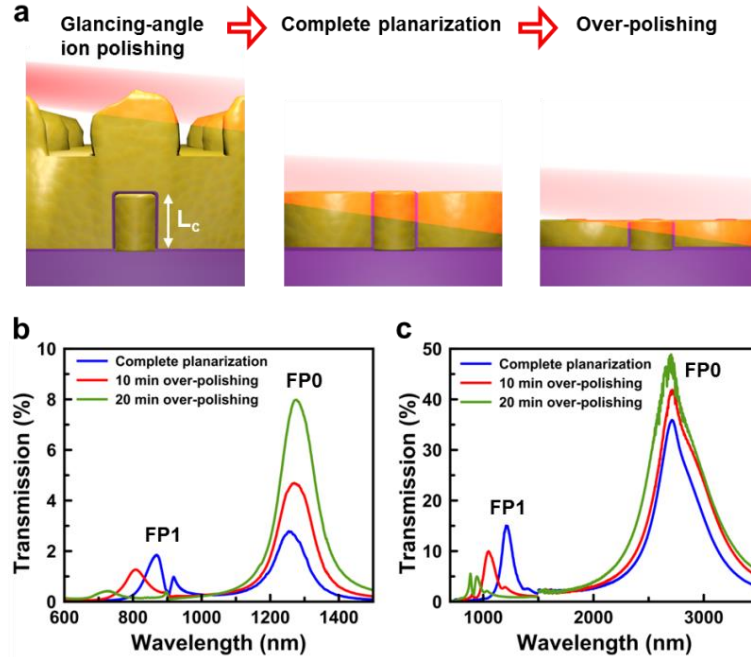


Figure 3.8 Experimental verification of the FP0 cut-off resonance mode by the ENZ properties of the resonant peaks. (a) Schematic of glancing-angle ion polishing to reduce the cavity length. (b) and (c) The change in the transmitted spectra as glancing-angle ion polishing time increases and film thickness decreases from a coaxial aperture array with a 10 nm gap width and diameters of 100 nm and 250 nm, respectively. Figure is adapted from Yoo *et al.*⁷¹

I studied the dispersion properties of these peaks experimentally by shortening the FP cavity length. This was accomplished by continuing the glancing-angle ion polishing past planarization (Figure 3.8a). As the cavity length is reduced, the resonance wavelength of the FP0 mode, which is determined by the cutoff frequency and has a propagation constant of practically zero, does not change appreciably while the FP1 peak blue-shifts (Figures 3.8b-c). We note that there is a small reflection phase which, at resonance, has to be cancelled with an “optical path” phase, slightly shifting the resonance away from the cutoff frequency. This is important for very thin metal films,⁹⁴ but not for the thicknesses considered in this work. The film-thickness-independent property of the FP0 mode also explains the nature of previously observed THz resonances alongside millimeter-scale loops in earlier work,³² which was not explicitly mentioned. In that case, the film thickness

was only 150 nm whereas the resonance wavelength was in the millimeter-scale, thus FP1 or higher-order modes could not be sustained in the thin film, while FP0 resonances were still present. This property of the FP0 “slow light” mode, which is independent of the length of the waveguide, exhibits ENZ behavior. In addition, the resonator periodicity can be much smaller than the resonance wavelength as demonstrated, and thus our coaxial resonator array can be a practical platform to construct large-area ENZ metamaterials.

3.7 Dispersion of coaxial nanogap aperture

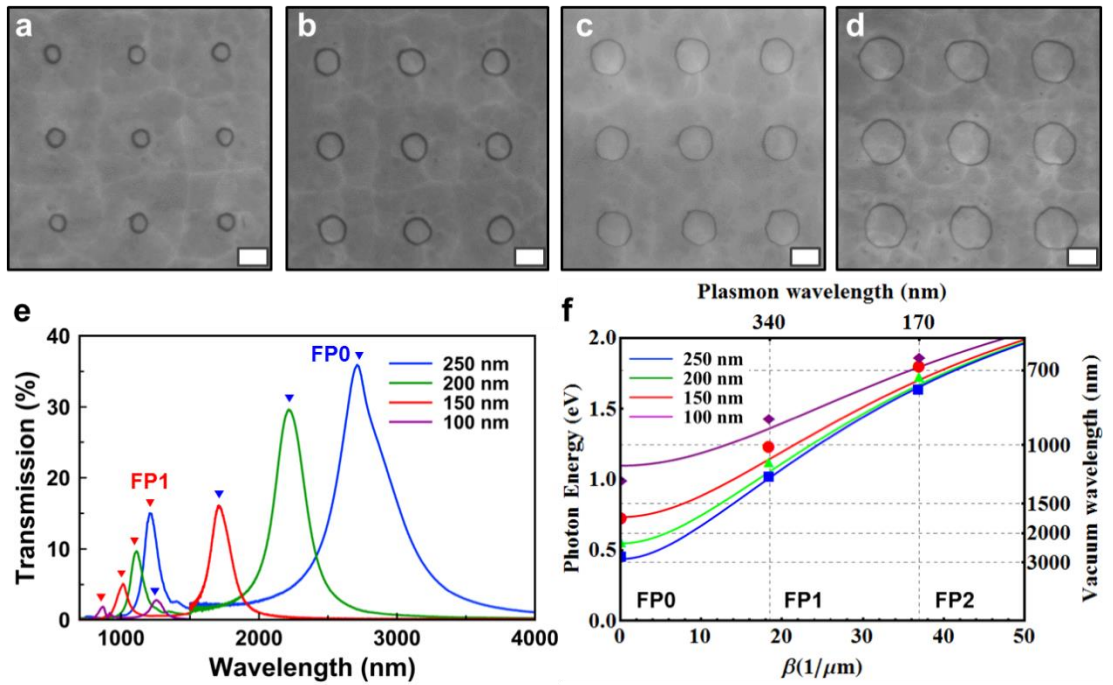


Figure 3.9 The effect of diameter on the transmission resonances excited in a coaxial aperture array. (a-d) SEM images of coaxial aperture arrays with 100, 150, 200, 250 nm diameters, respectively. (e) The transmitted spectra from the coaxial 10-nm gap with 100, 150, 200, 250 nm diameters. (f) The dispersion curve of the plasmonic coaxial aperture. FP0 ($m=0$), FP1 ($m=1$), FP2 ($m=2$) resonances (experimental data) are fitted with the analytical dispersion curve. Figure is adapted from Yoo *et al.*⁷¹

The TE_{11} resonances of our devices can be tuned by changing the aperture diameter. The propagation constant β , transverse wavevector k_{θ} of a coaxial aperture waveguide, and the propagation constant β_{MIM} of a planar MIM waveguide, should satisfy the following condition⁷⁶:

$$\beta^2 + k_\theta^2 = \beta_{\text{MIM}}^2 \quad (3.2)$$

$$2\pi R \cdot k_\theta = 2\pi\nu \quad (3.3)$$

where ν is an integer and R is the average radius. The cutoff frequency is thus influenced by the diameter of the coaxial aperture. To investigate this effect, coaxial apertures with a 10 nm gap were fabricated with ring diameters of 100, 150, 200, and 250 nm (Figures 3.9a-d). As shown in Figure 3.9e, the FP0 resonance peak blue-shifts with a decreasing diameter, as expected. These properties of FP resonances as a function of the aperture diameter can be explained by the theoretical dispersion calculated from eq. (3).⁷⁶ The dispersions of coaxial MIM structure are plotted using eqs. (2) and (3) and compared with experimental data in Figure 3.9f. A unique feature of coaxial apertures is that this cutoff wavelength decreases along with the aperture diameter while maintaining the gap size and hence the field confinement. Thus a simple coaxial aperture geometry can be used to create extreme-subwavelength resonators covering visible, IR, and THz frequencies. These effects are characteristic of an individual coaxial waveguide, rather than a periodic effect, as the change in the periodicity does not shift FP0 frequencies (Figure 3.10). Furthermore, the cutoff resonance frequencies for these FP0 modes do not change with the incident angle of illumination, as confirmed by theoretical modeling (Figure 3.11), making these structures ideal for applications where angle independence is important.^{56, 95}

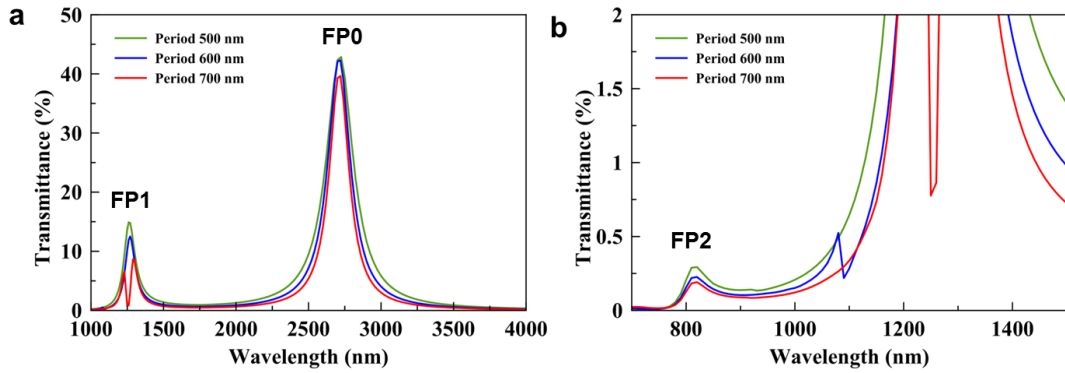


Figure 3.10 The effect of period on the transmission resonances excited from coaxial aperture arrays: (a), (b) 3D HDG FEM simulation of light transmitted from a coaxial aperture with a 10-nm-wide gap, 250 nm diameter and 500, 600, 700 nm periods. Zeroth-order mode (FP0), FP1, and FP2 show no dependence on the array period. As the period increases, Wood's anomaly redshifts and leads to a Fano resonance when it overlaps with the FP1 mode. Figure is adapted from Yoo *et al.*⁷¹

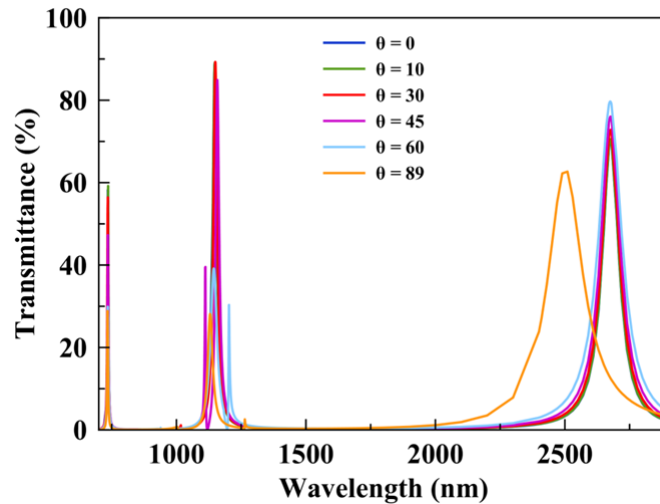


Figure 3.11 The angular dependence on the transmission resonances excited from the coaxial aperture array. CMM modeling of light transmitted from the coaxial 10-nm-wide gap with 250 nm diameter by different incident angles of light. Zeroth-order mode (FP0), FP1, and FP2 show no dependence on the incident angles. This modeling was fulfilled by Carretero-Palacios. Figure is adapted from Yoo *et al.*⁷¹

3.8 Conclusion

In summary, we have combined atomic layer lithography and wafer-scale glancing-angle ion polishing to manufacture ENZ metamaterials consisting of single-digit-nanometer-gap coaxial resonators and investigated their characteristic EOT and slow-light properties. These results demonstrate a 100-fold improvement in device characteristics over our previous work by decreasing the individual resonator footprint from tens of μm to ~ 100 nm, enabling the exploration of EOT as well as ENZ properties in the infrared regimes. Unlike multi-layer film stacks for ENZ, our coaxial aperture array can be made at wafer scale, and readily couple normally incident light independent of polarization, making this a practical ENZ platform utilizing EOT. Our choice of 500 nm array periodicity confines periodic coupling effects to the NIR regime while sub-10-nm gap widths push the FP1 and FP0 resonances of an individual coaxial aperture toward the MIR, allowing unambiguous observations of these properties and proving that the observed resonances arise from the properties of individual apertures. The gap width is as small as $\lambda/1900$ at MIR resonances, and the cutoff resonance wavelength of each resonator ($2\sim 4 \mu\text{m}$) is much larger than its unit cell size (cavity diameter of ~ 250 nm). Additionally, the volume of the Al_2O_3 -filled gap is as small as $\lambda^3/10^6$ for MIR operation, making these structures one of the smallest nanophotonic resonators to date. Our high-throughput fabrication technique can be applied to a wide range of metals and gap-filling insulators as well as for resonators in the visible regime and with different shapes. The metal pillars and surrounding film can be addressed as electrodes, potentially allowing for the electrical generation of plasmons by tunneling directly in the waveguides.⁹⁶⁻⁹⁹ Furthermore, the intense fields of this extremely confined slow-light mode at ENZ condition can be accessed from the flat top surface and coupled with other materials for applications in biosensing,^{100, 101} surface-enhanced spectroscopies,^{18, 31, 41, 102, 103} optical trapping,^{87, 104} and nonlinear optics.^{80, 105, 106} Our work demonstrates that metamaterials with extreme sub-wavelength features such as single-digit-nanometer gaps can now be manufactured for practical applications.

Chapter 4

Optically active trench nanogap resonators

4.1 High Q factor and Fano resonance

Quality factor (Q factor) is a standard to measure how long a resonator can store energy inside itself, and is defined by $Q = 2\pi f_{\text{resonance}} \times \frac{\text{Energy stored}}{\text{Power loss}}$. It can be described simply as $Q = \frac{\lambda_{\text{resonance}}}{\text{FWHM}}$, where FWHM is the full width at half the maximum. That is, as the loss of the resonator is reduced, the quality factor becomes larger with sharp resonance peaks. Optical microcavities such as micropost cavities,¹⁰⁷⁻¹⁰⁹ microtoroid resonators,¹¹⁰ and photonic crystals¹¹¹ have high Q factors because dielectric components have less losses compared to metals. However, dielectric cavities cannot confine light into small mode volumes below the sub-diffraction limit.¹¹² Therefore, surface plasmons (SPs) have been considered as an alternative. But, utilization of SPs for applications with high Q factors has been restricted by intrinsic losses associated with either dissipation to metal or radiation to air.¹¹³⁻¹¹⁵ To compensate for small modal volume and intrinsic high losses in metallic cavities, various designs have been explored, such as plasmonic wedge waveguides,^{116, 117} nanowires,^{118, 119} metallic whispering galleries.^{120, 121}

In a plasmonic system, high Q factor can be achieved by either reducing intrinsic losses or the abnormal interference of two resonances.¹²² Asymmetric resonance established by Ugo Fano⁵¹ is known to arise from the interference between a discrete state and broad continuum as described in Figure 4.1. This abnormal resonance shape has been observed in many classical optic experiments. Wood's anomaly was also understood by the interference between excited leaky surface waves and incoming radiation.⁵⁰ Many plasmonic structures have demonstrated Fano resonance by inducing the superposition of two different types of resonance modes.^{122, 123} Fano resonance can give rise to sharp resonance by splitting the resonance shape in half, leading to high Q factors in plasmonic devices.

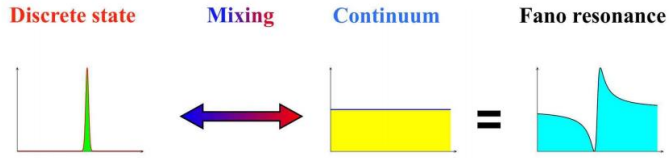


Figure 4.1 Illustration of the Fano resonance formula as a superposition of the Lorentzian lineshape of the discrete level with a flat continuous background. Reprinted with permission from Miroshnichenko *et al.*¹²³ Copyright 2010 American Physical Society.

4.2 Surface plasmon excitation and resonance in a trench resonator

The design of the trench resonator is derived from a similar structure called a cup resonator, which was initially suggested by our collaborator Henri Lezec.¹²⁴ Similar structures (i.e. a sub-wavelength slit inside a metallic microcavity) were also demonstrated by other groups.^{125, 126} The unique contribution of this thesis work is the development of a high-throughput fabrication process by combining atomic layer lithography and sidewall metal deposition, which has enabled fabrication of a trench resonator structure with a sub-10 nm slit. A schematic of the excitation of SPPs in the trench resonator structure is illustrated in Figure 4.2. The trench structure is defined by the trench height (H) and width (w). The nanogap (width: G) is placed at the center of the trench. Normal incident light illuminates the gap from below, through the glass substrate, launching surface plasmon polaritons (SPPs) inside the trench. SPPs propagate toward two metallic sidewalls, bounce back to the nanogap, and interfere with light directly transmitted through the nanogap. Under a constructive interference condition, light is scattered (radiating) into the far field, leading to resonance peaks in optical transmission spectra. On the other hand, transmission dips are observed in the case of destructive interference. In this system, the coherent interference between discrete resonant modes (plasmonic cavity resonances) and broad non-resonant modes (light transmitted from the nanogap) generate asymmetric Fano resonance, as described above.

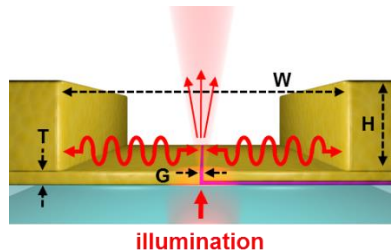


Figure 4.2 A schematic of optical interference in the trench nanogap structure with geometric parameters ($H=1$ μm , $W=3.4$ μm , $G=30\text{-}2000$ nm, $T=150$ nm).

4.3 Optical properties of a trench resonator

4.3.1 Fano resonance of a trench resonator

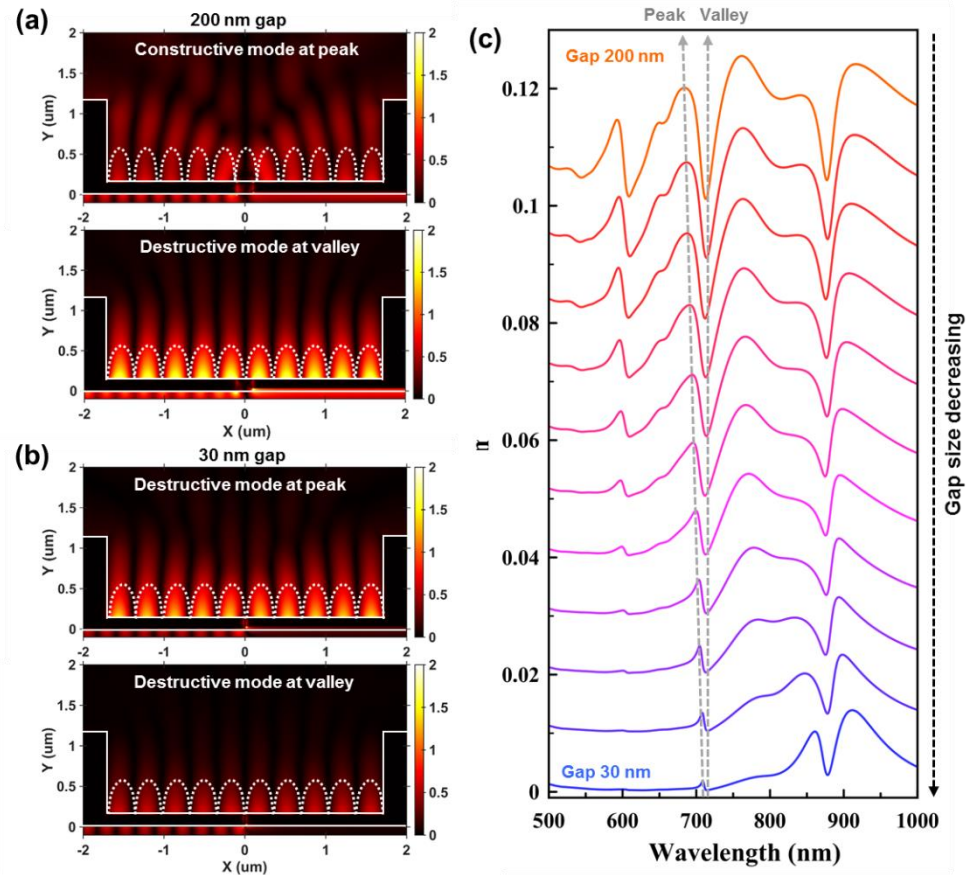


Figure 4.3 Fano resonance with high Q induced by a nanogap. (a-b) Spatial field distributions of E_y at the transmission peak and dip (crossed with gray dash lines) in a trench structure with 200nm and 30nm gap size, respectively. (c) FDTD-simulated transmission spectra from trench resonators with different gap sizes.

Figure 4.3a shows the spatial distributions of the E_y field at $\lambda=684\text{nm}$ (peak) and $\lambda=715\text{nm}$ (dip) in the trench resonator with a 200nm gap. SPPs excited from the gap travel back and forth at the bottom of the trench resonator, building up a standing wave. Subsequently, it interferes constructively with light coming in from the gap at the anti-node of the standing wave, scattering to the far-field, while the destructive interference between two waves at the node results in a transmission dip. The interference in this structure can be interpreted using simple approximation.

Light waves making a single round trip from the nanogap to the sidewall and back to the nanogap experience phase delay with respect to light transmitted directly from the nanogap:

$$\theta = 2 \times \frac{2\pi}{\lambda_{spp}} L + \phi_r \quad (4.1)$$

where θ is the total phase delay, ϕ_r is the phase shift from plasmon reflection, $\lambda_{spp} = \lambda_0 \sqrt{\frac{\epsilon_d + \epsilon_m}{\epsilon_d \epsilon_m}}$ is the wavelength of the SPP, and L is the distance between the nanogap and the sidewall. Assuming the phase shift of π on reflection from the sidewall, the constructive and destructive interferences can be determined as follows. When the total phase delay is an odd integer multiple of π , the destructive interference occurs:

$$L = \frac{\lambda_{spp}}{2} (m - 1) \quad m = 1, 2, 3, \dots \quad (4.2)$$

When the total phase shift is an even integer multiple of π , the constructive interference appears:

$$L = \frac{\lambda_{spp}}{2} \left(m - \frac{1}{2} \right) \quad m = 1, 2, 3, \dots \quad (4.3)$$

Based on this simple analysis, the transmission peak and dip seen in Figure 4.3a arise from constructive and destructive interferences with $m = 6$, respectively. Many other works^{124, 126} have demonstrated similar results with this simple approximation. As the aperture size decreases to tens of nanometers, however, we observe that this approximation is no longer valid for interpreting the interference modes in a trench resonator with a very narrow aperture. Figure 4.3b shows two spatial distributions of the E_y field at the transmission peak ($\lambda=709$ nm) and the transmission dip ($\lambda=715$ nm) in a trench resonator with a 30nm gap aperture. Interestingly, not only the transmission dip, but also the transmission peak arises out of the destructive interference at the node, unlike a trench resonator with a 200nm wide aperture. This singular optical behavior is induced by Fano resonance, in which scattering waves experience sharp phase shifts of π ¹²⁷ Thus, it results in that constructive and destructive interferences take place very close to each other spectrally, which allows constructive interference to be destructive interference. Thus, the transmission peak is governed by destructive conditions due to the phase shift of π occurred during the scattering event. Figure 4.3c

shows a waterfall set of spectra calculated by reducing an aperture size from 200nm to 30nm. At the 200nm aperture size, multiple peaks and dips are created by the interference. As the aperture size narrows to 30nm, transmission peaks start to approach the transmission dips, while the transmission dips do not shift. This can make resonance peaks sharper, thereby leading to Fano resonance with a high Q factor, as shown in Figure 4.3c. Over all, transmission peaks observed with a 200nm gap aperture experienced a phase shift of π from constructive to destructive with decreasing aperture size.

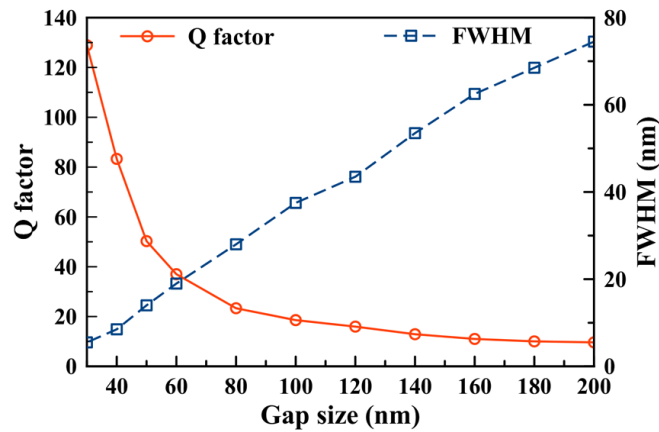


Figure 4.4 Q factor and FWHM calculated from FDTD modeling as a function of gap size.

Given that Q factor is defined by the ratio of stored energy and dissipated energy loss, the Q factor will be improved by reducing the leakage of energy. In a trench resonator, energy is stored as a standing wave form inside the trench. The aperture at the center of the trench then acts as leakage point, dissipating the stored energy and degrading the Q factor. Therefore, by shrinking the gap size, it is possible to reduce the energy dissipation via radiation. Q factor and FWHM as a function of the gap size are plotted in Figure 4.4. FWHM is linearly proportional to the gap size, while Q factor increases exponentially as the gap size decreases. In the end, a trench resonator with a 30nm gap size shows very sharp Fano resonance with a Q factor of 130.

Comparing field maps of 200nm and 30nm gap apertures described in Figure 4.3a and b, the 200nm-sized slit is as large as the wavelength of the SPPs. So, when SPPs and light transmitted from the aperture interfere atop the nanogap, light can scatter to the far-field as well as to the 200nm-wide aperture. On the other hand, a 30nm gap aperture is too small compared to the wavelength of the SPPs to dissipate stored energy. Such a structure can act as a high-Q-factor plasmonic resonator.¹¹²

4.3.2 Dispersion of Fano resonance

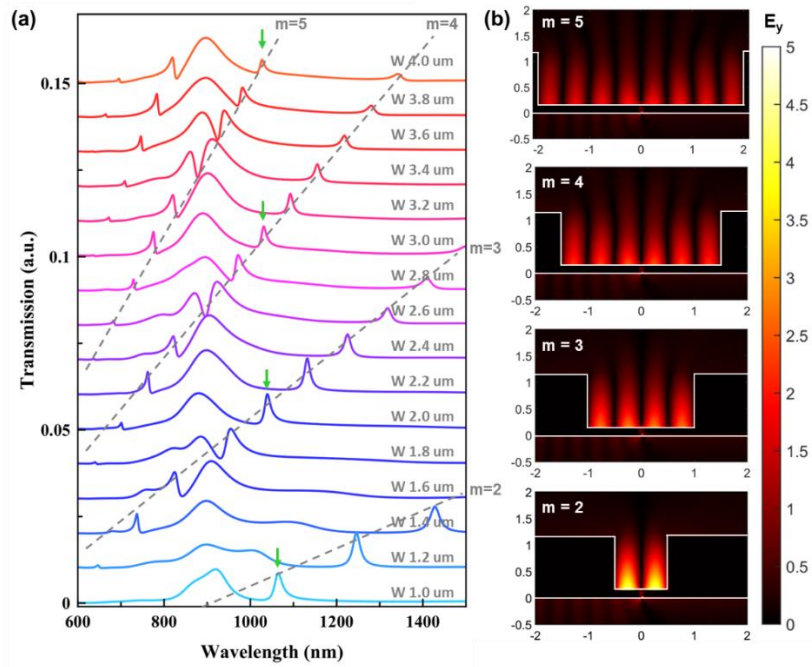


Figure 4.5 Dispersion of destructive mode with trench width. (a) FDTD-simulated transmission spectra through trench resonators with varying trench width (W), (b) spatial distributions of the E_y field in a trench resonator corresponding to destructive modes 2, 3, 4, 5 with $W=1, 2, 3, 4\mu\text{m}$, respectively.

Now, I will investigate how Fano resonance is determined by trench width. As described above, Fano resonance occurs when the destructive condition (equation 4.2) is satisfied. Therefore, resonance red-shifts with increasing trench width ($W=2L$) as shown in Figure 4.5(a). At $W=1\mu\text{m}$, the 2nd resonance mode occurs at the wavelength of 1064nm. Then, it red-shifts as trench width (W) increases. The 3rd resonance mode appearing at the wavelength 643nm for $W=1.2\mu\text{m}$ is approaching the IR regime. As the trench width continues to increase, lower resonance modes ($m=2, 3$) go beyond a window displayed in Figure 4.5a, followed by higher resonance modes ($m=4, 5, 6$). Figure 4.5b shows the spatial distributions of the E_y field around 1064nm for each mode (pointed out with arrows in Figure 4.5a). The 2nd mode shows a single SPP wavelength in the trench resonator, the 3rd mode has two, the 4th mode has three, and the 5th mode has four wavelengths of SPP in the trench resonator.

4.3.3 Asymmetric geometric effect

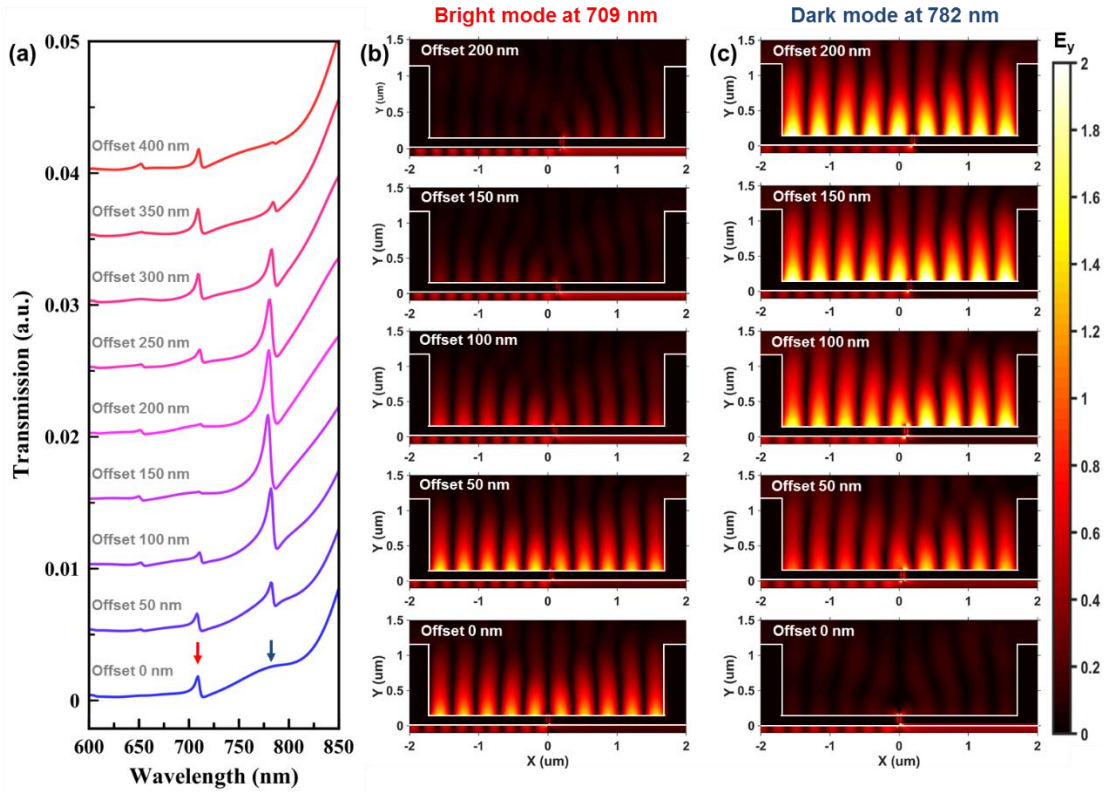


Figure 4.6 Excitation of a dark mode by breaking geometric symmetry. (a) FDTD-simulated transmission spectra from a trench resonator with varying offset at the position of the nanogap from 0nm to 400nm. (b-c) Spatial distributions of the E_y field at the wavelength of 709nm and 782nm, respectively, in the trench resonator with different offsets of 0, 50, 100, 150, and 200nm; (b) shows the extinction of the bright mode at resonance ($m=6$) when breaking geometrical symmetry; (c) depicts the appearance of a dark mode, which is suppressed by Fano interference in the asymmetric trench resonator.

In a geometrically symmetric trench resonator with a 30nm gap, transmission peaks appear with destructive interference due to Fano resonance, as shown in offset 0nm of Figure 4.6a. On the other hand, no transmission peak is observed with constructive interference, even though transmission should arise from the constructive interference. The suppressed constructive mode is called the dark mode. However, a dark mode can be excited by breaking structural symmetry in the trench resonator. Figures 4.6b and c describe how bright and dark modes evolve as the nanogap position shifts inside the trench. For Figure 4.6b, transmission occurs at the wavelength of 709nm where the

destructive condition is satisfied. On the contrary, Figure 4.6c shows that at the wavelength of 782nm, the constructive interference is suppressed, resulting in a dark mode with no transmission. Interestingly, however, this suppressed dark mode can be excited by offsetting the nanogap from the center position and breaking the structural symmetry. Going back to Figure 4.6a, the plasmonic bright mode, with a transmission peak at 709nm, starts to decrease as the nanogap position shifts to the right. It almost disappears at the offset between 150nm and 200nm. Then it increases again up to offset 350nm. The intensity of this resonance peak oscillates with a period of about 350nm, which corresponds well to approximately half of the wavelength of the SPP at 709nm as depicted in Figure 4.6b. In contrast, the depressed dark mode, where there is no transmission peak at 782nm, begins to evolve to a bright mode showing a transmission peak. Its intensity maximizes at the offset of about 200nm and goes back to zero at the offset of 400nm. This dark mode also seems to oscillate with a period of about 400nm. The periods shown in Figure 4.6a may not be precise because the offset interval (50nm) used for FDTD modeling is not small enough to resolve the periods exactly. Nevertheless, the two field maps for bright and dark modes shown in Figures 4.6b and c, respectively, depict how they evolve into opposite modes. For the bright mode, once the nanogap shifts, light transmitted directly from the nanogap starts to cancel the SPPs propagating at the trench resonator, being out-of-phase with the anti-node of the SPPs. For the dark mode, when the nanogap position shifts by half the wavelength of the SPPs, the light is in-phase at the node. Breaking symmetry allows the dark mode to be excited.^{126, 128, 129} This phenomenon can benefit various fields such as plasmonic biosensing¹²⁸ and opto-electronic modulation^{130, 131} due to sharp resonance.

4.3.4 Design of sidewall mirrors

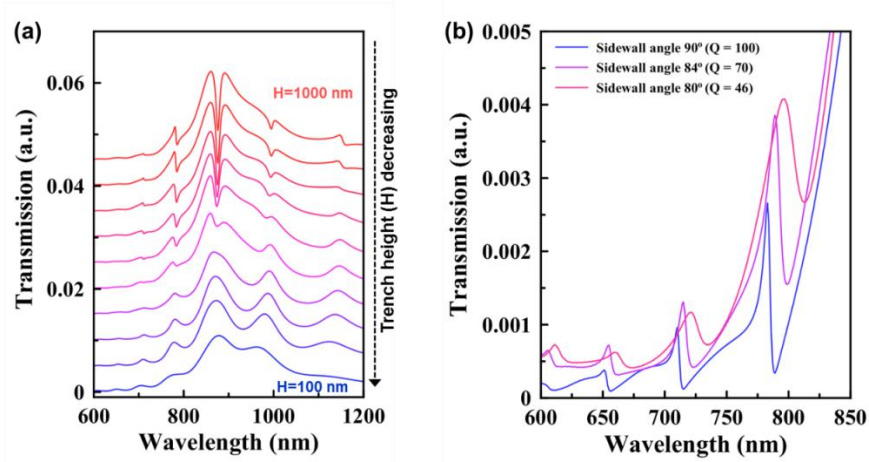


Figure 4.7 The effect of geometrical difference in the sidewall mirrors on resonance. (a) The effect of sidewall height (H) on resonance. As the height of the sidewall is reduced from 1000nm to 100nm, the resonances begin to broaden, and eventually, they disappear. (b) The effect of sidewall angle (α) on resonance. The vertical sidewall ($\alpha = 90^\circ$) shows a sharp Fano resonance. The Q factor decreases with the sidewall angle (α).

Sidewalls in a trench resonator act as the reflection mirrors and thus create sharp resonance peaks. If the reflection of SPPs from the sidewalls is not perfect, then the trench resonator cannot store strong optical energy without a dissipation of energy. Therefore, it is important to study the effect of geometrical differences in the sidewall mirrors on the resonance shape. First, as the height of sidewall decreases from 1000nm to 100nm, the multiple sharp resonance peaks begin to broaden, and eventually, they disappear as plotted in Figure 4.7a. Given FDTD modeling of a trench resonator, the evanescent field of SPPs is as tall as the trench height, although the SPPs are decaying perpendicular to the propagating direction. Therefore, the shorter the sidewall, the smaller the reflection. For example, a 1 μ m-high sidewall has a reflectance of 99%, while a 500nm-high sidewall reflects only 45% of incoming SPPs. Therefore, a 1 μ m-high sidewall was implemented in this device. Figure 4.7b shows the effect of the sidewall angle (α) on the resonance. A vertical sidewall ($\alpha = 90^\circ$) shows a sharp resonance peak. However, a tilted sidewall can scatter light partially to the far-field, reducing the light reflecting back to the trench. As a result, its Q factor decreases with a decreasing sidewall angle (α).

4.4 Fabrication of trench nanogap resonators

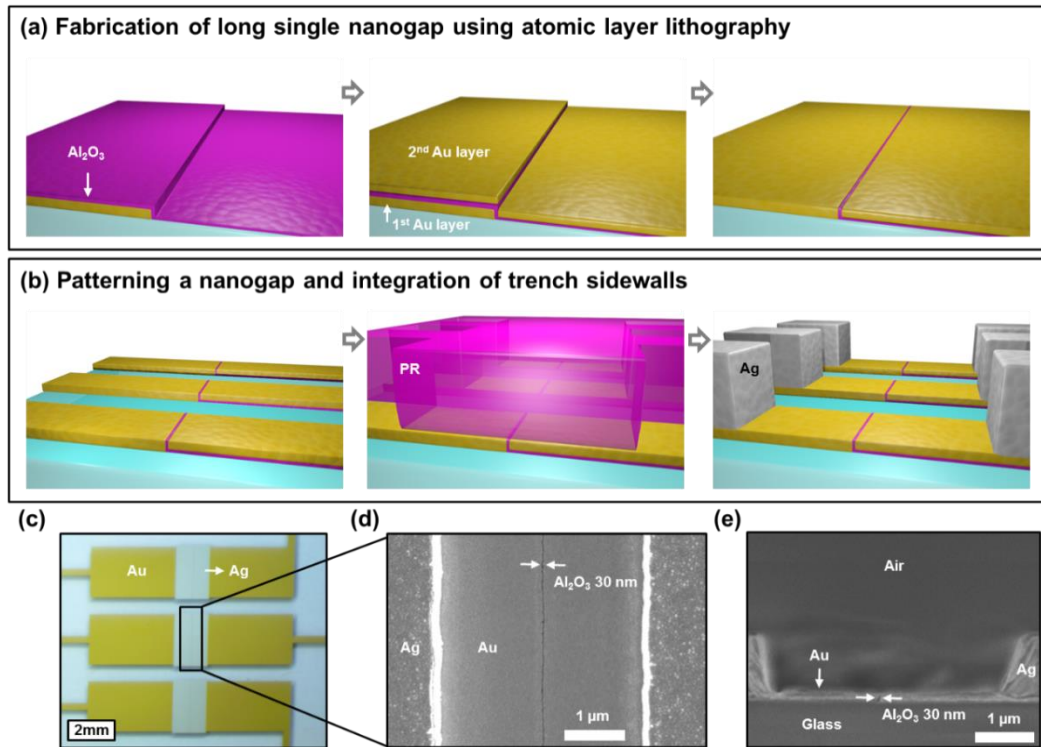


Figure 4.8 (a) Fabrication of long single nanogap via atomic-layer lithography. (b) Patterning a single nanogap structure and integration of trench sidewalls on the patterned nanogap. (c) Image of chip including multiple trench resonators. (d) Enlarged SEM image of trench resonator. (e) Cross-sectional SEM image of trench resonator.

As illustrated in Figure 4.8a, I employed atomic layer lithography³² to produce a metallic, sub-10nm nanogap for trench resonators combined with sidewall mirrors. First, a 150nm-thick Au film with 5nm Cr adhesion was patterned using conventional photolithography and the liftoff process. After creating a 30nm thick alumina using the ALD technique, a 120nm-thick Au with 5nm Cr adhesion was evaporated on the alumina-coated Au patterns. Using directional metal evaporation, I filled the empty patterned area with metal. The Au layer placed on top of the Au patterns was then peeled off using adhesive tape.³² Tape-based planarization allowed me to reproduce the centimeter-long, sub-10-nm nanogap. The nanogap was then divided into multiple line patterns using photolithography and ion milling as shown in Figure 4.8b, followed by additional photolithography on top of the multiple line patterns to make sidewalls. Subsequently, I created metallic sidewalls

on the left and right wings of the nanogap using 1 μ m-thick Ag deposition and liftoff as illustrated in Figure 4.8b. The offset between the nanogap and the surrounding trench can be manipulated by carefully aligning a Cr photomask during a second round of photolithography. Figure 4.8c shows the chip image including multiple trench resonators. Zoomed-in SEM images in Figures 4.8d and e show the shape of the trench resonator in detail. The width and height of the trench are 3.4 μ m and 1 μ m, respectively. A 30nm-wide alumina-filled nanogap is at the center of the trench width. The cross-section of this device in Figure 4.8e discloses that its sidewalls are angled owing to the shadowing effect during metal evaporation. Despite this fabrication imperfection, multiple centimeter-scale trench resonators were successfully fabricated on a 4-inch glass wafer.

4.5 Experimental characterization of trench nanogap resonators

For transmission measurements in the visible wavelengths, the trench resonator was illuminated with a halogen thermal lamp through a condenser on an inverted microscope (Nikon, Ti-S), and the light transmitted was collected with a 10X objective and imaged onto the entrance slit of a 300mm focal length imaging spectrometer (Acton SP2300i) equipped with a CCD camera (Princeton, Pixis 400). Spectra were background subtracted and normalized using the spectrum for direct transmission through the glass substrate.

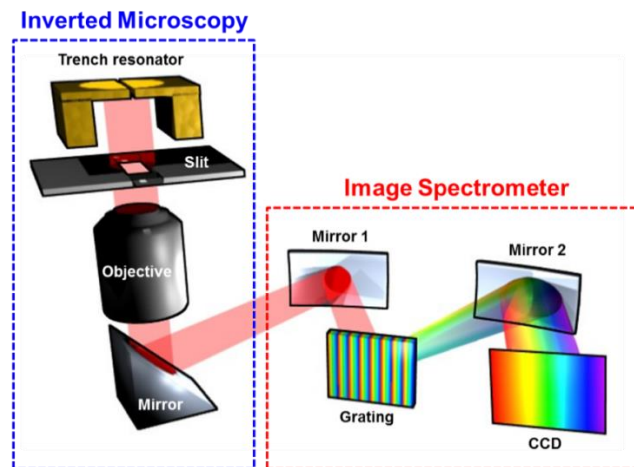


Figure 4.9 Optical measurement setup for trench resonator.

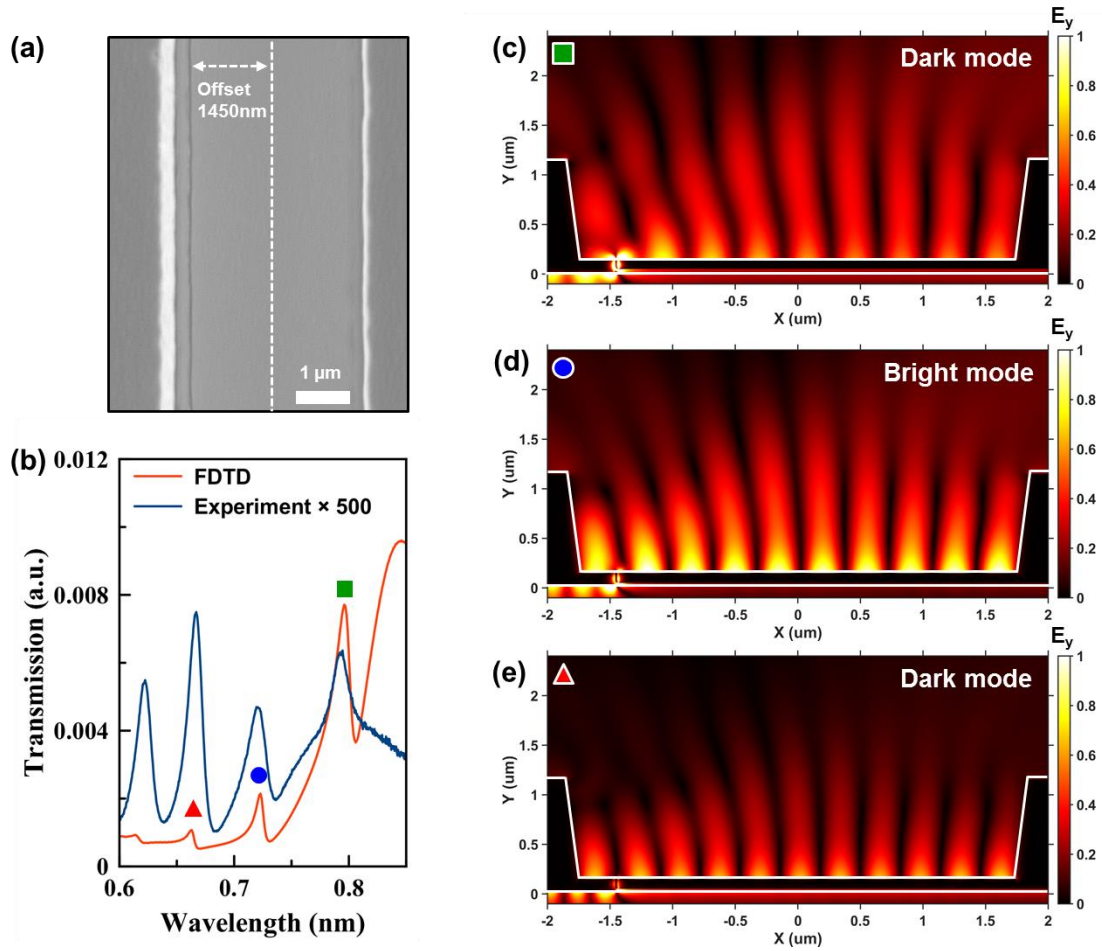


Figure 4.10 Experimental measurements of optical transmission through trench nanogap resonators. (a) SEM image of a trench resonator with a 30nm gap (1450nm off center). Trench width and height are 3450nm and 1000nm, respectively. (b) Measured (blue) and simulated spectra (red) from an asymmetric trench resonator shown in Figure 4.10a are compared. (c-e) Spatial distributions of the E_y field for transmission peak wavelengths of 790nm, 730nm, and 670nm, respectively.

As shown in Figure 4.10a, I fabricated an asymmetric trench resonator with a 30nm nanogap aligned at 1450nm-left-shifted from the center of the trench. The optical transmission spectrum through this structure was measured using an image spectrometer integrated with a CCD camera. The detailed optical setup is illustrated in Figure 4.9. In Figure 4.10b, the measured spectrum from the asymmetric trench resonator exhibits four sharp Fano-type resonances in the visible regime. The transmission peak at the wavelength of 670nm has a maximum Q factor of 50,

which is lower than the Q factor of 130 calculated from FDTD modeling, even though 50 is still high quality in terms of a plasmonic resonator. A reason for the degradation in Q factor is the loss from the tilted sidewalls as mentioned in Figure 4.7b. Tilted sidewalls can affect the Q factor of resonance by scattering light into the far-field, decreasing stored optical energy inside the trench resonator. Also, the roughness of the trench surface may increase metallic losses. The sidewall angle measured from the SEM image was approximately 84 degrees, which was used for FDTD simulations. The FDTD-calculated spectrum from an asymmetric trench resonator was plotted in Figure 4.10b for comparison. The measured and modeled transmission peaks and dips matched. However, there is a discrepancy between the measured and modeled intensities, which may be a result of the normalization process. This device is a single aperture-type structure, not an array or periodic structure. In the FDTD simulation, therefore, the beam of light sent through the glass substrate is as large as the model window size, in this case, 10 μ m. In the experiment, however, the beam size of the incident light via 10 \times object is much larger than in FDTD modeling, which makes it difficult to get the exact normalization from single-type aperture.

Next, the resonance mode for each peak was investigated using the spatial distribution of the E_y field at the wavelength corresponding to the transmission peaks marked with a square, circle, and triangle. The field map at 790nm shows nine half wavelengths of SPPs inside the trench resonator. Odd integers of $\frac{\lambda_{SPP}}{2}$ can be sustained by a dark mode arising from broken symmetry. Therefore, the transmission peak at 790nm results from the excitation of a dark mode. The transmission at 730nm corresponds to a bright mode with 10 half wavelengths of SPPs. At the wavelength of 690nm, a higher dark mode with eleven half wavelengths of SPPs occurs again. As seen in the experiment and modeling, if the nanogap is positioned between in-phase and out-of-phase, then two modes can be excited at the same time, leading to multiple transmission peaks.

4.6 Refractive index sensitivity

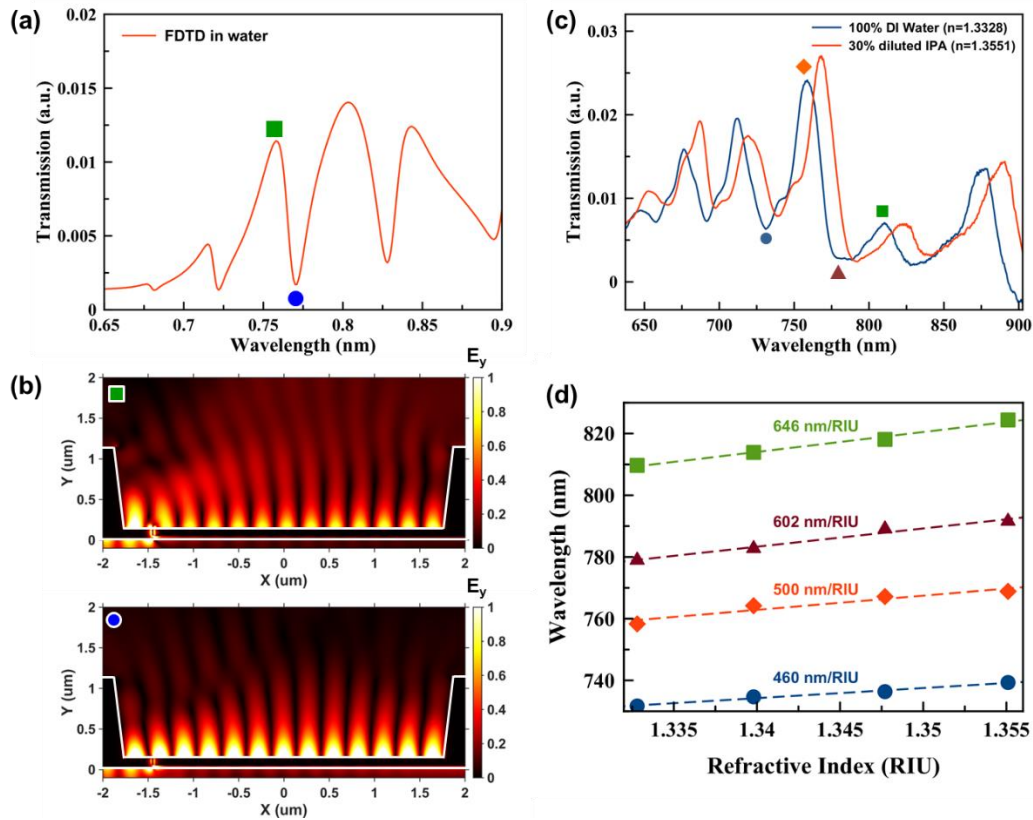


Figure 4.11 Bulk sensitivity of an asymmetric trench resonator. (a) FDTD-simulated transmission intensity from an asymmetric trench resonator with 1450nm offset in water environment. (b) Spatial distributions of the E_y field in an asymmetric trench nanogap with 1450nm offset in a water environment at the peak and dip (marked as a square and circle). (c) Measured optical transmission spectra from the asymmetric trench resonator (1450nm offset) with varying refractive index in the surrounding medium. (d) Measured bulk index sensitivities from multiple peaks and dips of (c) marked as a square, triangle, diamond, and circle. Overall, high sensitivities are observed in an asymmetric trench resonator, compared to the sensitivity in the nanohole array.

Multiple resonances with high Q factors are very useful in biosensing applications because sensitivity is proportional to the Q factor of resonance. In this section, the sensitivity of an asymmetric trench resonator is investigated using the bulk refractive index changing method. Figure 4.11a shows the FDTD-simulated transmission intensity of an asymmetric trench resonator with 1450nm offset in a water environment, followed by analysis of E_y field profiles with

corresponding peaks and dips (squares and circles) in Figure 4.11b. When the trench is filled with water (RI=1.33), the resonance wavelengths red-shift. The selected resonance for field mapping is the excited dark mode, which shows different field profiles for peaks and dips. At the peak wavelength, E_y fields tend to radiate to the far-field, while at the wavelength of a dip, the E_y field is confined to the trench bottom surface with high field amplitude. Refractive index sensing was performed using mixtures of water and IPA in Figure 4.11c. Four transmission spectra were measured with mediums having four different refractive indexes. Solutions were prepared by adding IPA (0, 10, 20, and 30%) to DI water. A refractometer was then employed to get accurate refractive indexes from the prepared solutions. Bulk refractive index sensitivities from multiple peaks and dips were extracted as shown in Figure 4.11d. Overall, 600nm/RIU was observed in the asymmetric trench resonator.

4.7 Conclusion

To summarize, we have developed atomic layer lithography further by adding metal patterning and evaporation to build up trench nanogap resonators and investigate their optical characteristics. These results demonstrate a high Q factor of 50 by reducing the gap width to 30nm and find that transmission peaks occur in the destructive interference condition due to Fano resonance with a sharp phase shift of π , not at the constructive interference condition. Furthermore, asymmetric nanogap apertures enable suppressed dark modes to be excited, resulting in multiple resonances. Trench nanogap resonators with multiple transmission peaks and dips demonstrate the potential for biochemical plasmonic sensing by showing high refractive index sensitivities of around 600nm/RIU. The combination of atomic layer lithography with additional processes such as ion-milling and metal evaporation allows us to engineer metallic nanogap apertures, thus leading to novel optical properties. High-Q-factor plasmon resonances created in a trench resonator can be harnessed for biosensing,^{101, 102} surface-enhanced spectroscopies,^{87, 104} and plasmonic lasers.¹¹⁵

Chapter 5

Electrically-active trench nanogap resonators

Surface plasmon resonance (SPR), the collective charge oscillation of conduction electrons on metal surfaces,³⁹ has opened the door for refractometric sensors,⁵ which have been widely used for measuring molecular binding kinetics and affinity^{5, 132, 133}. SPR-based biosensors are founded on the change in the surface refractive index (RI) caused by the adsorption of analytes to the metal sensing surface.¹³³ Therefore, the performance of surface-based biosensors is governed by the rate of surface reactions and mass-transport limitations due to diffusion.^{134, 135} The surface-reaction limit is associated with the binding interaction at the surface and the sensitivity of the device. Diffusion-limited transport depends on the concentration of analytes in the bulk solution. So, low concentration detection is limited by the diffusion rate of analytes. It is known that it could take many hours to detect analytes from picomolar (pM)-level concentration.¹³⁶

To overcome the diffusion limit in surface-based biosensors, various strategies have been explored to concentrate sparse analytes on the sensing surface by using evaporation-driven concentration of sample droplets¹³⁷ or by applying convection to push molecules through nanoholes.¹³⁸⁻¹⁴⁰ Such approaches have been demonstrated successfully, but also have a drawback in that they are passive delivery mechanisms that can only push analytes toward the sensing surface, but cannot fully manipulate them. On the other hand, dielectrophoresis (DEP) has been widely employed for actively manipulating particles in a surrounding medium via the interfacial charge distribution induced in a spatially non-uniform electric field.¹⁴¹ Recently, various SPR nanostructures, which can tailor local electric fields using their sharp geometries, have been explored to integrate SPR biosensing with DEP force.¹⁴²⁻¹⁴⁴

In this chapter, I introduce a novel, DEP-enhanced SPR biosensor using a trench resonator. In the trench resonator, the metal film at the bottom of the trench is separated electrically by a thin alumina layer, which enables the device to operate as a two-terminal electrical device. Specifically, the optical “hot spot,” which is sensitive to the refractive index change, also corresponds to the strongest field intensity that can thereby boost DEP force.

5.1 Dielectrophoresis

Dielectrophoresis (DEP) is the movement (translation or rotation) of a polarizable particle originating from its induced charge in a spatially non-uniform electric field.¹⁴¹ The direction of motion induced by DEP is determined by the charge distribution at the interface between a particle and its surrounding medium. As shown in Figure 5.1, the direction of the net dipole depends on the interfacial charge distribution. For example, if a particle is more polarizable than a medium so that it has more interfacial charges, then the net dipole is generated in parallel to the applied electric field. On the contrary, relatively more interfacial charges in a medium due to high polarizability induce a net dipole with an opposite direction to the applied electric field. The direction of the net dipole can be manipulated by the frequency of the applied electric field because polarizability in materials is frequency-dependent.

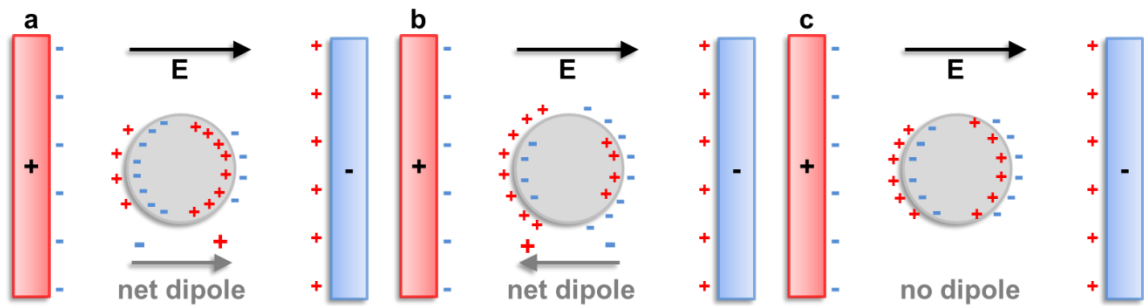


Figure 5.1 Schematic diagrams of three different cases in the polarization of a dielectric particle in a surrounding medium. (a) A particle more polarizable than the surrounding medium produces more charges inside the particle inducing net dipole in parallel to the applied electric field. (b) A particle in a more polarizable medium yields a net dipole in the opposite direction to applied field. (c) There is no net dipole when the charges on either side are equivalent.

In a uniform electric field, no net force is induced on a particle, because the net interfacial positive and negative charges on either side are the same. On the other hand, in a non-uniform electric field, the balance between positive and negative charges on either side is broken, thus enabling net force to apply to a particle body as depicted in Figure 5.2. The net force generated can move a particle according to the direction of the net dipole determined by the frequency of the applied electric field.¹⁴⁵ Figure 5.2b shows a positive DEP force at low frequency while the negative DEP force is seen in Figure 5.2c.

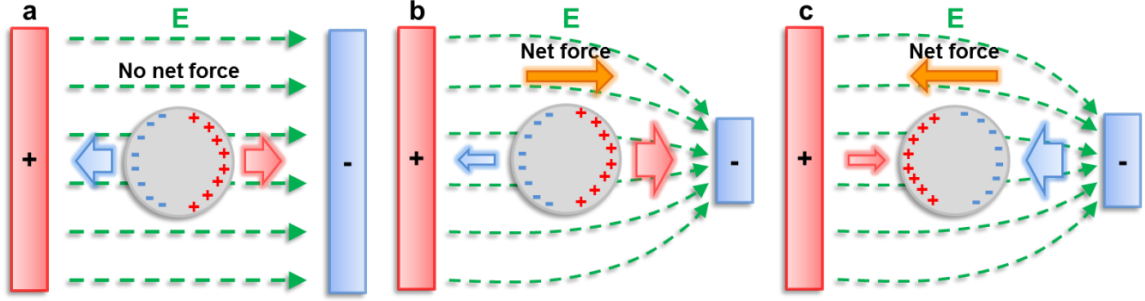


Figure 5.2 Schematic diagram of how different DEP forces occur. (a) In a uniform field, two forces with the same strength but opposite directions are canceled out as there is no net force. (b) A highly-polarizable particle in a non-uniform field has a large attractive force where the electric field is localized. The net force generated pushes the particle toward the high electric field. (c) In a highly-polarizable medium, a particle experiences a larger repulsive force, moving it in the opposite direction, against the electric field.

The behavior of DEP force can be described by the effective polarizability calculated from the effective dipole moment of a spherical particle. The potential of a dipole and the boundary condition for the potential at the surface of the sphere give the effective dipole moment:^{141, 145}

$$\mathbf{p} = 4\pi\epsilon_m \left(\frac{\tilde{\epsilon}_p - \tilde{\epsilon}_m}{\tilde{\epsilon}_p + 2\tilde{\epsilon}_m} \right) a^3 \mathbf{E} \quad (5.1)$$

where, $\tilde{\epsilon}_p$ is the complex permittivity of the particle and $\tilde{\epsilon}_m$ is the complex permittivity of the medium, and a is the radius of the spherical particle.

The effective dipole moment of the sphere can be expressed in the volume of the sphere (v) and the complex effective polarizability ($\tilde{\alpha}$) as

$$\mathbf{p} = v\tilde{\alpha}\mathbf{E} \quad (5.2)$$

From equations 5.1 and 5.2, the effective polarizability can be derived as the follow:

$$\tilde{\alpha} = 3\epsilon_m \tilde{f}_{CM}, \quad \text{where } \tilde{f}_{CM} = \left(\frac{\tilde{\epsilon}_p - \tilde{\epsilon}_m}{\tilde{\epsilon}_p + 2\tilde{\epsilon}_m} \right) \quad (5.3)$$

This is referred to as the Clausius-Mossotti (CM) factor, which is the complex function that governs the behavior of the DEP force according to the frequency of the applied electric field. Figure 5.3 shows the frequency variation of the real (solid line) and imaginary (dotted line) parts of the Clausius-Mossotti factor for a latex sphere, with $\sigma_p \gg \sigma_m$ and $\epsilon_p \ll \epsilon_m$. At low frequencies, the real part of \tilde{f}_{CM} approaches 1 while it approaches -0.5 as the frequency increases.

The force on the induced dipole in non-uniform ($\mathbf{F} = (\mathbf{p} \cdot \nabla)\mathbf{E}$) and dipole momentum (5.2) give the time-average DEP force as the following:

$$\mathbf{F}_{DEP} = \pi\epsilon_m a^3 \text{Re}[\tilde{f}_{CM}] \nabla |\mathbf{E}|^2 \quad (5.4)$$

As described in equation 5.4, DEP force is proportional to the electric field intensity gradient and its direction is determined by the CM factor. However, DEP force decreases with the volume of a particle ($\propto a^3$). Therefore, a very high electric field intensity gradient is required in order to trap nanometer-scale particles such as viruses and biomolecules. A high electric field gradient can be generated in miniaturized geometries such as sharp electrode edges,¹⁴² metallic tips,¹⁴⁴ and nanoscale gap electrodes.^{146, 147} Since DEP is a scalable technique, sub-10nm metallic nanogaps fabricated using atomic layer lithography,³² as introduced in the previous chapter, can boost DEP forces. Furthermore, a trench resonator with a 10nm metallic nanogap has an optical “hot spot” near the nanogap which is very sensitive to the changing surface index, thereby making the trench resonator a promising structure for DEP-enhanced SPR sensing.

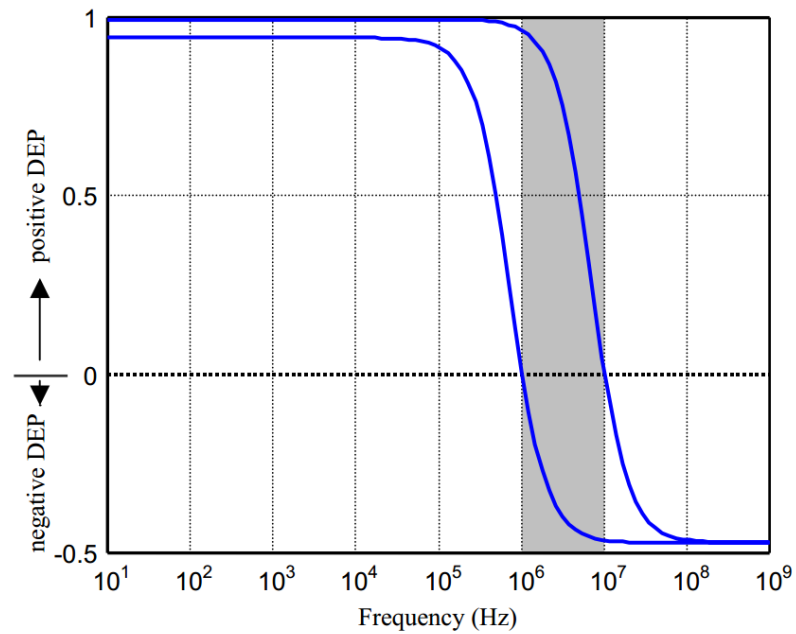


Figure 5.3 Plot of the normalized CM factor as a function of frequency for two different particles. In the shaded area, one particle experiences positive dielectrophoresis and the other negative dielectrophoresis, enabling separation in this frequency window. Reprinted with permission from Morgan *et al.*¹⁴⁵, Copyright 2003 Research Studies Press.

5.2 On-chip biosensor: DEP trapping in a trench resonator

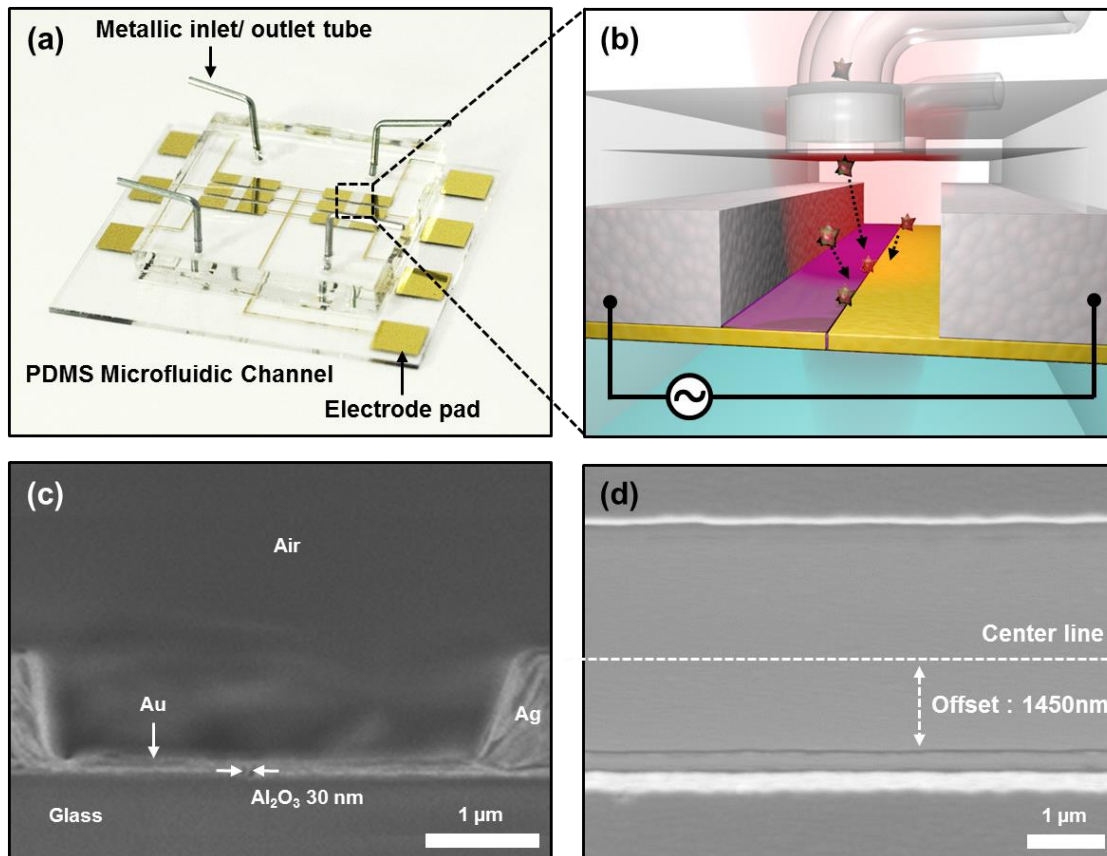


Figure 5.4 Dielectrophoresis (DEP) in a trench resonator. (a) Image of an on-chip multiple trench resonator with biosensor-integrated electrode pads. Six trench resonators are placed on one chip with one shared electrode and an electrode connected to each device, which allows each device to be activated individually and electrically. (b) Illustration of the trapping of biomolecules via DEP force in the electrically-activated trench resonator. The high electric field gradient induced by the 10nm gap generates a strong DEP force, which enables sub-micron-sized particles or biomolecules to be trapped at the nanogap. (c-d) SEM images of the asymmetric trench resonator from the side and from above, respectively.

First, I built trench resonator biosensors with multi-electrodes on a glass wafer using a combination of atomic layer lithography and additional patterning processes. This chip was then integrated with a PDMS microfluidic channel and inlet-outlet metallic tubes. The 15nm alumina and 5nm silica films were sequentially coated on the trench resonator using the ALD technique. After the silica

and PDMS surfaces were exposed to oxygen plasma for ten seconds using reactive ion etching (STS), I connected the two surfaces to create a strong dangling bond between the activated Si and O. Then, I connected the metallic inlet and outlet tubes through the PDMS microfluidic channels. Finally, I created the 1-inch-by-1-inch, on-chip, trench resonator biosensor with multi-channels and multi-electrodes as shown in Figure 5.4a. Each trench resonator has one shared electrode and its own electrode, which allows each device to work individually. The trench resonator was designed for the left and right side trench wings to be separated by a 10nm alumina layer, which allowed the resonator to act as DEP-enhanced plasmonic biosensor. Figure 5.4b shows how sub-micron-sized particles and biomolecules were trapped at the nanogap by the strong DEP force generated by the high electric field and detected by SPPs in the trench resonator.

Even very low voltages below 1V can induce a very strong electric field at the nanogap, since the electric field generated is inversely proportional to the space between the two metallic electrodes. 2D finite element method (FEM) modeling was used to investigate the electric field intensity induced across the 10nm alumina gap as depicted in Figure 5.5a. The dimensions from an actual asymmetric trench resonator were used for this modeling. Figure 5.5a shows the spatial distribution of the electrostatic field intensity in an asymmetric trench resonator when applying 1V. A strong electrostatic field was built up at the 10nm nanogap and produced a huge electric field intensity gradient. In Figure 5.5b, the gradient is extracted along the white dashed line extending vertically from the nanogap of Figure 5.5a and plotted with the distance from the nanogap. The gradient of electric field intensity increases exponentially as it approaches to the nanogap. The huge field gradient enabled the trapping of sub-micron-sized particles and biomolecules near the nanogap under low operating voltages.

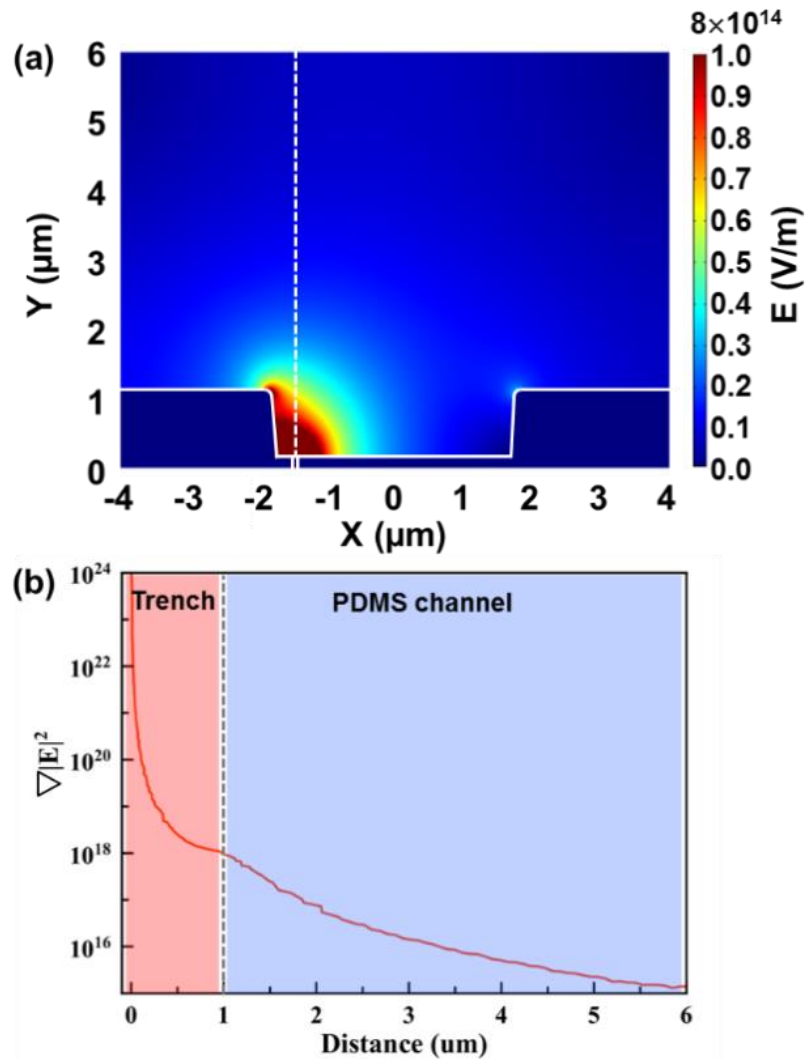


Figure 5.5 FEM modeling of the electric field intensity in the 10nm gap electrode of the trench resonator structure. (a) Spatial distribution of the static electric field intensity in the trench resonator electrode when 1V was applied to two electrodes. Strong static electric field intensity is accumulated near the nanogap inside the trench channel. (b) The gradient of the static electric field intensity extracted along the white dashed line extending vertically from the nanogap and plotted with the distance from the nanogap. The huge field gradient inside the trench channel was very useful for trapping particles via DEP.

5.3 Transmission measurement of trench resonator in water

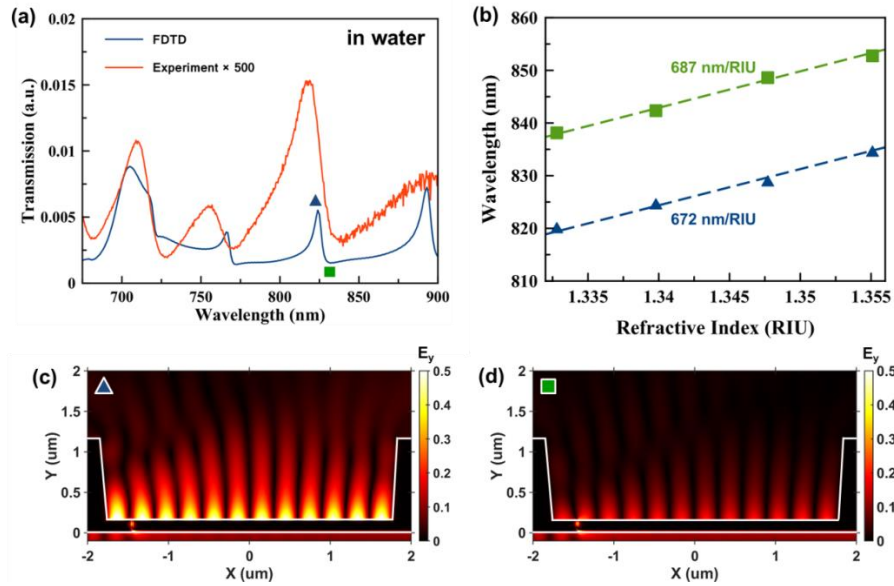


Figure 5.6 Optical transmission spectrum from an asymmetric trench resonator biosensor immersed in water. (a) A 2D, FDTD-modeled spectrum was compared with the experimentally-measured one. The blue solid line is the FDTD-simulated one and the red solid line is the measured one. (b) Bulk index sensitivity was measured experimentally by varying the refractive index in the medium. The green squares were tracked at the transmission minimum at the wavelength of 775nm. The blue triangles were measured at the transmission maximum at the wavelength of 750nm. (c-d) The electric field distributions of the asymmetric trench resonator in water at the wavelengths of 766nm and 772nm, respectively.

The transmission spectrum from an asymmetric trench resonator with a 10nm gap in water was investigated numerically and experimentally. Multiple transmission peaks and dips were observed through an image spectrometer with an inverted microscope. 2D FDTD modeling was simulated to identify the resonance mode corresponding to each peak. As seen in Figure 5.6a, dip positions in the measured and calculated spectra matched while the peak positions showed more discrepancies. The shape of the resonance for the 10nm gap was broad compared to the 30nm gap. The increased gap may affect peaks to blue-shift. In Figures 5.6c and d, the field distribution of the trench resonator in water was carried out to identify the resonance mode. It can be seen that the trench resonator in water has an odd number of lobes, and positioning the nanogap at the left side disturbs the interference with propagating SPPs, leading to excitation of the dark mode. The refractive index

sensitivity was also measured by varying the refractive index in the solution as shown in Figure 5.6b. Green squares were tracked at the transmission minimum at the wavelength of 775nm. Blue triangles were measured at the transmission maximum at the wavelength of 750nm. High sensitivity of about 690 nm/RIU was calculated in both peaks and valleys.

5.4 Experiment of dielectrophoretic-enhanced plasmonic sensing

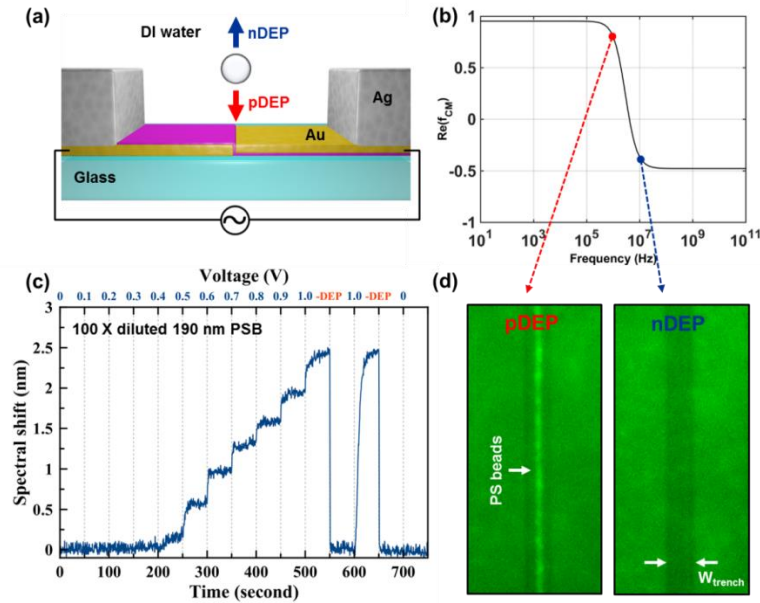


Figure 5.7 Dielectrophoretic manipulation of 190nm fluorescent polystyrene (PS) beads. (a) Schematic of the experimental setup for dielectrophoretic concentration of analyte molecules. The AC electric field is applied to left and right side wings, generating a strong field intensity gradient across a 10nm gap. The strong DEP force generated from the nanogap pulls dielectric particles at a low frequency, and pushes them at a high frequency. (b) Frequency dependence of the real component of the CM factor for solid polystyrene beads suspended in a surrounding medium of conductivity 0.28 Ms/m. (c) Resonance shift as a function of time by increasing applied voltage (V_{pp}) from 0 to 1V and then repeating positive and negative DEP by altering the frequency from 1MHz to 10MHz. (d) Optical fluorescence images through a green filter when PS beads are trapped and de-trapped at the nanogap at 1MHz (low frequency) and 10MHz (high frequency), respectively.

I demonstrated the manipulation of dielectric particles via DEP by monitoring resonance shift as well as fluorescence image. Figure 5.7a provides a schematic of the DEP setup in a trench resonator. The left and right sides of the trench resonator were connected with an AC voltage supply.

Fluorescent polystyrene beads (190nm diameter, center emission wavelength of 600nm, Bangs Laboratories, Fishers, IN) were diluted 100 times with DI water, then applied to the trench resonator with a PDMS chamber and sealed in with a cover glass. Optical measurement (exposure time: 0.5s, 10x objective) was carried out in the same manner described in Chapter 4. The DEP-based SPR sensing was performed with an AC electric field from 0 to 1V, and a frequency range from 1MHz to 10MHz. Based on the calculated CM factor in this system, 1MHz and 10MHz were selected as operating frequencies for positive DEP and negative DEP, respectively. Figure 5.7c shows time-resolved SPR sensing as a function of the applied voltages. The transmission minimum at the wavelength of 774nm was monitored and tracked using a polynomial fitting equation in Matlab. During the first 50 seconds, no voltage was applied, then voltage increments of 0.1V were applied every 50 seconds with a frequency of 1MHz. No resonance shift was observed up to 0.3V, but spectral shift appeared at 0.4V and increased with the voltage up to 1V as the positive DEP force increasingly attracted the PS beads into the sensing volume close to the nanogap. Next, the frequency was switched to 10MHz at 1V. This resulted in an abrupt drop in spectral shift owing to a strong repulsive force known as negative DEP. One more cycle of positive and negative DEP was repeated before the voltage was turned off at 700 seconds, and a steady baseline was observed for 50 seconds.

In a separate experiment, fluorescent images were recorded at regular time intervals of 10 seconds using a Photometrics CoolSNAP HQ2 CCD camera and Mirco-Manager software in order to confirm whether or not the trapping and releasing of the PS beads occurred as a function of the AC bias. The fluorescent PS beads were trapped along the nanogap during the positive DEP operation and pushed away from the nanogap by the negative DEP force as shown in Figure 5.7d. The spectral shift behavior with varying voltage was clearly understood to be a result of DEP force acting on this device. The electrically active trench resonator successfully demonstrated positive DEP trapping of nanoscale particles (190nm PS beads) at a very low voltage of 0.4V. In experiments with biomolecules, low operating voltages are desired to avoid practical problems such as high voltage-induced thermal convection and damage. To my knowledge, DEP trapping of nanoscale particles at 0.4V is a record in terms of DEP-implemented SPR biosensing. Furthermore, the clear dependence of applied voltage on resonance shift allows us to study DEP force on nanoscale objects qualitatively and quantitatively. In addition, the strong DEP force arising from the high electric field at a 10nm gap enables a very fast response time compared to previously reported results.

5.5 Limits of detection: size and concentration

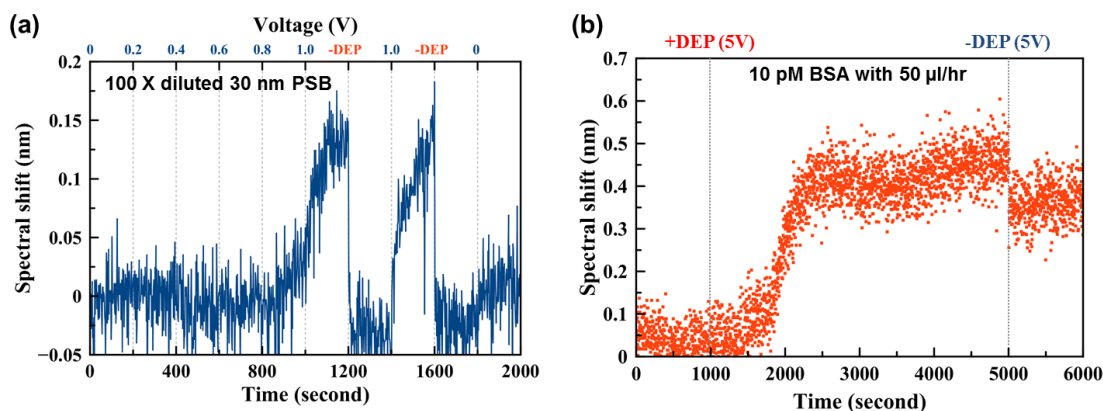


Figure 5.8 Experiments for limits of detection. (a) Trapping of 30nm-sized PSB. Resonance shift as a function of time by increasing applied voltage (V_{pp}) from 0 to 1V and then repeating positive and negative DEP by altering the frequency from 1MHz to 10MHz. (b) Trapping of biomolecules of BSA with 10pM. BSA was injected into the PDMS channel using a syringe pump with a flow rate of 50 μ l/hr. After 1000 seconds, positive DEP appeared with 5V and 1kHz, and turned to negative DEP (10MHz) at 5000s.

The limits of detection for DEP-enhanced plasmonic biosensing are demonstrated in terms of detectable size and concentration. First, the trapping of 30nm-sized PSBs was carried out with an applied voltage of 1V. Figure 5.8a shows resonance shift as a function of time by increasing applied voltage (V_{pp}) from 0 to 1V and then repeating positive and negative DEP by altering the frequency from 1MHz to 10MHz. For 30nm beads, the resonance shift did not increase until 0.8V, and the signal started to go up at 0.8V. At 1V, changing the frequency from 1MHz to 10MHz caused a negative DEP and dropped signal. One more cycle of positive and negative DEP was monitored by tracking resonance shift. Comparing the resonance shifts of 190nm and 30nm beads, the 190nm PSBs had a much stronger signal. According to equation 5.4, DEP force decreases with the volume of particles. Therefore, the decrease in detection signal can also be explained by the size effect. Nevertheless, the trench nanogap resonator successfully trapped 30nm PSBs under very low voltage like 0.8V. This can be attributed to the very high electric field generated across the nanogap.

Furthermore, a highly-diluted BSA (molecular weight: 65 kDa, Sigma-Aldrich) was employed to demonstrate the potential of DEP-enhanced plasmonic sensing for detecting protein

molecules at low concentrations. BSA was dissolved in a water medium of conductivity = 0.28 mS/m until its concentration met 10pM. In the experiment on low concentration, PDMS microfluidic channels were integrated with trench nanogap resonators. BSA was injected into the PDMS channels using a syringe pump with a flow rate of 50 μ l/hr and the trapping of BSA near the nanogap was monitored by recording the resonance spectra every 2s. After 1000s, positive DEP appeared at 5V and a frequency of 1kHz and switched to negative DEP at 5V and a frequency of 10MHz at 5000s. During the 500s after the positive DEP turn-on at 1000s, the signal did not shift, but started to increase at 1500s. It then got saturated over 2500s and lost signal intensity when negative DEP turned back on at 5000s. In this experiment, the signal delay for detection is observed due to low concentration. Also, the signal did not return to the baseline when negative DEP turned on. This may be because the BSA molecule is known as a sticky molecule and it could be difficult for a negative DEP force to push them away from sensing spots. Overall, the DEP-enhanced plasmonic sensor successfully demonstrated the trapping of protein molecules with a low concentration of 10pM within 1500s. The time of detection is defined as the time it takes to accomplish the concentration of the analyte molecule that generates a signal three times higher than the noise level of the sensor.¹³³ The trapping of protein molecules with 10pM was performed within 20min. Compared to the diffusion-transport limit, the DEP force accelerated the time of detection by 23 times.¹⁴²

5.6 Conclusion

In this chapter, I demonstrated DEP-enhanced plasmonic biosensing using electrically-active trench nanogap resonators. The combination of a strong electric field intensity gradient created across a 10nm nanogap aperture and the high sensitivity of a trench resonator enables active DEP-trapping of nanoscale particles and biomolecules to be monitored via a conventional SPR-biosensing setup. Using this powerful platform, I investigated DEP force on nanoscale particles with a 190nm diameter qualitatively and quantitatively, demonstrating DEP-trapping at 0.4V. Furthermore, this device manifests active plasmonic nanotweezers by demonstrating the active trapping of 30nm particles under 1V. Also, a DEP-enhanced plasmonic sensor overcomes diffusion-based limitations by largely reducing the time of detection at low concentrations like 10pM, and thus proving its potential as a powerful platform for biomolecular sensing.

Chapter 6

Other research results: Template-stripped tunable plasmonic devices on stretchable and rollable substrates

In this chapter, other recent research output will be presented. Template stripping is known as a versatile fabrication technology to manufacture high quality metallic nanostructures with high-throughput manner. This novel technique has been successfully demonstrated on the planar substrates like a Si wafer or a glass. In this work, I extend the versatility of this technique into the non-conventional substrate like stretchable and curved ones. Template stripping is employed to integrate metallic nanostructures onto flexible, stretchable, and rollable substrates. Using this approach, high-quality patterned metals that are replicated from reusable silicon templates can be directly transferred to polydimethylsiloxane (PDMS) substrates. First we produce stretchable gold nanohole arrays and show that their optical transmission spectra can be modulated by mechanical stretching. Next we fabricate stretchable arrays of gold pyramids and demonstrate a modulation of the wavelength of light resonantly scattered from the tip of the pyramid by stretching the underlying PDMS film. The use of a flexible transfer layer also enables template stripping using a cylindrical roller as a substrate. As an example, we demonstrate roller template stripping of metallic nanoholes, nanodisks, wires, and pyramids onto the cylindrical surface of a glass rod lens. These non-planar metallic structures produced via template stripping with flexible and stretchable films can facilitate many applications in sensing, display, plasmonics, metasurfaces, and roll-to-roll fabrication. The work presented in this chapter is mainly derived from the following publication:

Daehan Yoo, Timothy W. Johnson, Sudhir Cherukulappurath, David J. Norris, and Sang-Hyun Oh, “Template-Stripped Tunable Plasmonic Devices on Stretchable and Rollable Substrates”, ACS Nano, 2015, 9 (11), pp 10647–10654

6.1 Motivation of flexible optical and electrical devices

Metallic nanostructures such as nanoholes,¹ nanoparticles,^{41, 148, 149} and sharp tips¹⁵⁰ are key elements for plasmonics,¹³⁰ metamaterials,^{82, 151} and near-field optics.¹⁵⁰ Advanced top-down fabrication methods can produce precision-patterned metallic nanostructures on solid substrates such as silicon wafers.²⁵ Placing these metal nanostructures on stretchable substrates can add a new degree of freedom to plasmonic devices and metamaterials to mechanically tune their optical properties. These functional films can also wrap around non-planar surfaces for applications such as strain sensors,^{152, 153} touch panels,¹⁵⁴ curved displays,¹⁵⁵ and metasurfaces.¹⁵⁶⁻¹⁵⁸ To these ends, researchers have employed various methods such as transfer on polydimethylsiloxane (PDMS) films,¹⁵⁹ stencil lithography,¹⁶⁰ resist evaporation,¹⁶¹ transfer printing,¹⁶² and nanoskiving¹⁶³ to demonstrate metal nanostructures on unconventional substrates.

In this work, we demonstrate the potential of template stripping to produce stretchable metallic films. Template stripping has emerged as a versatile technique to produce smooth patterned metals with high throughput for plasmonics, metamaterials, and near-field optics.^{28, 164-170} Instead of directly patterning the metal films, here an inverse pattern is created in a reusable silicon template, replicated by a deposited metal film, and the patterned metal is removed from the silicon template. The use of crystalline silicon wafers for templates opens up many processing options such as plasma etching and crystal-orientation-dependent wet etching and enables films to be produced with much smoother surfaces than as-deposited metals. Previous work on template stripping demonstrated pattern transfers using optical adhesive, polyethylene films,¹⁶⁸ or as free-standing metal foils after electroplating.²⁸ Because this technique is based on transferring metals from a silicon wafer to a backing layer, it is possible to template-strip metals with stretchable films such as PDMS. Template stripping can produce planar films as well as 3D structures such as sharp metallic pyramids for imaging and spectroscopy applications.¹⁶⁹

We report detailed methods to transfer patterned metal films from a silicon wafer to PDMS and show examples of mechanically tunable plasmonic resonances using periodic gold nanohole arrays and pyramidal tips. We also show that template stripping can be performed using a roller to transfer the patterned metals on cylindrical surfaces.

6.2 Stretchable plasmonic nanohole device

Previous work on stretchable plasmonic devices focused on changing the distance between metal nanoparticles on a PDMS surface. Here we template-strip continuous patterned metal films using a PDMS backing layer and mechanically modulate their optical transmission spectra. After characterization of planar structures, we extend our method to gold pyramids.

6.2.1 Fabrication of stretchable gold nanohole arrays

Since the report of extraordinary optical transmission (EOT) in subwavelength hole arrays,¹ nanohole arrays patterned in metals have become one of the most extensively studied plasmonic structures for fundamental optical physics^{3, 44, 78, 171} as well as applications in spectroscopy,^{72, 93, 172} biosensing,¹⁷³⁻¹⁷⁵ and color filters.^{176, 177} High-throughput patterning of periodic nanohole arrays has been accomplished by techniques such as optical interference lithography,^{178, 179} colloidal lithography,¹⁸⁰ and template stripping.^{28, 167} Here we perform template stripping of large-area gold nanohole arrays with a stretchable PDMS film.

Our fabrication scheme is illustrated in Figure 6.1. First, a Si template is produced by creating a 2D array of deep circular holes (180 nm diameter and 500 nm periodicity) in a Si wafer using nanoimprint lithography (Nanonex, NX-B200) and reactive ion etching (STS-320). Then a 200-nm-thick Au film is deposited on the Si template through a shadow mask with an open area of 10 mm × 10 mm. During the metal evaporation process, nanoholes are naturally formed in the deposited Au film.

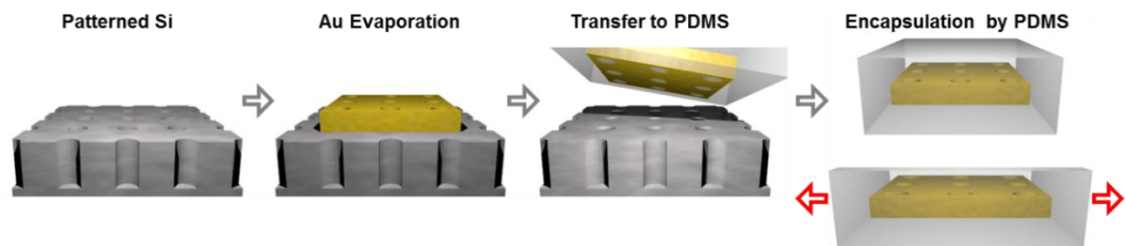


Figure 6.1. Stretchable gold nanohole arrays on a PDMS film. Schematic of the fabrication process. Figure is adapted from Yoo *et al.*¹⁸¹

Gold or silver films deposited on the oxidized surface of the Si template can readily be stripped using optical adhesive or sticky tape, but not with PDMS due to poor adhesion. Therefore we used

a self-assembled monolayer of 3-Mercaptopropyltrimethoxysilane (MPT) as an adhesion layer between the metal film and PDMS. The use of a Ti or Cr adhesion layer is not desirable because it can increase unwanted plasmon damping in the nanohole arrays. MPT is vaporized and immobilized on the exposed Au surface of the nanohole array film and also on the Si surface that is not covered by the gold film. Then PDMS is spin-coated on the gold film over the Si template. The MPT layer formed on the gold surface acts as an adhesion promoter for PDMS while the MPT layer formed on the Si surface prevents PDMS from sticking there.¹⁸² After curing the PDMS at 60 °C for 12 h, the perforated Au film, which is now adhered to the PDMS substrate, is template-stripped. A scanning electron micrograph (SEM) of a template-stripped periodic Au nanohole array (150 nm hole diameter) on the PDMS substrate is shown in Figure 6.2a. After template stripping, the top surface of the Au nanohole array is spin-coated again with PDMS for double-sided encapsulation during stretching experiments. This step also merges EOT peaks from both the top and bottom surfaces, simplifying the analysis of the EOT spectra.

6.2.2 Characterization of stretchable gold nanohole arrays

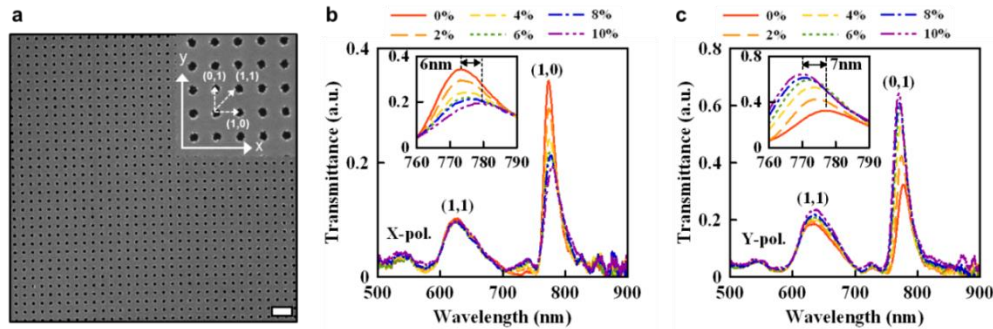


Figure 6.2 Stretchable gold nanohole arrays on a PDMS film. (a) Scanning electron micrograph (SEM) of a gold nanohole array template-stripped using a PDMS backing layer. Scale bar: 1 μm. Inset: Zoomed-in SEM of the nanohole array (150 nm hole diameter and 500 nm period). (b) Measured optical transmission spectra from a nanohole array stretched along the x axis and illuminated with x-polarized light. The unstretched nanohole array exhibits two main resonance peaks: the (1,1) Bragg resonance at 635 nm and the (1,0) resonance at 777 nm. After stretching in the x direction, the (1,0) resonance in the x-polarization red-shifts while its intensity decreases. (c) Transmission spectra for the nanohole array on PDMS stretched along the x axis with illumination with y-polarized light. In this case, the (0,1) peak shifts to shorter wavelengths and its intensity increases. Figure is adapted from Yoo *et al.*¹⁸¹

The fabricated Au nanohole array is stretched using a home-built tool. The optical transmission spectra of the nanohole arrays were measured with incident light that is polarized parallel (Figure 6.2b) or orthogonal (Figure 6.2c) to the stretching direction (x-axis) with a gradually increasing strain level. Before stretching, the nanohole array exhibits two main EOT peaks with wavelengths of 635 nm (FWHM=56 nm) and 790 nm (FWHM=16 nm). These peaks are the (1,1) and (1,0) Bragg resonances, respectively, using the following equation to approximate the peak position:⁴

$$\lambda_{spp} = \frac{a_0}{\sqrt{i^2 + j^2}} \sqrt{\frac{\epsilon_d \epsilon_m}{\epsilon_d + \epsilon_m}} \quad (6.1)$$

Here the integers (i, j) represent the Bragg resonance orders along the x- and y-axis, respectively, and ϵ_d and ϵ_m are the dielectric constants of the dielectric and metal, respectively.

As the nanohole array is stretched along the x-axis, parallel to the polarization of the incident beam, the corresponding (1,0) resonance peak red-shifts due to the increasing periodicity of the hole array (Figure 6.2b). As the circular holes are elongated in the x-direction with stretching, the electric field induced by surface charges becomes weaker and reduces the transmitted light intensity.¹⁸³ When the polarization of input beam is perpendicular (i.e. along the y-axis) to the stretching direction (x-axis), opposite trends are observed: here the (0,1) resonance peak [before stretching, the (1,0) and (0,1) resonances are degenerate and in the same position] blue-shifts while the intensity of the peak increases (Figure 6.2c). The observed blue shift can be explained by the contraction of the film along the y-axis when it is stretched along the x-axis, a relationship that is determined by the Poisson's ratios of the PDMS/Au composite film. The reduced array periodicity in the y-direction blue-shifts the peak wavelength. The peak intensity increases because of enhanced coupling of localized charges on the opposing edges of y-axial nanoholes.

The maximum spectral shift of the (1,0) or (0,1) resonance peak after stretching the PDMS substrate by 10% was about 7 nm and its measured linewidth (FWHM) was 20 nm. On the other hand, the (1,1) resonance peak does not move, as the change in length along the (1,1) direction is relatively small compared to change in the (1,0) and (0,1) directions. Our results indicate that the geometrical deformation of a nanohole array can induce polarization anisotropy in EOT. The changes in measured transmission spectra of nanohole arrays with stretching were compared with 3D finite-difference time-domain (FDTD) simulations (FullwaveTM, RSoft) as in Figure 6.3a and b. The measured spectral shift of 7 nm corresponds to only a 1% change in the length of the hole and periodicity while the entire substrate was stretched by 10%. The reason that the nanohole array only stretches by 1% is that cracks form in the surrounding substrate. Although the spectra were

measured from a large $200\ \mu\text{m} \times 200\ \mu\text{m}$ area of the nanohole array containing no cracks or wrinkles, the surrounding area of the full $8\ \text{mm} \times 8\ \text{mm}$ template-stripped sample had random cracking which accounts for the increased stretching of the total film.

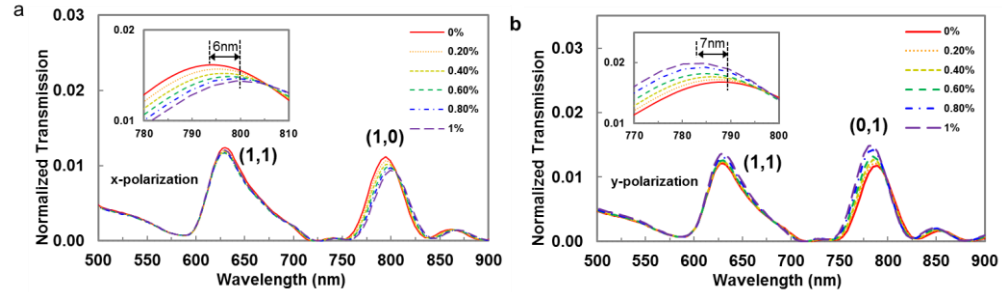


Figure 6.3 Finite difference time domain (FDTD) modeled transmission spectra from a nanohole array stretched along the x axis and illuminated with x-polarized light. (b) FDTD modeled transmission spectra for a nanohole array on PDMS stretched in the x axis with illumination with y-polarized light. To consider the deformation of shape in nanohole arrays we assumed that Poisson’s ratio of composite layer consisting of a 200 nm-thick Au layer and a 1 mm-thick PDMS layer is about 0.5 which is Poisson’s ratio of PDMS because PDMS is much thicker than the Au thin film. Thus, we expected the deformed shape of the nanohole arrays when stretched to follow the Poisson’s ratio of 0.5. Figure is adapted from Yoo *et al.*¹⁸¹

6.3 Stretchable plasmonic gold pyramids

Non-planar 3D structures can also be transferred onto PDMS. For example, below we use our approach to fabricate arrays of Au pyramids. Because our pyramids were constructed from a gold layer that is intentionally thinner on one facet, SPPs can be launched with internal (i.e. backside) illumination, leading to nanofocusing of SPPs at the pyramid tip.¹⁸⁴ The wavelength of the light scattered at the tip can then be modulated by regulating the angle of the pyramid facets with respect to the incident light via stretching.

6.3.1 Fabrication of stretchable gold pyramids

The fabrication process for asymmetric metallic pyramid arrays on a PDMS substrate is depicted in Figure 6.4. First, an array of circular patterns is made in a silicon nitride (Si_3N_4) film on a silicon wafer via photolithography (Karl Suss, MA-6) and dry etching (STS-320). Second, anisotropic Si

etching in a KOH solution^{165, 185, 186} creates inverted pyramidal pits in the exposed regions and the silicon nitride mask is removed (Figure 6.4a). Next, circular photoresist patterns that reveal individual openings of pyramids are made to isolate each pyramid (Figure 6.4b). Then a 135 nm-thick Au film and a 10 nm Ti adhesion layer are deposited at an incidence angle of 10° from normal by directional electron-beam evaporation (CHA, SEC 600), resulting in asymmetric Au pyramids with different Au thicknesses (45 and 120 nm) on opposing facets. After metal lift-off, an array of isolated, inverted Au pyramids is obtained (Figure 6.4c). Following O₂ plasma exposure to break bridging oxygen bonds on the Ti surface, PDMS (10:1 weight ratio mixture of base resin and curing agent) is spin-coated onto the Si template with the Au pyramidal pit array. After curing for 12 h at 60 °C, the PDMS layer is peeled off of the Si template (Figure 6.4d). SEMs of stretchable gold pyramids on PDMS are shown in Figures 6.4 e and f. The array of smooth and sharp Au pyramids can be fabricated over a large-area on PDMS as shown in Figure 6.4g.

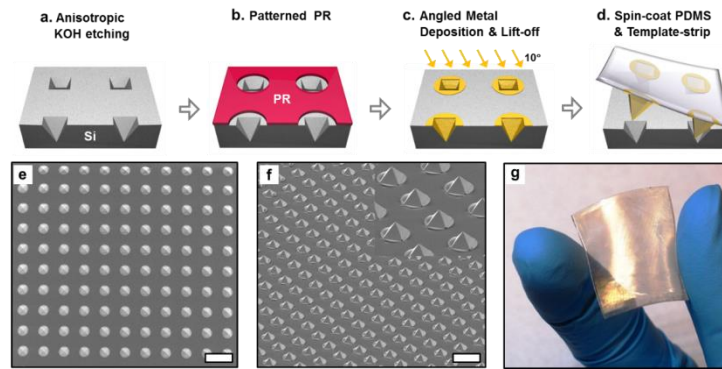


Figure 6.4 Fabrication of isolated gold pyramids template-stripped onto PDMS. (a) An array of pyramidal pits is formed by anisotropic etching in KOH through circular openings in a Si₃N₄ etch mask which is subsequently removed. (b) An array of 8 μm diameter circles in photoresist is patterned on top of the etched inverted pyramid array. (c) 135 nm of Au followed by 10 nm of Ti are deposited at 10° from normal using a directional e-beam evaporator. After lift-off, an array of disconnected, inverted Au pyramids is generated. (d) After oxygen plasma exposure to break bridging oxygen bonds, PDMS is spin-coated over the Au pyramidal pit array and cured at 60 °C for 12 h. The PDMS layer is then peeled off of the Si wafer. (e) Top-view and (f) bird's eye view SEMs of an Au pyramid array on a PDMS substrate. Scale bar: (e), (f) 20 μm. (g) Photograph of 1 inch x 1 inch flexible PDMS film fully covered with gold pyramids. Figure is adapted from Yoo *et al.*¹⁸¹

6.3.2 Characterization of stretchable gold pyramids

Optical property of gold pyramids transferred to PDMS substrate is investigated with stretching PDMS substrate. The base width of an unstretched pyramid as seen in Figure 6.5a is 7 μm . When the PDMS substrate is stretched by 10% and 20%, the base width of the pyramid increases by about 5% and 10%, respectively, because the region consisting of only PDMS is stretched more than the area covered with gold. Angled electron-beam evaporation of Au simultaneously creates a large array of pyramids with two different thicknesses on opposing sides (45 and 120 nm). Verification of this through cross-sectional imaging has been shown in a previous paper.⁴⁵ A 120-nm-thick Au film is optically opaque and hence blocks the incident light from the backside of the pyramid, whereas a 45-nm-thick Au film is optimal in exciting SPPs using a Kretschmann-like configuration. As illustrated in Figure 6.5d, stretching the Au pyramid changes the angle between the pyramid face and the incident light, which in turn changes the SPP coupling condition. Scattered light spectra from the pyramidal tip and spectral shifts caused by stretching the pyramid are shown in Figure 6.5e. All spectra were measured with white light polarized parallel to the stretching direction. The resonance peak wavelength, initially located at 545 nm without an applied force, gradually increases up to 682 nm as the applied force increases. The decreased incident angle of light as the pyramid stretches with the applied force causes the wavelength shift.¹⁵⁰ Assuming a conventional Kretschmann-like coupling mechanism,¹⁸⁷ the incident light with θ_{in} reflects at the interface between Au and PDMS, resulting in an evanescent field with in-plane momentum $k_x = \sqrt{\epsilon} \sin \theta_{\text{in}}$ propagating along the Au and PDMS interface, which excites SPPs at the interface between the Au and air. Thus, a reduced incident angle increases the wavelength of SPPs excited on the Au surface. The color green was observed at the tip when the resonance wavelength was located at 545 nm (Figure 6.5f) and the color red at 682 nm was seen for 9% strain. The wavelength of light scattered at the tip linearly increases with the mechanical strain, as shown in Figure 6.5g, demonstrating the tunability of the resonance by stretching a pyramid on the PDMS substrate. The pyramidal tips show a large resonance shift due to the strain, so large that the percentage change in wavelength is even larger than the percentage change in stretching. This high sensitivity to stretching likely originates from the high angular sensitivity of Kretschmann-like coupling of SPPs¹⁸⁷ on the pyramidal facets.

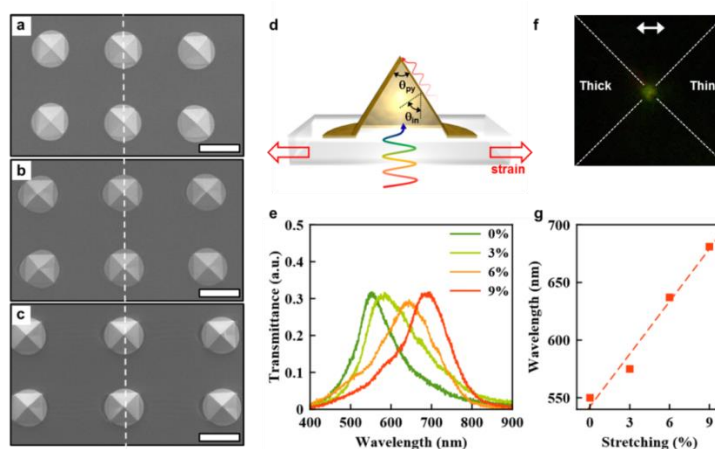


Figure 6.5 Tunable resonances of stretched metallic pyramids on PDMS. (a) The base width of the initial pyramid is 7 μm . (b) When the film is stretched to 10% of its initial length, the observed width increase of the pyramid's base is about 5%. (c) When stretched to 20%, a 10% increase in the pyramid base width is observed. Scale bar: (a)-(c) 10 μm . (d) Cross-sectional schematic illustrating SPPs being generated on the thin Au face of the pyramid. (e) The measured spectra of scattered light at the pyramidal tip. As the applied force increases, the peak position of the spectra red-shifts from 545 to 682 nm. (f) CCD image of an asymmetric pyramidal tip that is internally illuminated with a white light source. The approximate position of the pyramidal tip is represented by dotted white lines. Green light (545 nm) is observed from the tip for no strain. (g) Spectral tuning of the light scattering at the tip by changing the incident angle via applied strain. Figure is adapted from Yoo *et al.*¹⁸¹

6.4 Roller template stripping

Metal structures on PDMS films can be placed conformally on non-planar surfaces for various applications in optics, electronics, plasmonics, as well as metasurfaces. With template stripping, this transfer process can be made ever simpler and more controllable, because a cylindrical roller can be used to strip and transfer the patterned metal film onto a curved surface in a one-step rolling process, as illustrated in Figure 6.6. During the peel-off process, a sticky transferring layer is attached to the supporting substrate, which in this case is the curved surface of glass rod lens. Here, a Kapton® tape, a special type of polyimide, is used as the sticky transferring layer. By performing template stripping using a cylindrical roller, it is possible to control the bending angle of the flexible substrate (via the roller diameter) and the speed of template stripping (rolling speed) precisely. This technique can integrate both continuous and discontinuous patterned metal structures with curved

surfaces in a facile and controlled manner. For 3D metallic patterns such as pyramidal structures, a supporting layer like PDMS is needed to fill the void inside the pyramid. The sticky transferring layer starts integrating the metallic pyramids onto the curved surface as it is rolled up. On the other hand, 2D metallic patterns like nanohole array can be directly transferred onto the roller using only a sticky transfer layer (Kapton® tape) and no supporting layer (PDMS). Our process, shown in Figures 6.6a-b, can be used to transfer various metallic structures onto rollable substrates. In Figure 6.6c, arrays of 7 μm sized pyramids are transferred onto the curved surface of a 2 mm diameter glass rod using both a support and transfer layer. Furthermore, Figure 6.6d shows the nanohole patterns transferred onto a 10 mm diameter glass rod. The nanohole array with 500 nm periodicity and 200 nm hole size was separated into 500 μm by 500 μm square patterns prior to template stripping by photolithography and wet etching. To reduce stress in the metal film and prevent cracking, the size of each nanohole array is limited to a few hundred microns.

For roller template stripping of sub-micron-size patterns from a Si substrate, optical adhesive (NOA63, Norland Inc.) was used as a transfer layer instead of Kapton® tape to enhance adhesion for small metal structures (Figures 6.6e-f). A thin layer of partially cured NOA63 is flexible and can be wrapped around the glass rod lens. Using this approach, an array of gold disks (200 nm diameter) was successfully integrated on the glass surface of 1 mm radius using the optical epoxy supporting layer (Figure 6.6e). Metal wires (5 μm width) can also be transferred at various angles to the cylindrical axis of the rod lens (Figure 6.6f). In this case both the optical epoxy supporting and Kapton® tape transferring layers were used. In this technique, both bending angle and strip speed can be used as process parameters. Moreover, the type of supporting layer could be selected according to the structure to be transferred. Such controllability can facilitate successful integration of smooth patterned metallic structures onto curved surfaces. For example, plasmonic nanostructures could readily be integrated onto the curved surface of an optical fiber or microsphere resonator for sensing applications. Since metallic apertures, nanoparticles, tips, and wire grids are basic building blocks for metasurfaces,^{157, 158} our roller template stripping technique can provide a practical route for manufacturing large-area non-planar metasurfaces. For applications requiring large-area patterning beyond the standard wafer scale, such as transparent electrodes,¹⁸⁷ and flexible touch panels,¹⁵⁴ roller template stripping may be combined with roll-to-roll processing schemes to mass-produce continuous patterned metal foils or polymer films embedded with high-quality patterned metals.

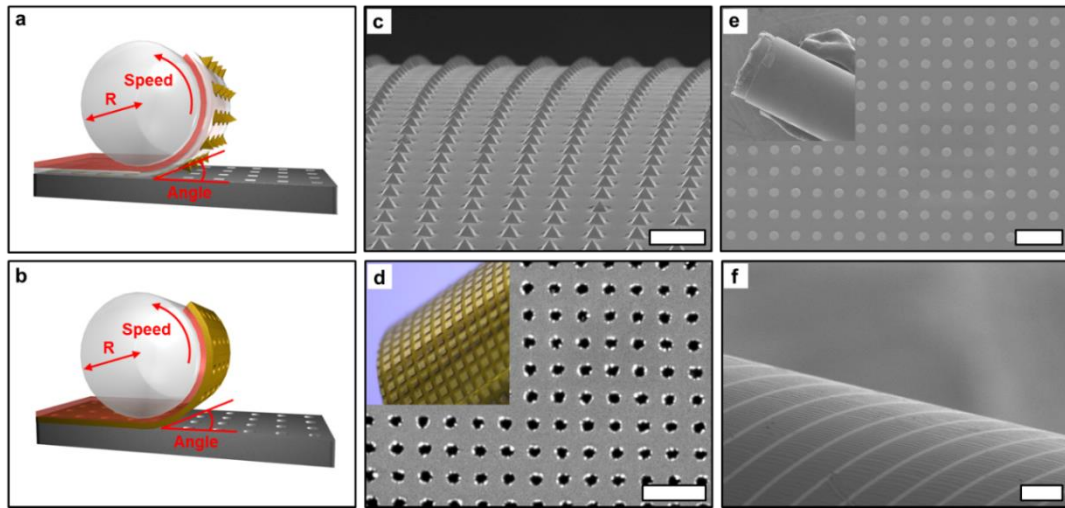


Figure 6.6 (a) Illustration of a roller template stripping process. Patterned metals on a silicon template are covered with a PDMS transfer layer (white) followed by a sticky double-sided Kapton tape (red). A glass rod lens is used as a rollable substrate to peel off patterned metals from the Si substrate and wrap them around its cylindrical surface. (b) Gold nanohole array films can be transferred using only a Kapton tape layer. (c) An array of $7\ \mu\text{m}$ sized pyramids was rolled onto the curved surface of a glass rod (2 mm in diameter). Scale bar: $20\ \mu\text{m}$. (d) Nanohole patterns transferred onto a glass rod with a 10 mm diameter. The nanohole array with a 500 nm period and a 200 nm hole size was separated into $200\ \mu\text{m}$ by $200\ \mu\text{m}$ square patterns via standard photolithography before transferring to the glass rod. Scale bar: $1\ \mu\text{m}$. (e) An array of Au disks (200 nm diameter) was integrated onto the surface of a 1 mm radius glass rod using an optical epoxy transfer layer. Scale bar: $1\ \mu\text{m}$. (f) An array of parallel Au wires ($5\ \mu\text{m}$ width) was transferred onto a glass rod (2 mm diameter) with optical epoxy and a Kapton tape transfer layer. Scale bar: $30\ \mu\text{m}$. Figure is adapted from Yoo *et al.*¹⁸¹

6.5 Conclusion

We have demonstrated a novel method of integrating plasmonic nanostructures such as Au nanohole arrays and pyramids with PDMS using template stripping allowing for mechanical tuning of the plasmonic properties of these nanostructures consisting of continuous metal films. Using our technique, it is possible to modulate the EOT spectra through nanohole arrays and the wavelength of light resonantly scattered at the tip of a gold pyramid. We took this approach one step further by demonstrating roller template stripping of metallic nanostructure onto cylindrical surface of a glass rod lens. This method can be combined with other cylindrical surfaces such as optical fibers, spherical surfaces such as microsphere resonators, or other structured surfaces to enable integration of plasmonic properties with light delivery mechanisms, and fabrication of optrodes, hyperlenses, non-planar metamaterials,^{188, 189} and cylindrical displays¹⁵⁵. Finally, nano-patterning on a cylindrical roller can be used for subsequent roll-to-roll nanoimprinting.^{190, 191}

Chapter 7

Conclusion and Future Directions

This chapter outlines engineering metallic nanogap aperture structure for enhancing optical transmission and resulting plasmonic device's application described in the previous chapters and presents future research directions of on-going projects along with primary data.

7.1 Dissertation overview and conclusions

This dissertation presented how metallic nanogap aperture can be engineered for enhancing optical transmission. Based on atomic layer lithography, turned into novel and efficient technique to fabricate sub-10-nm metallic nanogap aperture, we have improved current technique to achieve various metallic nanogap apertures which could never be realized via existing techniques. Resulting metallic nanogap apertures were investigated theoretically to figure out how they can enhance optical transmission through themselves. Afterward, novel application was proposed in this thesis.

First, extraordinary optical transmission via the coaxial nanogap aperture was explored. In this structure, enhanced mid-IR transmission was attributed to TE_{11} -plasmonic guided mode at a cutoff frequency. Furthermore, extremely strong field confinement into a single digit nanometer gap aperture could be taken into account by model epsilon-near-zero (ENZ) at a cutoff frequency. Coaxial nanogap aperture, a novel but challenging structure to fabricate, was successfully achieved using a combination of atomic layer lithography with glancing-angle ion polishing. ENZ properties such as supercoupling, independence of waveguide length, and uniform field distribution owing to infinite phase velocity were demonstrated experimentally and numerically.

Second, a single nanogap aperture was engineered by adding metallic sidewalls as reflecting mirrors to improve the resonance sharpness. T-shaped trench resonator gave rise to Fano-shaped resonance with high Q factor by suppressing optical leakage source using very narrow nanogap aperture. Interestingly, resulting Fano-resonance peaks were no longer governed by phase-matching condition unlike previous studies on T-shaped trench resonator. Such deviation could be interpreted by steep phase change near Fano-resonance. Moreover, we could demonstrate plasmon-induced transparency (PIT) by breaking symmetry of nanogap position, thereby allowing for the tunability of Fano-resonance in visible regime.

Third, trench nanogap resonator, separated into two wings isolated electrically, could act as a two-terminal device, which enables for a novel application like electrically-active plasmonic nanotweezer via dielectrophoretic force. In this structure, single nanogap aperture fabricated by atomic layer lithography was activated optically as well as electrically. In addition, the highly sensitive “hot spot” corresponds with where the strong electric field is generated. This structural merit benefits DEP-enhanced plasmonic biosensing. Therefore, trap and de-trap of nanometer-sized PS beads could be detected and monitored throughout refractive index sensing under very low voltage (<1V). Ultimately, DEP-enhanced plasmonic sensing was demonstrated to overcome the diffusion transport limit. It excellently performed sensing of biomolecule with 10 pM with 100 times faster than diffusion-based transportation.

Lastly, various plasmonic metallic nanostructures such as nanohole array and pyramid were engineered by transferring conventional Si substrate into stretchable substrate using template-stripping. It allowed for plasmonic resonance to be manipulated via mechanical stretching of substrate. Furthermore, roller-based template-stripping enabled metallic nanostructure to be integrated onto 3D substrate like cylindrical lens. This novel approach opened up a door to manufacture 3D plasmonic or metamaterial devices beyond simple 2D structures.

Throughout this dissertation, novel nanogap metallic apertures were carefully designed and fabricated using atomic layer lithography. Such technical progress enabled us to explore physical phenomena of interest and to improve (or engineer or optimize) their optical properties.

7.2 Future directions

Metallic nanogap apertures presented in this dissertation can be harnessed for applications to require strong interaction of light with matter, because it is capable for confining light into nanometric volume, leading to extremely strong field enhancement inside the nanogap. Therefore, the integration of active materials with our metallic nanogap aperture would benefit many applications for light-matter interaction.

7.2.1 Nanogap-enhanced infrared absorption

The use of metallic structure capable of supporting SPPs or localized resonances for sensing in the mid-IR^{18, 22, 103} has clearly shown promise. However, unlike SPR-based surface sensing in visible frequency, which have been widely adopted as standard laboratory techniques or even commercial systems, mid-IR plasmonic-based sensing has not been broadly adopted outside the research lab in spite of frequency of interest where most molecular absorptions take place. This may be due to the large mode volume and weak confinement of light at mid-IR frequency, which limits the interaction of light with molecules of interest. For this reason, there has been significant interest in developing plasmonic structures capable of confining mid-IR light to ultra-small mode volumes.^{24, 28, 102} In this thesis, we successfully fabricated coaxial aperture array with micrometer-scale perimeter and nanometer-scale gap.⁷¹ Successful integration of micrometer-scale patterns with nanometer-scale gap allows for nanoscale confinement of light with long wavelength, thus leading to greatly enhanced transmission from near infrared to mid infrared by controlling a diameter of coaxial nanogap aperture and a width of nanogap. The ability to confine mid-IR light to nanoscale volumes has the potential to enhance the interaction between incident light and molecules. Therefore, gap-enhanced infrared absorption will be explored in the future research.

Figure 7.1a shows IR absorption spectroscopy of thin PMMA layer enhanced via coaxial nanogap aperture. Here, coaxial nanogap aperture arrays with 250 nm in diameter and 10 nm in gap size were spin-coated with 100 nm thick PMMA layer (2% diluted PMMA). Symmetric and asymmetric vibrations of C-H bond around 3000 wavenumber (1/cm) was amplified by strong electric field inside the coaxial nanogap, thus leading to huge absorption dips as shown in Figure 7.1a. This primary data manifests coaxial nanogap aperture as a great platform for surface-enhanced IR absorption (SEIRA). Furthermore, a new technique introduced in this dissertation, combination of atomic layer lithography and glancing-angle ion polishing, allows for more complicated coaxial nanogap aperture such as multiple concentric nanogap rings in Figure 7.1b. In multiple concentric

nanogap rings, each ring has specific resonance frequency. Therefore, broadband enhanced transmission would be achieved through multiple concentric nanogap rings structure. It would be very useful for detection of multiple absorption bands at the same time. However, coaxial nanogap array with high pattern density may affect the field enhancement because all nanogap apertures should share the finite intensity of incoming light. Thus, we need to design this device carefully using numerical modeling.

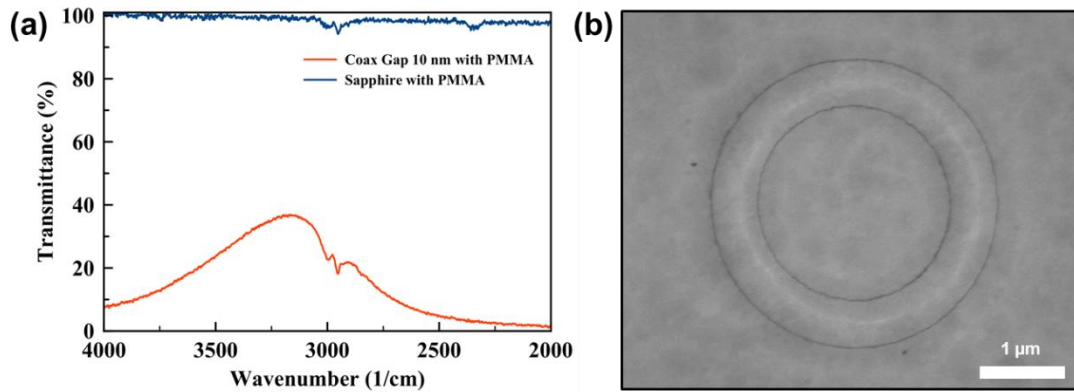


Figure 7.1 Gap-enhanced IR absorption spectroscopy. (a) IR absorption spectroscopy of thin PMMA layer enhanced via coaxial nanogap aperture. (b) Multiple concentric coaxial nanogap apertures for broadband IR absorption spectroscopy.

7.2.2 VO₂-incorporated coaxial nanogap apertures

Vanadium oxide (VO₂) is an inorganic compound exhibiting phase transition from insulator to metal at transition temperature (T_c) = 74 C°. ¹⁹² At temperature below T_c , VO₂ is a monoclinic crystal structure with distorted shorter distances between pairs of V atoms indicating metal-metal bonding. So, it exhibits insulator-like optical property in infrared frequency. At temperature above T_c , however, VO₂ is transformed to rutile crystal structure with undistorted long distance of V atoms by breaking metal-metal bonding, causing an increase in electrical conductivity like metal. ¹⁹³ Such interesting optical and electrical property has attracted much attention from photonics and electronics communities with many applications such as phase change memories ¹⁹⁴ for information storage, and optical switches. ^{195, 196} For the modulation applications, the transition should occur within a short range of temperature. However, the insulator-to-metal transition occurs gradually as temperature increases from 25 C° to 74 C°. To overcome a slow transition rate, various plasmonic structures have been combined with VO₂.

In metallic coaxial nanogap aperture, the gap is very sensitive to the variation in refractive index of material inside the gap due to strong field enhancement. Therefore, the incorporation of VO₂ into our metallic coaxial nanogap structure as a dielectric medium would be very useful for detecting the structural transition of VO₂, thus enabling to reduce the effective transition temperature for optical modulation. We employed ALD technique to incorporate VO₂ thin film into coaxial nanogap structure because our atomic layer lithography turns ALD thin-film into vertically-oriented nanogap. That is, VO₂ grown by ALD technique is compatible with our approach to fabricate metallic nanogap structure. Figure 7.2 shows the reflection spectra measured from VO₂-incorporated coaxial nanogap aperture array using FTIR with increasing temperature from below T_c to above T_c . Here two different VO₂ gap sizes like 13 nm and 17 nm were implemented in coaxial nanogap array shown in Figure 7.2 c-d. At room temperature, VO₂-incorporated coaxial nanogap arrays have cutoff resonances according to diameters of coaxial aperture because VO₂ acts as dielectric at room temperature. Bulk or micrometer-thick VO₂ layers above T_c have been known to be transformed into metallic status without any transparency in infrared. Therefore, we expected no reflection dips were observed in this experiment after heating above T_c . When heating the devices above T_c , however, reflection dips did not disappear. Instead, it decreases along with redshift. Thicker VO₂ coaxial nanogap arrays experience more reduction in reflection dip with further redshift. To my knowledge, optical property of such very thin VO₂ film has not been investigated many times. So, we need more experimental sets to figure out the results. But we think

that this result is logically valid because even metal below 20 nm thickness is not opaque in infrared due to thinner thickness than skin depth of light. Thus, we are on the way to fabricating 30-nm-thick VO₂ coaxial nanogap array and to measuring the transmission by increasing temperature.

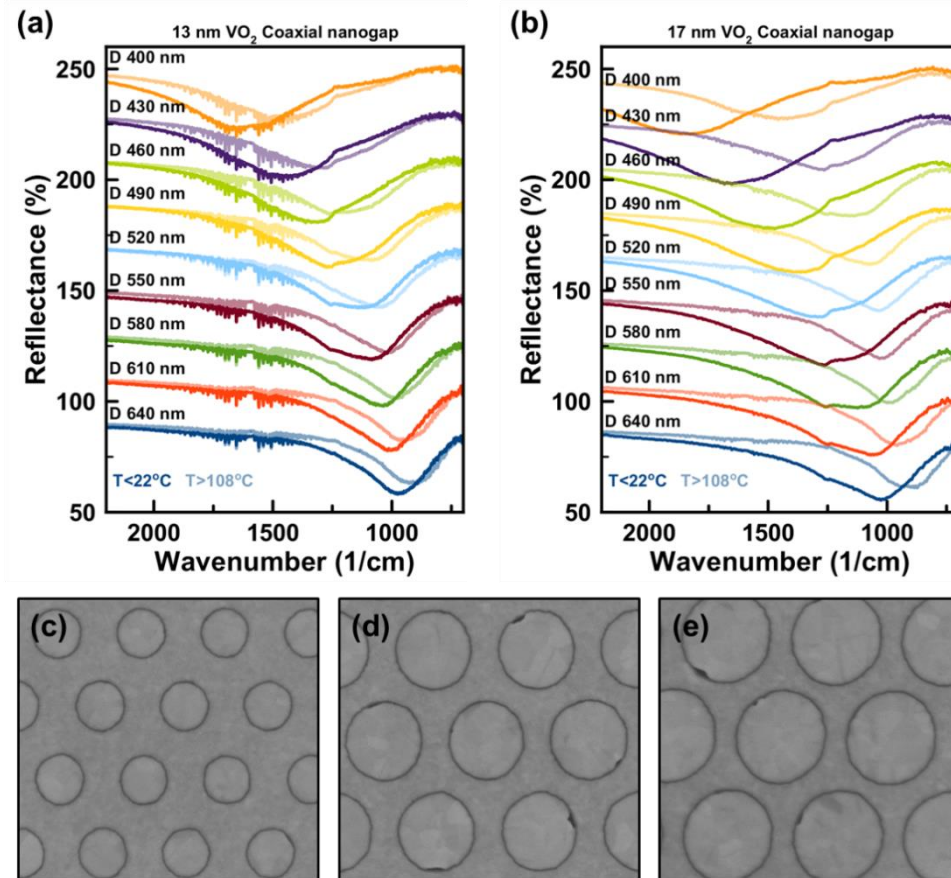


Figure 7.2 VO₂-incorporated coaxial nanogap apertures. (a) and (b) Reflection spectra measured using FTIR by increasing temperature from coaxial nanogap apertures with VO₂ of 13 nm and 17 nm, respectively. (c), (d), (e) SEM images corresponding to VO₂-filled coaxial nanogap array with a diameter 460 nm, 550 nm, 640 nm, respectively.

Bibliography

1. T. W. Ebbesen, H. J. Lezec, H. F. Ghaemi, T. Thio, P. A. Wolff. Extraordinary optical transmission through sub-wavelength hole arrays. *Nature* **1998**, 391, (6668), 667-669.
2. H. F. Ghaemi, T. Thio, D. E. Grupp, T. W. Ebbesen, H. J. Lezec. Surface plasmons enhance optical transmission through subwavelength holes. *Phys Rev B* **1998**, 58, (11), 6779-6782.
3. A. Krishnan, T. Thio, T. J. Kima, H. J. Lezec, T. W. Ebbesen, P. A. Wolff, J. Pendry, L. Martin-Moreno, F. J. Garcia-Vidal. Evanescently coupled resonance in surface plasmon enhanced transmission. *Opt Commun* **2001**, 200, (1-6), 1-7.
4. L. Martin-Moreno, F. J. Garcia-Vidal, H. J. Lezec, K. M. Pellerin, T. Thio, J. B. Pendry, T. W. Ebbesen. Theory of extraordinary optical transmission through subwavelength hole arrays. *Phys Rev Lett* **2001**, 86, (6), 1114-1117.
5. J. Homola, S. S. Yee, G. Gauglitz. Surface plasmon resonance sensors: review. *Sensor Actuat B-Chem* **1999**, 54, (1-2), 3-15.
6. D. E. Grupp, H. J. Lezec, T. Thio, T. W. Ebbesen. Beyond the Bethe limit: Tunable enhanced light transmission through a single sub-wavelength aperture. *Adv Mater* **1999**, 11, (10), 860-862.
7. H. J. Lezec, A. Degiron, E. Devaux, R. A. Linke, L. Martin-Moreno, F. J. Garcia-Vidal, T. W. Ebbesen. Beaming light from a subwavelength aperture. *Science* **2002**, 297, (5582), 820-822.
8. A. Bouhelier, J. Renger, M. R. Beversluis, L. Novotny. Plasmon-coupled tip-enhanced near-field optical microscopy. *J Microsc-Oxford* **2003**, 210, 220-224.
9. A. Bouhelier, M. Beversluis, A. Hartschuh, L. Novotny. Near-field second-harmonic generation induced by local field enhancement. *Phys Rev Lett* **2003**, 90, (1).
10. E. Verhagen, L. Kuipers, A. Polman. Enhanced nonlinear optical effects with a tapered plasmonic waveguide. *Nano Lett* **2007**, 7, (2), 334-337.
11. M. I. Stockman. Nanofocusing of optical energy in tapered plasmonic waveguides. *Phys Rev Lett* **2004**, 93, (13).
12. N. A. Janunts, K. S. Baghdasaryan, K. V. Nerkararyan, B. Hecht. Excitation and superfocusing of surface plasmon polaritons on a silver-coated optical fiber tip. *Opt Commun* **2005**, 253, (1-3), 118-124.
13. E. Verhagen, A. Polman, L. Kuipers. Nanofocusing in laterally tapered plasmonic waveguides. *Opt Express* **2008**, 16, (1), 45-57.
14. H. T. Miyazaki, Y. Kurokawa. Squeezing visible light waves into a 3-nm-thick and 55-nm-long plasmon cavity. *Phys Rev Lett* **2006**, 96, (9).
15. D. R. Ward, F. Huser, F. Pauly, J. C. Cuevas, D. Natelson. Optical rectification and field enhancement in a plasmonic nanogap. *Nat Nanotechnol* **2010**, 5, (10), 732-736.
16. J. A. Schuller, E. S. Barnard, W. S. Cai, Y. C. Jun, J. S. White, M. L. Brongersma. Plasmonics for extreme light concentration and manipulation (vol 9, pg 193, 2010). *Nat Mater* **2010**, 9, (4).
17. A. M. Michaels, J. Jiang, L. Brus. Ag nanocrystal junctions as the site for surface-enhanced Raman scattering of single Rhodamine 6G molecules. *J Phys Chem B* **2000**, 104, (50), 11965-11971.

18. X. S. Chen, C. Ciraci, D. R. Smith, S. H. Oh. Nanogap-Enhanced Infrared Spectroscopy with Template-Stripped Wafer-Scale Arrays of Buried Plasmonic Cavities. *Nano Lett* **2015**, 15, (1), 107-113.
19. R. A. Shelby, D. R. Smith, S. Schultz. Experimental verification of a negative index of refraction. *Science* **2001**, 292, (5514), 77-79.
20. V. M. Shalaev. Optical negative-index metamaterials. *Nat Photonics* **2007**, 1, (1), 41-48.
21. S. Aksu, A. A. Yanik, R. Adato, A. Artar, M. Huang, H. Altug. High-Throughput Nanofabrication of Infrared Plasmonic Nanoantenna Arrays for Vibrational Nanospectroscopy. *Nano Lett* **2010**, 10, (7), 2511-2518.
22. R. Adato, A. A. Yanik, J. J. Amsden, D. L. Kaplan, F. G. Omenetto, M. K. Hong, S. Erramilli, H. Altug. Ultra-sensitive vibrational spectroscopy of protein monolayers with plasmonic nanoantenna arrays. *P Natl Acad Sci USA* **2009**, 106, (46), 19227-19232.
23. J. Melngailis. Focused Ion-Beam Technology and Applications. *J Vac Sci Technol B* **1987**, 5, (2), 469-495.
24. R. M. Langford, P. M. Nellen, J. Gierak, Y. Q. Fu. Focused ion beam micro- and nanoengineering. *Mrs Bull* **2007**, 32, (5), 417-423.
25. N. C. Lindquist, P. Nagpal, K. M. McPeak, D. J. Norris, S. H. Oh. Engineering metallic nanostructures for plasmonics and nanophotonics. *Rep Prog Phys* **2012**, 75, (3).
26. C. Vieu, F. Carcenac, A. Pepin, Y. Chen, M. Mejias, A. Lebib, L. Manin-Ferlazzo, L. Couraud, H. Launois. Electron beam lithography: resolution limits and applications. *Appl Surf Sci* **2000**, 164, 111-117.
27. S. Y. Chou, P. R. Krauss, P. J. Renstrom. Imprint lithography with 25-nanometer resolution. *Science* **1996**, 272, (5258), 85-87.
28. P. Nagpal, N. C. Lindquist, S. H. Oh, D. J. Norris. Ultrasoft Patterned Metals for Plasmonics and Metamaterials. *Science* **2009**, 325, (5940), 594-597.
29. M. T. Bohr, R. S. Chau, T. Ghani, K. Mistry. The high-k solution. *Ieee Spectrum* **2007**, 44, (10), 29-35.
30. M. Leskela, M. Ritala. Atomic layer deposition chemistry: Recent developments and future challenges. *Angew Chem Int Edit* **2003**, 42, (45), 5548-5554.
31. H. Im, K. C. Bantz, N. C. Lindquist, C. L. Haynes, S. H. Oh. Vertically Oriented Sub-10-nm Plasmonic Nanogap Arrays. *Nano Lett* **2010**, 10, (6), 2231-2236.
32. X. S. Chen, H. R. Park, M. Pelton, X. J. Piao, N. C. Lindquist, H. Im, Y. J. Kim, J. S. Ahn, K. J. Ahn, N. Park, D. S. Kim, S. H. Oh. Atomic layer lithography of wafer-scale nanogap arrays for extreme confinement of electromagnetic waves. *Nat Commun* **2013**, 4.
33. H. R. Park, X. S. Chen, N. C. Nguyen, J. Peraire, S. H. Oh. Nanogap-Enhanced Terahertz Sensing of 1 nm Thick ($\lambda/10(6)$) Dielectric Films. *Acs Photonics* **2015**, 2, (3), 417-424.
34. R. H. Ritchie. Plasma Losses by Fast Electrons in Thin Films. *American Physical Society* **1957**, 106, (6).
35. H. Raether. Surface-Plasmons on Smooth and Rough Surfaces and on Gratings. *Springer Tr Mod Phys* **1988**, 111, 1-133.
36. W. L. Barnes, A. Dereux, T. W. Ebbesen. Surface plasmon subwavelength optics. *Nature* **2003**, 424, (6950), 824-30.
37. Erwin Kretschmann. Die Bestimmung optischer Konstanten von Metallen durch Anregung von Oberflächenplasmaschwingungen. *Zeitschrift für Physik* **1971**, 241, (4).
38. R. Zia, M. D. Selker, P. B. Catrysse, M. L. Brongersma. Geometries and materials for subwavelength surface plasmon modes. *J Opt Soc Am A* **2004**, 21, (12), 2442-2446.
39. Stefan A. Maier, *Plasmonics : fundamentals and applications*. 1st, (Springer, 2007).

40. Tetsuro Kobayashi Junichi Takahara. Low-Dimensional Optical Waves And Nano-Optical Circuits. *optics and Photnics News* **2004**, 15, (10), 54.
41. H. X. Xu, E. J. Bjerneld, M. Kall, L. Borjesson. Spectroscopy of single hemoglobin molecules by surface enhanced Raman scattering. *Phys Rev Lett* **1999**, 83, (21), 4357-4360.
42. H. A. Bethe. Theory of diffraction by small holes. *Physical Review* **1944**, 66, 163.
43. K. J. K. Koerkamp, S. Enoch, F. B. Segerink, N. F. van Hulst, L. Kuipers. Strong influence of hole shape on extraordinary transmission through periodic arrays of subwavelength holes. *Phys Rev Lett* **2004**, 92, (18).
44. R. Gordon, A. G. Brolo, A. McKinnon, A. Rajora, B. Leathem, K. L. Kavanagh. Strong polarization in the optical transmission through elliptical nanohole arrays. *Phys Rev Lett* **2004**, 92, (3).
45. A. Degiron, T. W. Ebbesen. The role of localized surface plasmon modes in the enhanced transmission of periodic subwavelength apertures. *J Opt a-Pure Appl Op* **2005**, 7, (2), S90-S96.
46. A. Degiron, H. J. Lezec, N. Yamamoto, T. W. Ebbesen. Optical transmission properties of a single subwavelength aperture in a real metal. *Opt Commun* **2004**, 239, (1-3), 61-66.
47. C. Genet, T. W. Ebbesen. Light in tiny holes. *Nature* **2007**, 445, (7123), 39-46.
48. H. T. Liu, P. Lalanne. Microscopic theory of the extraordinary optical transmission. *Nature* **2008**, 452, (7188), 728-731.
49. L. Rayleigh. Note on the remarkable case of diffraction spectra described by prof. wood. *Philosophical magazine* **1907**, 14.
50. U. Fano. The Theory of Anomalous Diffraction Gratings and of Quasi-Stationary Waves on Metallic Surfaces (Sommerfeld' waves). *Journal of the Optical Society of America* **1941**, 31, (3).
51. U. Fano. Citation Classics - Effects of Configuration Interaction on Intensities and Phase-Shifts. *Curr Contents* **1977**, (27), 8-8.
52. M. Sarrazin, J. P. Vigneron, J. M. Vigoureux. Role of Wood anomalies in optical properties of thin metallic films with a bidimensional array of subwavelength holes. *Phys Rev B* **2003**, 67, (8).
53. C. Genet, M. P. van Exter, J. P. Woerdman. Fano-type interpretation of red shifts and red tails in hole array transmission spectra. *Opt Commun* **2003**, 225, (4-6), 331-336.
54. F. I. Baida, D. Van Labeke. Light transmission by subwavelength annular aperture arrays in metallic films. *Opt Commun* **2002**, 209, (1-3), 17-22.
55. F. I. Baida, D. Van Labeke. Three-dimensional structures for enhanced transmission through a metallic film: Annular aperture arrays. *Phys Rev B* **2003**, 67, (15).
56. F. I. Baida. Enhanced transmission through subwavelength metallic coaxial apertures by excitation of the TEM mode. *Appl Phys B-Lasers O* **2007**, 89, (2-3), 145-149.
57. F. I. Baida, A. Belkhir, D. Van Labeke, O. Lamrous. Subwavelength metallic coaxial waveguides in the optical range: Role of the plasmonic modes. *Phys Rev B* **2006**, 74, (20).
58. M. I. Haftel, C. Schlockermann, G. Blumberg. Enhanced transmission with coaxial nanoapertures: Role of cylindrical surface plasmons. *Phys Rev B* **2006**, 74, (23).
59. F. I.; Salvi Baida, J., *Enhanced Optical Transmission Through Annular Aperture Arrays: Role of the Plasmonic Guided Modes*. 1, 239-268 (Springer-Verlag New York, 2010).
60. M. Silveirinha, N. Engheta. Tunneling of electromagnetic energy through subwavelength channels and bends using epsilon-near-zero materials. *Phys Rev Lett* **2006**, 97, (15).
61. A. Alu, M. G. Silveirinha, A. Salandrino, N. Engheta. Epsilon-near-zero metamaterials and electromagnetic sources: Tailoring the radiation phase pattern. *Phys Rev B* **2007**, 75, (15).
62. N. Engheta. Pursuing Near-Zero Response. *Science* **2013**, 340, (6130), 286-287.

63. E. Feigenbaum, K. Diest, H. A. Atwater. Unity-Order Index Change in Transparent Conducting Oxides at Visible Frequencies. *Nano Lett* **2010**, 10, (6), 2111-2116.
64. A. P. Vasudev, J. H. Kang, J. Park, X. G. Liu, M. L. Brongersma. Electro-optical modulation of a silicon waveguide with an "epsilon-near-zero" material. *Opt Express* **2013**, 21, (22), 26387-26397.
65. J. A. Dionne, K. Diest, L. A. Sweatlock, H. A. Atwater. PlasMOSstor: A Metal-Oxide-Si Field Effect Plasmonic Modulator. *Nano Lett* **2009**, 9, (2), 897-902.
66. H. W. Lee, G. Papadakis, S. P. Burgos, K. Chander, A. Kriesch, R. Pala, U. Peschel, H. A. Atwater. Nanoscale Conducting Oxide PlasMOSstor. *Nano Lett* **2014**, 14, (11), 6463-6468.
67. M. Z. Alam, I. De Leon, R. W. Boyd. Large optical nonlinearity of indium tin oxide in its epsilon-near-zero region. *Science* **2016**, 352, (6287), 795-797.
68. R. Maas, J. Parsons, N. Engheta, A. Polman. Experimental realization of an epsilon-near-zero metamaterial at visible wavelengths. *Nat Photonics* **2013**, 7, (11), 907-912.
69. J. Gao, L. Sun, H. X. Deng, C. J. Mathai, S. Gangopadhyay, X. D. Yang. Experimental realization of epsilon-near-zero metamaterial slabs with metal-dielectric multilayers. *Appl Phys Lett* **2013**, 103, (5).
70. A. Alu, N. Engheta. Light squeezing through arbitrarily shaped plasmonic channels and sharp bends. *Phys Rev B* **2008**, 78, (3).
71. D. Yoo, N. C. Nguyen, L. Martin-Moreno, D. A. Mohr, S. Carretero-Palacios, J. Shaver, J. Peraire, T. W. Ebbesen, S. H. Oh. High-Throughput Fabrication of Resonant Metamaterials with Ultrasmall Coaxial Apertures via Atomic Layer Lithography. *Nano Lett* **2016**, 16, (3), 2040-2046.
72. A. G. Brolo, E. Arctander, R. Gordon, B. Leathem, K. L. Kavanagh. Nanohole-enhanced Raman scattering. *Nano Lett* **2004**, 4, (10), 2015-2018.
73. S. I. Bozhevolnyi, V. S. Volkov, E. Devaux, J. Y. Laluet, T. W. Ebbesen. Channel plasmon subwavelength waveguide components including interferometers and ring resonators. *Nature* **2006**, 440, (7083), 508-511.
74. N. J. Halas. Plasmonics: An Emerging Field Fostered by Nano Letters. *Nano Lett* **2010**, 10, (10), 3816-3822.
75. S. M. Orbons, A. Roberts. Resonance and extraordinary transmission in annular aperture arrays. *Opt Express* **2006**, 14, (26), 12623-12628.
76. P. B. Catrysse, S. H. Fan. Understanding the dispersion of coaxial plasmonic structures through a connection with the planar metal-insulator-metal geometry. *Appl Phys Lett* **2009**, 94, (23).
77. R. de Waele, S. P. Burgos, A. Polman, H. A. Atwater. Plasmon Dispersion in Coaxial Waveguides from Single-Cavity Optical Transmission Measurements. *Nano Lett* **2009**, 9, (8), 2832-2837.
78. F. J. Garcia-Vidal, L. Martin-Moreno, T. W. Ebbesen, L. Kuipers. Light passing through subwavelength apertures. *Rev Mod Phys* **2010**, 82, (1), 729-787.
79. M. G. Silveirinha, N. Engheta. Theory of supercoupling, squeezing wave energy, and field confinement in narrow channels and tight bends using epsilon near-zero metamaterials. *Phys Rev B* **2007**, 76, (24).
80. W. Fan, S. Zhang, N. C. Panoiu, A. Abdenour, S. Krishna, R. M. Osgood, K. J. Malloy, S. R. J. Brueck. Second harmonic generation from a nanopatterned isotropic nonlinear material. *Nano Lett* **2006**, 6, (5), 1027-1030.
81. C. Argyropoulos, P. Y. Chen, G. D'Aguanno, N. Engheta, A. Alu. Boosting optical nonlinearities in epsilon-near-zero plasmonic channels. *Phys Rev B* **2012**, 85, (4).
82. S. P. Burgos, R. de Waele, A. Polman, H. A. Atwater. A single-layer wide-angle negative-index metamaterial at visible frequencies. *Nat Mater* **2010**, 9, (5), 407-412.

83. M. A. van de Haar, R. Maas, H. Schokker, A. Polman. Experimental Realization of a Polarization-Independent Ultraviolet/Visible Coaxial Plasmonic Metamaterial. *Nano Lett* **2014**, 14, (11), 6356-6360.
84. K. L. Tsakmakidis, A. D. Boardman, O. Hess. 'Trapped rainbow' storage of light in metamaterials. *Nature* **2007**, 450, (7168), 397-401.
85. H. A. Atwater, A. Polman. Plasmonics for improved photovoltaic devices. *Nat Mater* **2010**, 9, (10), 865-865.
86. M. Khajavikhan, A. Simic, M. Katz, J. H. Lee, B. Slutsky, A. Mizrahi, V. Lomakin, Y. Fainman. Thresholdless nanoscale coaxial lasers. *Nature* **2012**, 482, (7384), 204-207.
87. A. A. E. Saleh, J. A. Dionne. Toward Efficient Optical Trapping of Sub-10-nm Particles with Coaxial Plasmonic Apertures. *Nano Lett* **2012**, 12, (11), 5581-5586.
88. A. Alu, N. Engheta. Boosting Molecular Fluorescence with a Plasmonic Nanolauncher. *Phys Rev Lett* **2009**, 103, (4).
89. M. Melli, A. Polyakov, D. Gargas, C. Huynh, L. Scipioni, W. Bao, D. F. Ogletree, P. J. Schuck, S. Cabrini, A. Weber-Bargioni. Reaching the Theoretical Resonance Quality Factor Limit in Coaxial Plasmonic Nanoresonators Fabricated by Helium Ion Lithography. *Nano Lett* **2013**, 13, (6), 2687-2691.
90. W. J. Fan, S. Zhang, B. Minhas, K. J. Malloy, S. R. J. Brueck. Enhanced infrared transmission through subwavelength coaxial metallic arrays. *Phys Rev Lett* **2005**, 94, (3).
91. W. J. Fan, S. Zhang, K. J. Malloy, S. R. J. Brueck. Enhanced mid-infrared transmission through nanoscale metallic coaxial-aperture arrays. *Opt Express* **2005**, 13, (12), 4406-4413.
92. S. M. George. Atomic Layer Deposition: An Overview. *Chem Rev* **2010**, 110, (1), 111-131.
93. J. A. Hutchison, D. M. O'Carroll, T. Schwartz, C. Genet, T. W. Ebbesen. Absorption-Induced Transparency. *Angew Chem Int Edit* **2011**, 50, (9), 2085-2089.
94. S. Carretero-Palacios, F. J. Garcia-Vidal, L. Martin-Moreno, S. G. Rodrigo. Effect of film thickness and dielectric environment on optical transmission through subwavelength holes. *Phys Rev B* **2012**, 85, (3).
95. M. J. Lockyear, A. P. Hibbins, J. R. Sambles, C. R. Lawrence. Microwave transmission through a single subwavelength annular aperture in a metal plate. *Phys Rev Lett* **2005**, 94, (19).
96. J. Lambe, S. L. Mccarthy. Light-Emission from Inelastic Electron-Tunneling. *Phys Rev Lett* **1976**, 37, (14), 923-925.
97. R. Esteban, A. G. Borisov, P. Nordlander, J. Aizpurua. Bridging quantum and classical plasmonics with a quantum-corrected model. *Nat Commun* **2012**, 3.
98. D. C. Marinica, M. Zapata, P. Nordlander, A. K. Kazansky, M. Echenique, P. J. Aizpurua, A. G. Borisov. Active quantum plasmonics. *Science advances* **2015**, 1, (11), e1501095.
99. M. Parzefall, P. Bharadwaj, A. Jain, T. Taniguchi, K. Watanabe, L. Novotny. Antenna-coupled photon emission from hexagonal boron nitride tunnel junctions. *Nat Nanotechnol* **2015**, 10, (12), 1058-1063.
100. S. Lal, S. Link, N. J. Halas. Nano-optics from sensing to waveguiding. *Nat Photonics* **2007**, 1, (11), 641-648.
101. R. Gordon, D. Sinton, K. L. Kavanagh, A. G. Brolo. A new generation of sensors based on extraordinary optical transmission. *Accounts Chem Res* **2008**, 41, (8), 1049-1057.
102. D. R. Ward, N. K. Grady, C. S. Levin, N. J. Halas, Y. P. Wu, P. Nordlander, D. Natelson. Electromigrated nanoscale gaps for surface-enhanced Raman spectroscopy. *Nano Lett* **2007**, 7, (5), 1396-1400.

103. L. V. Brown, K. Zhao, N. King, H. Sobhani, P. Nordlander, N. J. Halas. Surface-Enhanced Infrared Absorption Using Individual Cross Antennas Tailored to Chemical Moieties. *J Am Chem Soc* **2013**, 135, (9), 3688-3695.
104. Y. J. Pang, R. Gordon. Optical Trapping of a Single Protein. *Nano Lett* **2012**, 12, (1), 402-406.
105. M. Kauranen, A. V. Zayats. Nonlinear plasmonics. *Nat Photonics* **2012**, 6, (11), 737-748.
106. J. B. Lassiter, X. S. Chen, X. J. Liu, C. Ciraci, T. B. Hoang, S. Larouche, S. H. Oh, M. H. Mikkelsen, D. R. Smith. Third-Harmonic Generation Enhancement by Film-Coupled Plasmonic Stripe Resonators. *Acs Photonics* **2014**, 1, (11), 1212-1217.
107. J. L. Jewell, S. L. McCall, Y. H. Lee, A. Scherer, A. C. Gossard, J. H. English. Lasing Characteristics of GaAs Microresonators. *Appl Phys Lett* **1989**, 54, (15), 1400-1402.
108. J. M. Gerard, D. Barrier, J. Y. Marzin, R. Kuszelewicz, L. Manin, E. Costard, V. Thierry-Mieg, T. Rivera. Quantum boxes as active probes for photonic microstructures: The pillar microcavity case. *Appl Phys Lett* **1996**, 69, (4), 449-451.
109. G. S. Solomon, M. Pelton, Y. Yamamoto. Modification of spontaneous emission of a single quantum dot. *Phys Status Solidi A* **2000**, 178, (1), 341-344.
110. D. K. Armani, T. J. Kippenberg, S. M. Spillane, K. J. Vahala. Ultra-high-Q toroid microcavity on a chip. *Nature* **2003**, 421, (6926), 925-928.
111. O. Painter, R. K. Lee, A. Scherer, A. Yariv, J. D. O'Brien, P. D. Dapkus, I. Kim. Two-dimensional photonic band-gap defect mode laser. *Science* **1999**, 284, (5421), 1819-1821.
112. V. J. Sorger, R. F. Oulton, J. Yao, G. Bartal, X. Zhang. Plasmonic Fabry-Perot Nanocavity. *Nano Lett* **2009**, 9, (10), 3489-3493.
113. R. Hillenbrand, T. Taubner, F. Keilmann. Phonon-enhanced light-matter interaction at the nanometre scale. *Nature* **2002**, 418, (6894), 159-162.
114. T. Baba, D. Sano. Low-threshold lasing and Purcell effect in microdisk lasers at room temperature. *Ieee J Sel Top Quant* **2003**, 9, (5), 1340-1346.
115. D. J. Bergman, M. I. Stockman. Surface plasmon amplification by stimulated emission of radiation: Quantum generation of coherent surface plasmons in nanosystems. *Phys Rev Lett* **2003**, 90, (2).
116. E. Moreno, S. G. Rodrigo, S. I. Bozhevolnyi, L. Martin-Moreno, F. J. Garcia-Vidal. Guiding and focusing of electromagnetic fields with wedge plasmon polaritons. *Phys Rev Lett* **2008**, 100, (2).
117. S. J. P. Kress, F. V. Antolinez, P. Richner, S. V. Jayanti, D. K. Kim, F. Prins, A. Riedinger, M. P. C. Fischer, S. Meyer, K. M. McPeak, D. Poulidakos, D. J. Norris. Wedge Waveguides and Resonators for Quantum Plasmonics. *Nano Lett* **2015**, 15, (9), 6267-6275.
118. H. Ditlbacher, A. Hohenau, D. Wagner, U. Kreibig, M. Rogers, F. Hofer, F. R. Aussenegg, J. R. Krenn. Silver nanowires as surface plasmon resonators. *Phys Rev Lett* **2005**, 95, (25).
119. B. Wild, L. N. Cao, Y. G. Sun, B. P. Khanal, E. R. Zubarev, S. K. Gray, N. F. Scherer, M. Pelton. Propagation Lengths and Group Velocities of Plasmons in Chemically Synthesized Gold and Silver Nanowires. *Acs Nano* **2012**, 6, (1), 472-482.
120. B. K. Min, E. Ostby, V. Sorger, E. Ulin-Avila, L. Yang, X. Zhang, K. Vahala. High-Q surface-plasmon-polariton whispering-gallery microcavity. *Nature* **2009**, 457, (7228), 455-U3.
121. S. H. Kwon. Deep subwavelength plasmonic whispering-gallery-mode cavity. *Opt Express* **2012**, 20, (22), 24918-24924.
122. B. Luk'yanchuk, N. I. Zheludev, S. A. Maier, N. J. Halas, P. Nordlander, H. Giessen, C. T. Chong. The Fano resonance in plasmonic nanostructures and metamaterials. *Nat Mater* **2010**, 9, (9), 707-715.
123. A. E. Miroschnichenko, S. Flach, Y. S. Kivshar. Fano resonances in nanoscale structures. *Rev Mod Phys* **2010**, 82, (3), 2257-2298.

124. Stephen A. O. Olson, Daniel A. Mohr, Jonah Shaver, Timothy W. Johnson, and Sang-Hyun Oh. Plasmonic Cup Resonators for Single-Nanohole-Based Sensing and Spectroscopy. *Acs Photonics* **2016**, 3, (7), 1202-1207.
125. Q. Min, R. Gordon. Surface plasmon microcavity for resonant transmission through a slit in a gold film. *Opt Express* **2008**, 16, (13), 9708-9713.
126. J. J. Chen, Z. Li, S. Yue, J. H. Xiao, Q. H. Gong. Plasmon-Induced Transparency in Asymmetric T-Shape Single Slit. *Nano Lett* **2012**, 12, (5), 2494-2498.
127. Y. S. Joe, A. M. Satanin, C. S. Kim. Classical analogy of Fano resonances. *Phys Scripta* **2006**, 74, (2), 259-266.
128. F. Hao, Y. Sonnefraud, P. Van Dorpe, S. A. Maier, N. J. Halas, P. Nordlander. Symmetry Breaking in Plasmonic Nanocavities: Subradiant LSPR Sensing and a Tunable Fano Resonance. *Nano Lett* **2008**, 8, (11), 3983-3988.
129. S. Zhang, D. A. Genov, Y. Wang, M. Liu, X. Zhang. Plasmon-induced transparency in metamaterials. *Phys Rev Lett* **2008**, 101, (4).
130. T. W. Ebbesen, C. Genet, S. I. Bozhevolnyi. Surface-plasmon circuitry. *Phys Today* **2008**, 61, (5), 44-50.
131. Z. H. Han, S. I. Bozhevolnyi. Plasmon-induced transparency with detuned ultracompact Fabry-Perot resonators in integrated plasmonic devices. *Opt Express* **2011**, 19, (4), 3251-3257.
132. B. Liedberg, C. Nylander, I. Lundstrom. Surface-Plasmon Resonance for Gas-Detection and Biosensing. *Sensor Actuator* **1983**, 4, (2), 299-304.
133. J. Homola. Surface plasmon resonance sensors for detection of chemical and biological species. *Chem Rev* **2008**, 108, (2), 462-493.
134. P. E. Sheehan, L. J. Whitman. Detection limits for nanoscale biosensors. *Nano Lett* **2005**, 5, (4), 803-807.
135. T. M. Squires, R. J. Messinger, S. R. Manalis. Making it stick: convection, reaction and diffusion in surface-based biosensors. *Nat Biotechnol* **2008**, 26, (4), 417-426.
136. Laurent Feuz, Fredrik Höök, Erik Reimhult, Design of Intelligent Surface Modifications and Optimal Liquid Handling for Nanoscale Bioanalytical Sensors. In *Intelligent Surfaces in Biotechnology*, John Wiley & Sons, Inc.: 2012; pp 71-122.
137. F. De Angelis, F. Gentile, F. Mecarini, G. Das, M. Moretti, P. Candeloro, M. L. Coluccio, G. Cojoc, A. Accardo, C. Liberale, R. P. Zaccaria, G. Perozziello, L. Tirinato, A. Toma, G. Cuda, R. Cingolani, E. Di Fabrizio. Breaking the diffusion limit with super-hydrophobic delivery of molecules to plasmonic nanofocusing SERS structures. *Nat Photonics* **2011**, 5, (11), 683-688.
138. F. Eftekhari, C. Escobedo, J. Ferreira, X. B. Duan, E. M. Girotto, A. G. Brolo, R. Gordon, D. Sinton. Nanoholes As Nanochannels: Flow-through Plasmonic Sensing. *Anal Chem* **2009**, 81, (11), 4308-4311.
139. M. P. Jonsson, A. B. Dahlin, L. Feuz, S. Petronis, F. Hook. Locally Functionalized Short-Range Ordered Nanoplasmonic Pores for Bioanalytical Sensing. *Anal Chem* **2010**, 82, (5), 2087-2094.
140. C. Escobedo, A. G. Brolo, R. Gordon, D. Sinton. Optofluidic Concentration: Plasmonic Nanostructure as Concentrator and Sensor. *Nano Lett* **2012**, 12, (3), 1592-1596.
141. Herbert A. Pohl, *Dielectrophoresis : the behavior of neutral matter in nonuniform electric fields*. (Cambridge University Press, 1978).
142. A. Barik, L. M. Otto, D. Yoo, J. Jose, T. W. Johnson, S. H. Oh. Dielectrophoresis-Enhanced Plasmonic Sensing with Gold Nanohole Arrays. *Nano Lett* **2014**, 14, (4), 2006-2012.
143. S. Cherukulappurath, S. H. Lee, A. Campos, C. L. Haynes, S. H. Oh. Rapid and Sensitive in Situ SERS Detection Using Dielectrophoresis. *Chem Mater* **2014**, 26, (7), 2445-2452.

144. A. Barik, S. Cherukulappurath, N. J. Wittenberg, T. W. Johnson, S. H. Oh. Dielectrophoresis-Assisted Raman Spectroscopy of Intravesicular Analytes on Metallic Pyramids. *Anal Chem* **2016**, 88, (3), 1704-1710.
145. Hywel Morgan, Nicolas G. Green, *AC electrokinetics : colloids and nanoparticles*. (Research Studies Press, 2003).
146. R. Krupke, F. Hennrich, H. von Lohneysen, M. M. Kappes. Separation of metallic from semiconducting single-walled carbon nanotubes. *Science* **2003**, 301, (5631), 344-347.
147. Avijit Barik, Xiaoshu Chen, Sang-Hyun Oh. Ultralow-Power Electronic Trapping of Nanoparticles with Sub-10 nm Gold Nanogap Electrodes. *Nano Lett* **2016**, 16, (10), 6317-6324
148. S. A. Maier, P. G. Kik, H. A. Atwater, S. Meltzer, E. Harel, B. E. Koel, A. A. G. Requicha. Local detection of electromagnetic energy transport below the diffraction limit in metal nanoparticle plasmon waveguides. *Nat Mater* **2003**, 2, (4), 229-232.
149. N. J. Halas, S. Lal, W. S. Chang, S. Link, P. Nordlander. Plasmons in Strongly Coupled Metallic Nanostructures. *Chem Rev* **2011**, 111, (6), 3913-3961.
150. Lukas Novotny, Bert Hecht, *Principles of nano-optics*. 2nd, (Cambridge University Press, 2012).
151. V. M. Shalaev, W. S. Cai, U. K. Chettiar, H. K. Yuan, A. K. Sarychev, V. P. Drachev, A. V. Kildishev. Negative index of refraction in optical metamaterials. *Opt Lett* **2005**, 30, (24), 3356-3358.
152. M. Amjadi, A. Pichitpajongkit, S. Lee, S. Ryu, I. Park. Highly Stretchable and Sensitive Strain Sensor Based on Silver Nanowire-Elastomer Nanocomposite. *Acs Nano* **2014**, 8, (5), 5154-5163.
153. L. Gao, Y. H. Zhang, H. Zhang, S. Doshay, X. Xie, H. Y. Luo, D. Shah, Y. Shi, S. Y. Xu, H. Fang, J. A. Fan, P. Nordlander, Y. G. Huang, J. A. Rogers. Optics and Nonlinear Buckling Mechanics in Large-Area, Highly Stretchable Arrays of Plasmonic Nano structures. *Acs Nano* **2015**, 9, (6), 5968-5975.
154. J. Lee, P. Lee, H. Lee, D. Lee, S. S. Lee, S. H. Ko. Very long Ag nanowire synthesis and its application in a highly transparent, conductive and flexible metal electrode touch panel. *Nanoscale* **2012**, 4, (20), 6408-6414.
155. H. O. Jacobs, A. R. Tao, A. Schwartz, D. H. Gracias, G. M. Whitesides. Fabrication of a cylindrical display by patterned assembly. *Science* **2002**, 296, (5566), 323-325.
156. N. F. Yu, P. Genevet, M. A. Kats, F. Aieta, J. P. Tetienne, F. Capasso, Z. Gaburro. Light Propagation with Phase Discontinuities: Generalized Laws of Reflection and Refraction. *Science* **2011**, 334, (6054), 333-337.
157. A. V. Kildishev, A. Boltasseva, V. M. Shalaev. Planar Photonics with Metasurfaces. *Science* **2013**, 339, (6125).
158. X. J. Ni, Z. J. Wong, M. Mrejen, Y. Wang, X. Zhang. An ultrathin invisibility skin cloak for visible light. *Science* **2015**, 349, (6254), 1310-1314.
159. I. M. Pryce, K. Aydin, Y. A. Kelaita, R. M. Briggs, H. A. Atwater. Highly Strained Compliant Optical Metamaterials with Large Frequency Tunability. *Nano Lett* **2010**, 10, (10), 4222-4227.
160. S. Aksu, M. Huang, A. Artar, A. A. Yanik, S. Selvarasah, M. R. Dokmeci, H. Altug. Flexible Plasmonics on Unconventional and Nonplanar Substrates. *Adv Mater* **2011**, 23, (38), 4422-4430.
161. J. Zhang, C. Con, B. Cui. Electron Beam Lithography on Irregular Surfaces Using an Evaporated Resist. *Acs Nano* **2014**, 8, (4), 3483-3489.

162. D. Chanda, K. Shigeta, S. Gupta, T. Cain, A. Carlson, A. Mihi, A. J. Baca, G. R. Bogart, P. Braun, J. A. Rogers. Large-area flexible 3D optical negative index metamaterial formed by nanotransfer printing. *Nat Nanotechnol* **2011**, 6, (7), 402-407.
163. Q. Xu, R. M. Rioux, G. M. Whitesides. Fabrication of complex metallic nanostructures by nanoskiving. *Acs Nano* **2007**, 1, (3), 215-227.
164. M. Hegner, P. Wagner, G. Semenza. Ultralarge Atomically Flat Template-Stripped Au Surfaces for Scanning Probe Microscopy. *Surf Sci* **1993**, 291, (1-2), 39-46.
165. C. H. Sun, N. C. Linn, P. Jiang. Templated fabrication of periodic metallic nanopyramid arrays. *Chem Mater* **2007**, 19, (18), 4551-4556.
166. J. C. Yang, H. W. Gao, J. Y. Suh, W. Zhou, M. H. Lee, T. W. Odom. Enhanced Optical Transmission Mediated by Localized Plasmons in Anisotropic, Three-Dimensional Nanohole Arrays. *Nano Lett* **2010**, 10, (8), 3173-3178.
167. H. Im, S. H. Lee, N. J. Wittenberg, T. W. Johnson, N. C. Lindquist, P. Nagpal, D. J. Norris, S. H. Oh. Template-Stripped Smooth Ag Nanohole Arrays with Silica Shells for Surface Plasmon Resonance Biosensing. *Acs Nano* **2011**, 5, (8), 6244-6253.
168. W. Zhou, T. W. Odom. Tunable subradiant lattice plasmons by out-of-plane dipolar interactions. *Nat Nanotechnol* **2011**, 6, (7), 423-427.
169. T. W. Johnson, Z. J. Lapin, R. Beams, N. C. Lindquist, S. G. Rodrigo, L. Novotny, S. H. Oh. Highly Reproducible Near-Field Optical Imaging with Sub-20-nm Resolution Based on Template-Stripped Gold Pyramids. *Acs Nano* **2012**, 6, (10), 9168-9174.
170. K. L. Lee, P. W. Chen, S. H. Wu, J. B. Huang, S. Y. Yang, P. K. Wei. Enhancing Surface Plasmon Detection Using Template-Stripped Gold Nanoslit Arrays on Plastic Films. *Acs Nano* **2012**, 6, (4), 2931-2939.
171. H. W. Gao, J. Henzie, T. W. Odom. Direct evidence for surface plasmon-mediated enhanced light transmission through metallic nanohole arrays. *Nano Lett* **2006**, 6, (9), 2104-2108.
172. M. Saboktakin, X. C. Ye, U. K. Chettiar, N. Engheta, C. B. Murray, C. R. Kagan. Plasmonic Enhancement of Nanophosphor Upconversion Luminescence in Au Nanohole Arrays. *Acs Nano* **2013**, 7, (8), 7186-7192.
173. A. G. Brolo, R. Gordon, B. Leathem, K. L. Kavanagh. Surface plasmon sensor based on the enhanced light transmission through arrays of nanoholes in gold films. *Langmuir* **2004**, 20, (12), 4813-4815.
174. A. Lesuffleur, H. Im, N. C. Lindquist, S. H. Oh. Periodic nanohole arrays with shape-enhanced plasmon resonance as real-time biosensors. *Appl Phys Lett* **2007**, 90, (24).
175. N. C. Lindquist, A. Lesuffleur, H. Im, S. H. Oh. Sub-micron resolution surface plasmon resonance imaging enabled by nanohole arrays with surrounding Bragg mirrors for enhanced sensitivity and isolation. *Lab Chip* **2009**, 9, (3), 382-387.
176. T. Xu, Y. K. Wu, X. G. Luo, L. J. Guo. Plasmonic nanoresonators for high-resolution colour filtering and spectral imaging. *Nat Commun* **2010**, 1.
177. S. P. Burgos, S. Yokogawa, H. A. Atwater. Color Imaging via Nearest Neighbor Hole Coupling in Plasmonic Color Filters Integrated onto a Complementary Metal-Oxide Semiconductor Image Sensor. *Acs Nano* **2013**, 7, (11), 10038-10047.
178. J. Henzie, M. H. Lee, T. W. Odom. Multiscale patterning of plasmonic metamaterials. *Nat Nanotechnol* **2007**, 2, (9), 549-554.
179. J. W. Menezes, J. Ferreira, M. J. L. Santos, L. Cescato, A. G. Brolo. Large-Area Fabrication of Periodic Arrays of Nanoholes in Metal Films and Their Application in Biosensing and Plasmonic-Enhanced Photovoltaics. *Adv Funct Mater* **2010**, 20, (22), 3918-3924.
180. S. H. Lee, K. C. Bantz, N. C. Lindquist, S. H. Oh, C. L. Haynes. Self-Assembled Plasmonic Nanohole Arrays. *Langmuir* **2009**, 25, (23), 13685-13693.

181. D. Yoo, T. W. Johnson, S. Cherukulappurath, D. J. Norris, S. H. Oh. Template-Stripped Tunable Plasmonic Devices on Stretchable and Rollable Substrates. *Acs Nano* **2015**, 9, (11), 10647-10654.
182. K. J. Lee, K. A. Tossier, R. G. Nuzzo. Fabrication of stable metallic patterns embedded in poly(dimethylsiloxane) and model applications in non-planar electronic and lab-on-a-chip device patterning. *Adv Funct Mater* **2005**, 15, (4), 557-566.
183. A. R. Zakharian, M. Mansuripur, J. V. Moloney. Transmission of light through small elliptical apertures. *Opt Express* **2004**, 12, (12), 2631-2648.
184. S. Cherukulappurath, T. W. Johnson, N. C. Lindquist, S. H. Oh. Template-Stripped Asymmetric Metallic Pyramids for Tunable Plasmonic Nanofocusing. *Nano Lett* **2013**, 13, (11), 5635-5641.
185. J. Henzie, E. S. Kwak, T. W. Odom. Mesoscale metallic pyramids with nanoscale tips. *Nano Lett* **2005**, 5, (7), 1199-1202.
186. A. Boltasseva, V. S. Volkov, R. B. Nielsen, E. Moreno, S. G. Rodrigo, S. I. Bozhevolnyi. Triangular metal wedges for subwavelength plasmon-polariton guiding at telecom wavelengths. *Opt Express* **2008**, 16, (8), 5252-5260.
187. J. Homola, I. Koudela, S. S. Yee. Surface plasmon resonance sensors based on diffraction gratings and prism couplers: sensitivity comparison. *Sensor Actuat B-Chem* **1999**, 54, (1-2), 16-24.
188. M. C. K. Wiltshire, J. B. Pendry, I. R. Young, D. J. Larkman, D. J. Gilderdale, J. V. Hajnal. Microstructured magnetic materials for RF flux guides in magnetic resonance imaging. *Science* **2001**, 291, (5505), 849-851.
189. D. Shin, Y. Urzhumov, Y. Jung, G. Kang, S. Baek, M. Choi, H. Park, K. Kim, D. R. Smith. Broadband electromagnetic cloaking with smart metamaterials. *Nat Commun* **2012**, 3.
190. H. Tan, A. Gilbertson, S. Y. Chou. Roller nanoimprint lithography. *J Vac Sci Technol B* **1998**, 16, (6), 3926-3928.
191. J. G. Ok, H. S. Youn, M. K. Kwak, K. T. Lee, Y. J. Shin, L. J. Guo, A. Greenwald, Y. S. Liu. Continuous and scalable fabrication of flexible metamaterial films via roll-to-roll nanoimprint process for broadband plasmonic infrared filters. *Appl Phys Lett* **2012**, 101, (22).
192. M. Imada, A. Fujimori, Y. Tokura. Metal-insulator transitions. *Rev Mod Phys* **1998**, 70, (4), 1039-1263.
193. D. J. Hilton, R. P. Prasankumar, S. Fourmaux, A. Cavalleri, D. Brassard, M. A. El Khakani, J. C. Kieffer, A. J. Taylor, R. D. Averitt. Enhanced photosusceptibility near T(c) for the light-induced insulator-to-metal phase transition in vanadium dioxide (vol 99, art no 226401, 2007). *Phys Rev Lett* **2008**, 100, (1).
194. T. Driscoll, H. T. Kim, B. G. Chae, M. Di Ventra, D. N. Basov. Phase-transition driven memristive system. *Appl Phys Lett* **2009**, 95, (4).
195. F. Beteille, J. Livage. Optical switching in VO₂ thin films. *J Sol-Gel Sci Techn* **1998**, 13, (1-3), 915-921.
196. Y. G. Jeong, S. Han, J. Rhie, J. S. Kyoung, J. W. Choi, N. Park, S. Hong, B. J. Kim, H. T. Kim, D. S. Kim. A Vanadium Dioxide Metamaterial Disengaged from Insulator-to-Metal Transition. *Nano Lett* **2015**, 15, (10), 6318-6323.

Appendix A

Fabrication Methods and Recipes

This appendix outlines detailed fabrication processing steps, procedures, and recipes.

A.1 Coaxial Nanogap Aperture

Wafer cleaning

1. Clean the sapphire wafer in Piranha solution ($\text{H}_2\text{SO}_4 : \text{H}_2\text{O}_2 = 1:1$) @ 120°C for more than 10 mins.
2. Soak the wafer in DI water for 5 mins.
3. Dry the wafer in the dryer (rinse for 350 sec and dry 300 sec).
4. Dry on hotplate at 150°C for 5 mins.

E-beam lithography

5. Polymethyl methacrylate resist (MicroChem, 950 PMMA C4) was spin-coated on a sapphire wafer (University Wafer).
6. Bake PMMA-coated wafer on hotplate at 180°C for 15 mins.
7. Sputter 20-nm-thick aluminum (Al) layer (AJA, ATC 2200) to avoid charging during e-beam lithography.
8. E-beam lithography (VISTEC, EBPG5000+) is then performed at 100 keV beam energy and $1000 \mu\text{C}/\text{cm}^2$ exposure dose to pattern a nanohole array.
9. After removal of Al in a CD-26 solution for 1-2 mins, the exposed resist is developed by a solution of MIBK: IPA (1:3) for 90sec, followed by IPA rinse for 60 sec.

1st metal patterning and ALD coating

10. 3 nm Ti and 200 nm Au films are then directionally deposited on the patterned substrate using electron beam evaporator (CHA, SEC 600).
11. After the lift-off process using acetone or 1165 overnight, oxygen plasma (STS, 320PC) is performed at 100W for 30s to remove resist residue.
12. Al_2O_3 is deposited on the Au nanopillar array using ALD (Cambridge Nano Tech Inc., Savannah) at a typical deposition rate of 1 \AA per cycle at 250°C .

Glancing-angle ion polishing

13. 5-nm-thick Ti and 400-nm-thick Au film are evaporated using an electron beam evaporator (CHA, SEC 600) with a planetary fixture.
14. Finally, an anisotropic ion milling (Intlvac, Nanoquest) is carried out by Ar beam of 130 mA and 36 V with tilt of 10° from the horizontal plane for 90 mins.

A.2 Trench Nanogap Resonator-Electrode

Wafer cleaning

1. Clean the glass wafer in Piranha solution ($\text{H}_2\text{SO}_4 : \text{H}_2\text{O}_2 = 1:1$) at 120°C for more than 10 mins.
2. Soak the wafer in DI water for 5 mins.
3. Dry the wafer in the dryer (rinse for 350 sec and dry 300 sec).
4. Dry on hotplate @ 150°C for 5 mins.

1st Layer Photolithography

5. Do HMDS treatment for 3 min in the HMDS chamber to promote the adhesion between photoresist and glass substrate.
6. Spincoat NR71-1500P (negative photoresist) with 3000 rpm for 40 sec and softbake it on hotplate at 150°C for 2 mins. Bake time depends on types of substrates such as Si and glass.
7. Do photolithography with exposure time 25 s, and hard contact using MA-6.
8. Post-Exposure Bake (PEB) at 100°C for 1.5 mins.
9. Do developing using RD 6 for 25 s and then rinse 2 mins. (Long rinse time can cause PR to be detached on the substrate and come up.)
10. Dry with N₂ gun. Be careful to dry.
11. Remove remained PR using O2CLEAN for 30 s using STS etcher.

Making nanogap patterns

12. Deposit 5 nm Cr and 150 nm Au using Temescal.

13. Do liftoff using 1165 overnight and then add sonication for 3 mins if metals are still attached to PR.
14. Rinse with acetone and sonication and then rinse with DI water. Dry with N₂ gun.
15. Deposit 10 nm-thick Al₂O₃ at 250°C. Put a piece of Si wafer to monitor the deposited Al₂O₃ thickness. High temperature ALD will give the strong adhesion between 1st Au and the deposited Al₂O₃.
16. Deposit 140 nm Au using Temescal without Cr adhesion layer. When loading a wafer place the flat zone of wafer to the center of hemisphere holder. In this case, the quality of left-sided nanogap will be better than right-sided one.
17. Peel off the 2nd Au thin film using 3M scotch tape. After removing 2nd metal layer, nanogap patterns will be created on the glass wafer.

2nd Layer Photolithography + Ion milling

18. Do HMDS treatment for 3 mins.
19. Spincoat NR71-3000P with 5000 rpm for 40 s and softbake it at 150°C for 2 mins.
20. Do photolithography with exposure time 30 s, and hard contact using MA-6.
21. Post-Exposure Bake (PEB) at 100°C for 1.5 mins.
22. Do developing using RD 6 for 50 s and then rinse 1.5 mins. (Long rinse time can cause PR to be detached on the substrate and come up.)
23. Dry with N₂ gun. Be careful to dry.
24. After developing, you can see the remained PR on the metal surface. Do not add more developing or rinse. Remove remained PR using O2CLEAN for 1-2 mins using STS etcher.
25. Do ion milling with fast recipe (75° angle). Milling time depends on the thickness of Al₂O₃ to be etched. 11 mins is enough to etch 10 nm-thick Al₂O₃ + 150 nm-thick Au. Do ion milling without holder metal ring to etch out entire metal deposited on glass wafer.
26. Remove PR using RR41 overnight and then do sonication for 2 min with 50% power.
27. Do O2CLEAN for 1 min using STS etcher.

3rd Layer Photolithography

28. Do HMDS treatment for 3 mins.
29. Spincoat NR71-3000P with 5000 rpm for 40 s and softbake it at 150°C for 2 mins.
30. Do photolithography with exposure time 25 s, and hard contact using MA-6.

31. Post-Exposure Bake (PEB) at 100°C for 1.5 mins.
32. Do developing using RD 6 for 50 s and then rinse 1.5 mins. (Long rinse time can cause PR to be detached on the substrate and come up.)
33. Dry with N₂ gun. Be careful when you are drying a sample with N₂ gun. If wind is strong, very narrow PR patterns can be collapsed.
34. Do O2CLEAN for 1 min using STS etcher.

3rd metal deposition + Glancing-angle-ion polishing + Dicing

35. Deposit 5 nm Cr and 1 um Ag using Temescal. When loading wafer, place the flat zone of wafer to the center of hemisphere holder. In this case, the quality of left-sided nanogap will be better than right-sided one.
36. Do ion-milling with fast recipe (10°) for 20 mins, which will facilitate the following lift-off process by removing the metal deposited on the sidewall of PR.
37. Spincoat S1818 with 1500 rpm for 30 seconds and cure on hotplate at 50°C for 5 mins.
38. Do dicing using sawing machine.
39. Do lift-off process with RR41 overnight.
40. Do sonication with mild power.

A.3 Template-stripped Nanohole Array Fabrication

Wafer cleaning

1. Clean the Si wafer in Piranha solution (H₂SO₄ : H₂O₂ = 1:1) at 120°C for more than 10 mins.
2. Soak the wafer in DI water for 4 mins while changing the water at least once.
3. Dry the wafer in the dryer (bay 3) – rinse for 350 s and dry 300 s.
4. Dry on hotplate at 150°C for 5 mins.

SiO₂ mask layer deposition

5. We usually use LPCVD-SiO₂-grown Si wafer. We can grow SiO₂ thin film on bare Si wafer using APCVD in Keller clean room. But this furnace-type CVD is very expensive for use and gives us non-uniform film thickness. Therefore, if you have a plan to make nanohole samples frequently, I recommend purchasing SiO₂-grown Si wafer from

University wafer. If not, PECVD-SiO₂-deposited Si wafer is also available for a hard mask.

6. Deposit SiO₂ thin film using PECVD in Keller clean room with recipe SIO2100 (which means SiO₂ 100°C process). Deposition time can be determined by thickness needed. We usually use two thicknesses like 100 nm or 200 nm SiO₂ as a hard mask.

Nanoimprint lithography

7. Clean the syringe using acetone and IPA first. Then add a filter (200 nm size) at the tip of syringe. Then, pour 1 ml of NXR 1025 (thermal resist) into the syringe.
8. Cleave a whole Si wafer by 3 x 3 and remove particles which may occur on Si surface with N₂ gun. If some particles get trapped on the top surface, it might create bad patterning problem.
9. Spin-coat thermal resist on Si wafer to attain a thickness ~300 nm by 3500 rpm for 30 sec. Then, bake the wafer on hot plate at 200 °C for 120 sec.
10. We have various types of nanoimprint stamp which can be purchased at Lightsmyth (www.lightsmyth.com). We have to coat the anti-adhesion SAM layer at once before you use a new stamp. First, place the Si nanoimprint stamp inside the vacuum chamber and drop a little amount of anti-adhesion coating solution on glass dish, which will be put together inside the vacuum chamber. Then keep pumping down for 3 hours. When you pick up the Si stamp and handle it, please be careful to prevent the Si stamp from be damaged from tweezer. It is recommended to use a plastic tweezer rather than metallic one.
11. Do nanoimprint with a Si stamp on the thermal resist-coated Si wafer. Pressure 300 psi, temperature 130 °C, time 2 mins.
12. After nanoimprinting, detach the stamp from Si wafer using a razor blade.

Dry etching processes

13. Do O2NIL50W (O₂ Cleaning recipe) in STS etcher (load the recipe and at the etch step be careful to abort after the required time) for 30 s. This step is required to remove any residual resist on the imprinted area.
14. Do PJSOXIDE (SiO₂ etching recipe). Etching time depends on the SiO₂ mask thickness. To make smaller size nanohole less than 140 nm, thicker (200 nm) SiO₂ is needed while thinner (100 nm) one is enough for larger nanohole with 180 nm in diameter.

For 100 nm-thick SiO₂, etching time is around 4 min 30 sec.

For 200 nm-thick SiO₂, etching time is around 8 min 30 sec. Those are the case for LPCVD-grown SiO₂ hard mask. LPCVD-grown SiO₂ thin film is much dense compared to PECVD, resulting in slow etching rate. Thus, you have to do etching rate test whenever you change a type of thin film or thickness.

15. Do O₂ CLEAN (O₂ Cleaning recipe) for 3 mins to remove thermal resist. However, this step can be skipped.
16. Remove the thermal resist using A.M.I cleaning. Then, clean the sample with piranha until the thermal resist disappears totally.
17. Do Si etching with CNF-14-V at the deep trench etcher. When you decide the etching time, you have to consider two factors like the depth of Si nanohole and etching rate of SiO₂ for CNF-14-V recipe. SiO₂ hard mask can be etched by CNF-14-V recipe even though it is Si etching recipe. So we have to stop Si etching process before SiO₂ hard mask is gone, while we need 500 nm depth of Si nanohole for template-stripping. Si etching time of 3-5 min would be good.
18. Remove the remained SiO₂ hard mask using BOE etchant.

Metal deposition process

19. To do template-stripping, we have to grow fresh native oxide on the surface of Si nanohole chip, which will result in poor adhesion between Si nanohole chip and Au or Ag metal layer. Do BOE to remove old native oxide on the Si surface, followed by piranha cleaning (15-30 min) to grow fresh native oxide on the Si surface. Rinse with DI water fully and dry with N₂ gun.
20. Deposit Au or Ag metal as thick as 100 nm (for larger sized-nanohole) or 200 nm (for smaller sized-nanohole) using Temescal with deposition rate of 1Å/sec.

Template-stripping method

21. Before do template-stripping, prepare for a supporting substrate to peel off the metal using optical epoxy. Usually a glass slide is useful for template-stripping. So, do cleaning glass slide with piranha solution.
22. Drop two droplets of 5µl onto the glass slide at which metal-deposited Si mode will be placed.
23. Put the metal-deposited Si mode upside down on the glass substrate.

24. Optical epoxy will start to spread out along with a gap between a glass slide and a Si mold.
To get uniform spreading of epoxy, you may tilt the sample overnight, thereby making epoxy is going down due to gravity.
25. Cure the sample using UV lamp for 4 hours, then do thermal curing on hotplate at 60-70°C overnight.
26. Insert a razor blade into the gap between a glass slide and a Si mold, which will generate a crack propagating inside the gap. You can get rid of Si mode from a glass slide by leaving metallic nanostructure onto the glass slide.

Appendix B

Common Acronyms

Table B.1 A listing of the common acronyms used throughout the dissertation text.

Acronym	Definition
AFM	Atomic Force Microscopy
ALD	Atomic Layer Deposition
BOE	Buffered Oxide Etchant
DEP	Dielectrophoresis
EOT	Extraordinary Optical Transmission
ENZ	Epsilon Near Zero
FDTD	Finite Difference Time Domain
FEM	Finite Element Method
FSS	Frequency Selective Surface
FP	Fabry-Pérot
IR	Infrared
MIM	Metal Insulator Metal
PDMS	Polydimethylsiloxane
PIT	Plasmon induced Transparency
PMMA	Polymethyl Methacrylate
RIE	Reactive Ion Etching
SAM	Self Assembled Monolayer
SEIRA	Surface Enhanced Infrared Absorption
SERS	Surface Enhanced Raman Scattering
SPP	Surface Plasmon Polariton
SPR	Surface Plasmon Resonance